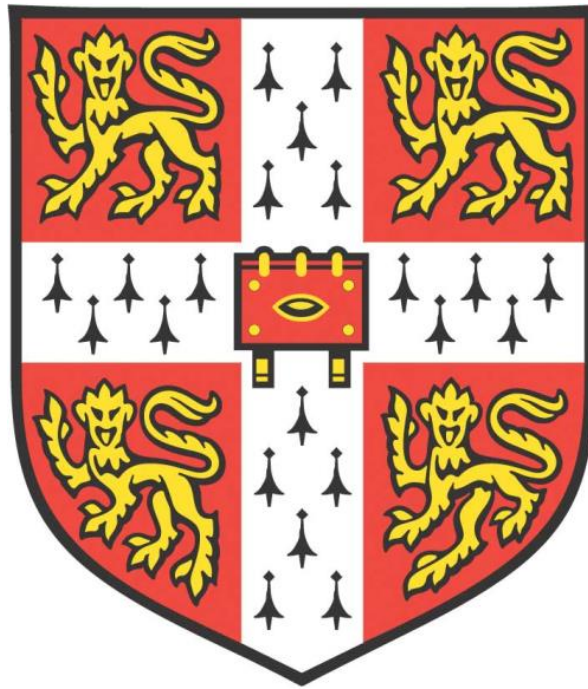


Extraction of Mechanical Properties over a Range of Strain Rates from Indentation Data



Max Edward Burley

Downing College

Department of Materials Science and Metallurgy

University of Cambridge

This dissertation is submitted for the degree of Doctor of Philosophy

September 2019

Preface

This dissertation is submitted for the degree of Doctor of Philosophy at the University of Cambridge. All of the contents are a result of my own work and includes nothing which is the outcome of work done in collaboration except as specified in the text. The research was carried out between October 2015 and September 2019, under the supervision of Professor T.W. Clyne, in the Department of Materials Science and Metallurgy.

I hereby declare that this dissertation is not substantially the same as any that I have submitted, or is being concurrently submitted for a degree or diploma or other qualification at the University of Cambridge or any other University or similar institution. I further state that no substantial part of my dissertation has already been submitted, or, is being concurrently submitted for any such degree, diploma or other qualification at the University of Cambridge or any other University or similar institution. It is fewer than 60,000 words in length.

Max E. Burley

Publications

Publications from the work in this thesis:

Burley, M., et al., *Johnson-Cook Parameter Extraction from Ballistic Impact Data via Iterative FEM Modelling*. International Journal of Impact Engineering, 2017. **112**: p. 180-192.

Burley, M., et al., *A Methodology for Obtaining Primary and Secondary Creep Characteristics from Indentation Experiments, Using a Recess*. International Journal of Mechanical Sciences, 2020. **176**.

Burley, M., et al., *Evaluation of the Fracture Energy of Magnesium via Ballistic Impact Experiments*. Materialia, 2020. **10**.

Other related publications:

Campbell, J.E., et al., *Experimental and Computational Issues for Automated Extraction of Plasticity Parameters from Spherical Indentation*. Mechanics of Materials, 2020. **124**: p.118-131.

Campbell, J.E., et al., *Comparisons Between Stress-Strain Plots Obtained from Indentation Plastometry, Based on Residual Indent Profiles*. Acta Materialia, 2020. **168**: p.87-99.

Abstract

A procedure is described for indentation creep plastometry. It is based on iterative numerical simulation of the indentation process, with repeated comparison between an experimental outcome and the corresponding model prediction, systematically varying the values of parameters in a constitutive law until optimal agreement is achieved. The experimental outcome is the penetration depth as a function of time, under a constant applied load. An important feature of the procedure is the prior creation of a spherical recess in the sample, having a pre-selected depth and a curvature radius equal to that of the indenter. This allows control over the stress levels created during the indentation creep testing and can be used to ensure that no (time-independent) plastic deformation is stimulated during the test. Confirmation of the viability of the procedure is provided via comparisons between the creep characteristics of pure nickel samples at 750°C, obtained in this way and via conventional uniaxial tensile testing.

A similar procedure has been applied for the study of rate-dependent plasticity in bulk metallic materials. Ballistic impact (indentation) of hard spherical projectiles was used to study a rigidly held target, with operative strain rates of the order 10^5 s^{-1} . Input for the FEM model includes data characterizing the (temperature-dependent) quasi-static plasticity, obtained by conventional uniaxial testing. The experimental outcomes are displacement-time plots for the projectile and the residual indent profile. Since the strain rate sensitivity is characterised by a single parameter value (C in the Johnson-Cook formulation), convergence on its optimum value is straightforward, although a parameter characterizing interfacial friction is also required. Using experimental data from (both work-hardened and annealed) copper samples, this procedure has been carried out and best-fit values of C (~ 0.016 and ~ 0.030) have been obtained.

This procedure has been extended for the study of fracture characteristics (under high imposed strain rates). The strain rate sensitivity of magnesium was evaluated ($C \sim 0.026$) as above. The main emphasis, however, is on study of its fracture characteristics, with tomographic imaging being used to obtain crack patterns for different projectile velocities. An approach based on fracture mechanics, and on use of FEM modelling to estimate the strain energy release rate required for crack propagation (i.e. the fracture energy of the material) is proposed and applied to these experimental results, leading to a value of the order of 2 kJ m^{-2} . While such a procedure is unlikely to produce accurate values, partly because the crack propagation takes place under local conditions that change rapidly and are not well-defined, this figure is plausible for the case concerned. While there are several sources of complexity, it may be possible to develop this methodology, both as a technique for fracture toughness measurement (requiring only small samples of simple shape) and as an improved approach to prediction of ballistic impact outcomes.

Acknowledgements

Without many people, this endeavour would not have been possible; however, it is probably most fitting that I begin this by acknowledging Prof. Bill Clyne and Dr. James Dean, my academic supervisors. I would like to thank Bill for his committed supervision, invaluable expertise and creating a welcoming and social working environment. I thank Dr. James Dean for his input, which was crucial to getting off to a good start (and, of course, the odd side-hustle). Many thanks also go to the Atomic Weapons Establishment for the provision of a CASE student award. I would like to thank Dr. Giles Aldrich-Smith and Nigel Park, my industrial supervisors, for their support and continued input.

Involvement with the University Football Club (CUAFC) has proved an integral part of my time at Cambridge. The opportunities and experiences that this has given me, along with the friends I have made, will stay with me forever. I thank Nikos Yerolemou and Martin Sedlak, whose friendship kick-started what has been an incredible journey – here is to the three amigos. Really, all the lads deserve their bit, but that would be a little tedious, so special mentions go to Jack Congdon, Henry Warne and Richard Wolstenhulme. It really is the best club in the world.

I would like to thank all the members of the Gordon Lab. I feel extremely lucky to have had such a good group, both socially and academically. Lab tours, punting trips, pub trips, dubiously long coffee breaks, you name it, we have it. I would like to thank Dr. Jimmy Campbell and Dr. Sam Troughton (BDT) for surprising me in Cindies every Wednesday in the earlier years of my PhD and Matt O’Hara and Julia Pürstl for taking on the responsibility of looking after me in BDT’s absence and Jimmy’s old age. As the saying goes, with old age comes wisdom, and it is worth noting, that the input of Jimmy over the last two years is very appreciated. Special thanks to my contemporaries Megan McGregor and Alastair Houston, my beer and hair care advisor Rob Thompson, Amy Goodfellow for emotional support, Noel Glazenger, Eleanor Brug, Tom Edwards, Yi Cui and Eleonore Poli for being part of the journey.

Thank you to my parents, whom I know have been watching on anxiously as my finish date moved further and further back. Your continued support is extremely appreciated.

Thank you to my landlord, Joe Taylor, who was kind enough to proof-read this document. Here's to another year. Finally, a special mention to Sioned Davies, whose continual chatter has been the perfect distraction from the stresses of work this past year (when this was required).

Nomenclature

Roman Symbols

A	-	Johnson-Cook Parameter
A_1	MPa	Zerilli-Armstrong Parameter
$A_2 - A_3$	-	Zerilli-Armstrong Parameters
A_a	MPa	Athermal Zerilli-Armstrong Parameter
A_c	m^2	Area of contact
A_p	m^2	Projected Area of Contact
B	-	Johnson Cook Parameter
C	-	Johnson-Cook Strain Rate Sensitivity Parameter
C_1	$MPa^{-n_2} s^{-(m_2+1)}$	Miller-Norton Multiplier
C_2	$MPa^{-n_2} s^{-(m_2+1)}$	Constant Temperature Miller-Norton Multiplier
C_3	MPa^{-n_2}	Steady-State Miller-Norton Multiplier
C_4	MPa^{-n_2}	Steady State Miller-Norton Multiplier (Constant T)
c	m	Crack half length
$D_1 - D_4$	-	Johnson-Cook Damage Parameter
E	GPa	Young's Modulus
E'	GPa	Non-linear Elastic Modulus
E_k	J	Kinetic Energy
F	N	Force
G	$J m^{-1}$	Strain Energy Release Rate
G_c	$J m^{-1}$	Critical Strain Energy Release Rate
G_I	$J m^{-1}$	Mode I Strain Energy Release Rate
G_{Ic}	$J m^{-1}$	Mode I Critical Strain Energy Release Rate
g	MPa	Shear Modulus
H	$kgf mm^{-2}$	Hardness
J	$J m^{-1}$	J Integral
K	MPa	Work-Hardening Coefficient
K_f	$MPa^{1/2}$	Fracture Toughness

K_c	$\text{MPa}^{1/2}$	Critical Fracture Toughness
K_I	$\text{MPa}^{1/2}$	Mode I Fracture Toughness
K_{IA}	$\text{MPa}^{1/2}$	Mode I Fracture Toughness for Arrest
K_{Ic}	$\text{MPa}^{1/2}$	Mode I Critical Fracture Toughness
K_{ID}	$\text{MPa}^{1/2}$	Mode I Dynamic Fracture Toughness
k_h	$\text{MPa m}^{1/2}$	Zerilli-Armstrong Microstructural Intensity Factor
L	m	Specimen Length
M	-	Total Number of Volume Elements
m	-	Johnson-Cook Temperature Exponent
m_2	-	Miller-Norton Time Exponent
N	-	Number of Data Points
n	-	Work Hardening Exponent
n_2	-	Creep Stress Exponent
P	N	Indentation Load
Q	kJ mol^{-1}	Activation Energy
R	m	Indenter Radius
R_{gas}	$\text{J mol}^{-1} \text{K}^{-1}$	Universal Gas Constant – 8.314
r	m	Crack Tip Radius
S_e	-	MTS Parameter
S_i	-	MTS Parameter
S_{red}	-	Reduced Sum of Squares
T	K	Temperature
T_M	K	Melting Temperature
t	seconds	Time
U	J	Internal Energy
V	m^3	Volume
V_i	m s^{-1}	Incident Velocity
W	J	Work
Z	-	Total Number of Strain Increments

Greek Symbols

γ	J m^{-2}	Surface Energy
δ	μm	Displacement

δ_{CTOD}	μm	Crack Tip Opening Displacement
ε	-	Strain
ε_c	-	Characteristic Strain (Voce)
ε_f	-	Fracture Failure Strain
$\dot{\varepsilon}$	s^{-1}	Strain Rate
λ	m	Average Grain Diameter (Zerilli-Armstrong)
μ	-	Friction Coefficient
ρ	kg m^{-3}	Density
σ	MPa	Stress
$\sigma_1 - \sigma_3$	MPa	Principal Stresses
σ_a	MPa	MTS Athermal Stress Component
σ_e	MPa	MTS Microstructural Evolution Stress Component
σ_f	MPa	Far-field stress in the Presence of a Crack
σ_{flow}	MPa	Flow Stress
σ_g	MPa	Zerilli-Armstrong Stress Component
σ_H	MPa	Hydrostatic Stress
σ_i	MPa	MTS Intrinsic Stress Component
σ_n	MPa	Normal Stress Component
σ_S	MPa	Voce Saturation Stress
σ_{VM}	MPa	Von Mises Stress
σ_Y	MPa	Yield Stress
σ^*	MPa	Critical Stress
τ	MPa	Shear Stress
Ψ	m^2	Cross-Sectional Area
ω	m	Plate Thickness

Subscripts

0	Reference
av	Average
b	Bar
cr	Creep
E	Experiment
eff	Effective

inc	Incident
M	Model
max	Maximum
N	Nominal
O	Original
P	Plastic
r	Representative
ref	Reflection
s	Specimen
T	True
trans	Transmitted

Preface	i
Publications.....	ii
Abstract	iii
Acknowledgements.....	v
Nomenclature	vii
Roman Symbols	vii
Greek Symbols	viii
Subscripts.....	ix
Chapter 1 Introduction.....	1
1.1 Applications	1
1.2 Research aims	2
1.3 Document overview.....	2
Chapter 2 Plastic Deformation and Creep of Metals	4
2.1 An Introduction to Plasticity	4
2.1.1 Deviatoric (von Mises) stress	7
2.2 An Introduction to Creep.....	8
2.2.1 Mechanisms.....	9
2.2.2 The Effect of Microstructure	11
2.2.3 Conventional Creep Testing.....	12
2.2.4 Constitutive Laws for Creep	12
Chapter 3 The Effect of High Imposed Strain Rate on Plasticity and Fracture	16
3.1 Dynamic Plasticity	16
3.1.1 Plasticity Mechanisms	18
3.2 Strain Rate Sensitive Plasticity Characterisation	21
3.2.1 Constitutive laws.....	21
3.2.2 Conventional Testing Methods.....	27

3.2.3	Characterisation by Inverse Finite Element Method	29
3.3	Dynamic Fracture	32
3.3.1	Embrittlement Mechanisms.....	38
3.3.2	Conventional Characterisation Methods.....	38
3.3.3	Dynamic Fracture in FEM	39
Chapter 4	Indentation Testing.....	43
4.1	Indentation Material Characterisation.....	43
4.1.1	Hardness.....	44
4.1.2	Plasticity	45
4.1.3	Indentation Creep.....	46
4.1.4	Ballistic (Dynamic) Indentation Methods	49
4.1.5	Indentation Methods for the study of Fracture.....	51
4.1.6	Indentation of Coatings.....	52
4.2	Factors Influencing Indentation Outcomes	53
Chapter 5	Experimental Techniques.....	55
5.1	Experimental Procedures	55
5.1.1	Specimen Production.....	55
5.1.2	Sample Preparation.....	55
5.1.3	Indentation Creep.....	57
5.1.4	Uniaxial Tensile Testing	58
5.1.5	Uniaxial Tensile Creep Testing	58
5.1.6	Uniaxial Compression Testing	59
5.1.7	Ballistic Impact (Gas Gun).....	60
5.1.8	High speed photography	61
5.1.9	Residual indent topography	61
5.1.10	X-ray Computed Tomography	62

Chapter 6	Computational Methods	63
6.1	Computational Issues	63
6.1.1	FEM Formulation for the (Recess) Indentation Creep	63
6.1.2	FEM Formulation for Ballistic Indentation (No Fracture).....	64
6.1.3	FEM Modelling of Crack Propagation.....	65
6.1.4	Constitutive Laws.....	67
6.1.5	Effect of Interfacial Friction	70
6.1.6	Model Input Data.....	70
6.1.7	Model Output Data.....	76
6.2	Convergence Procedure	77
6.2.1	Convergence Algorithm and Procedure for Creep Indentation	77
Chapter 7	A Methodology for obtaining Primary and Secondary Creep Characteristics from Indentation Experiments, using a Recess.....	79
7.1	Introduction.....	79
7.2	Microstructure	81
7.3	Quasi-static Plasticity.....	82
7.4	Uniaxial Tensile Creep Results.....	84
7.5	Indentation Creep Results.....	86
7.6	Tensile Creep Curves from Indentation Outcomes	87
7.7	Summary	91
Chapter 8	Johnson-Cook Parameter Evaluation from Ballistic Impact Data via Iterative FEM Modelling.....	93
8.1	Microstructure	93
8.2	Quasi-static plasticity.....	93
8.2.1	Stress-strain plots for ambient temperature	93
8.2.2	Stress-strain plots for elevated temperatures.....	97
8.3	Evaluation of the strain rate sensitivity parameter, C	99

8.3.1	Conditions during projectile penetration.....	99
8.3.2	Evaluation of C for the as-received material	105
8.3.3	Evaluation of C for the annealed material.....	108
8.3.4	Reliability of the inferred values of C.....	111
8.4	Summary	112
Chapter 9 Evaluation of the Fracture Energy of Magnesium via Ballistic Impact Experiments 113		
9.1	Introduction.....	113
9.2	Microstructure	113
9.3	Effects of Temperature and Strain Rate on Plasticity.....	115
9.3.1	Quasi-static Stress-strain Plots as a Function of Temperature	115
9.3.2	Effect of Strain Rate and Evaluation of C.....	116
9.4	Evaluation of the Fracture Energy	118
9.4.1	Tomographic Capture of Crack Patterns	118
9.4.2	Stress, Strain, Strain Rate and Temperature Fields.....	120
9.4.3	Simulation of Crack Growth.....	121
9.5	Summary	125
Chapter 10 Conclusions		
10.1	Creep Properties using Recess Instrumented Indentation.....	126
10.2	Extraction of a Strain Rate Sensitivity Parameter from Ballistic Indentation 127	
10.3	Measurement of Fracture Energy from Indentation Data.....	129
10.4	Future Work.....	130
References		132

Chapter 1

Introduction

1.1 Applications

The accessibility and capability of computational modelling has come on a long way in recent years. User-friendly finite element method (FEM) software packages that can simulate multi-physics problems have changed the way that research and development is conducted. The capabilities of these packages are such that the problem can be very complex. There are obvious benefits to the user of having a good understanding of the problem and the relevant physics, but the “black box” nature of these packages can lead to certain aspects being overlooked, ignored or included unnecessarily.

Key to FEM simulation is the specification of constitutive laws and their parameter characterisation. When done well, this will accurately capture the relevant material behaviour. If all other aspects of the model are considered and described thoughtfully, the simulation should accurately predict the experiment. The resulting cost saving for research and development is huge. The production and testing of hundreds of samples, potentially to destruction, can be replaced by the outcome of simulations. A more refined sample space can then be interrogated with physical experimentation to verify the simulation results and converge on an optimum component design.

The analysis of data from conventional methods can often be unsatisfactory, with material property parameters being inferred from analytical equations. These often grossly simplify the behaviour and lead to unacceptable errors; this can be demonstrated with FEM analysis. More accurate parameters can be obtained from inverse FEM methods, iterating towards a correct outcome, which is found by optimising the agreement between the experimental outcome and the simulation outcome. In theory, this procedure can be carried out with any experiment, so long as the relevant material

response is probed. Experiments with simple boundary conditions and those which activate minimal material response mechanisms are favoured. The former makes for more straightforward model construction and the latter can simplify optimisation procedures and can remove the requirement for prior knowledge of certain material property parameters.

The use of indentation for material property characterisation is an area of active research. When compared with conventional techniques, there are many attractions of this method; easy sample preparation, small volume requirements, material mapping and in situ testing. With respect to inverse FEM procedures, the boundary conditions of an indentation experiment are also relatively simple. Until recently, hardness and elastic moduli extraction were the only notable quantitative parameters obtained through indentation [1, 2]. Developments in the application of an inverse FEM procedure for the extraction of quasi-static plasticity parameters from indentation data have also been successfully demonstrated [3].

1.2 Research aims

Following the success of methods for extracting quasi-static plasticity parameters from indentation data, this study is aimed at extending these to characterise the creep and high strain rate plasticity response of metallic materials from instrumented “recess” indentation and (ballistic) dynamic indentation experiments, respectively. Further to this, an attempt has been made at developing a procedure for extracting information on fracture characteristics, following ballistic impact.

1.3 Document overview

Chapter 2 introduces the deformation mechanisms of plasticity and creep for metallic materials. Conventional methods for characterisation are discussed.

Chapter 3 introduces the phenomenon of strain rate sensitive plasticity and the dynamic fracture response of metallic materials.

Chapter 4 reviews indentation characterisation methods, discussing the benefits of analytical and numerical procedures.

Chapter 5 presents the experimental procedures used in this work. This includes the creep recess indentation and ballistic indentation methods

Chapter 6 presents the computations procedures used in this work. The finite element model construction and convergence procedures are discussed.

Chapter 7 demonstrates a novel method for the characterisation of primary and secondary creep from indentation data.

Chapter 8 Presents a novel method for the characterisation of strain rate sensitive plasticity parameters from ballistic (dynamic) indentation.

Chapter 9 demonstrates a method for the study of dynamic fracture events in material subject to ballistic indentation.

The conclusions from this work and possible further advances are discussed in **Chapter 10**.

Chapter 2

Plastic Deformation and Creep of Metals

2.1 An Introduction to Plasticity

Beyond an elastic limit, metals commonly deform plastically. This is fundamental to their prominence in engineering applications, because it allows for considerable strength and toughness, in addition to being workable. At quasi-static rates, the key mechanism for this behaviour is dislocation glide [4]. At higher strain rates, twinning and/or shear phase transformations may become the dominant mechanism [5]. They all involve an internal rearrangement of the structure, on various length scales, to give a permanent change in shape.

The most prominent method for measuring plasticity is the uniaxial tensile (or compression) test [6]. A uniaxial load is applied to a specimen of uniform cross-section. This load is ramped up (usually in displacement control) to probe the yielding and subsequent work hardening behaviour. A typical quasi-static tensile stress-strain curve is shown in Figure 2.1 [7, 8]. The uniform nature of the stress and strain field for an idealised uniaxial test allow stresses and strains to be evaluated using simple analytical expressions. Nominal values of the stress and strain are given by

$$\varepsilon_N = \frac{L - L_0}{L_0} \quad \text{and} \quad \sigma_N = \frac{F}{\Psi_0} \quad (2.1)$$

where L_0 is the original length of the specimen, L_1 the final length, F the applied load and Ψ_0 the original cross-sectional area. The fact that length and area are changing means that these nominal values begin to deviate from the actual (“true”) values, given by

$$\varepsilon_T = \ln\left(\frac{L}{L_0}\right) \quad \text{and} \quad \sigma_T = \frac{F}{\Psi} \quad (2.2)$$

where Ψ , the cross-sectional area, is allowed to change during the test. With the assumption that volume is conserved (i.e. neglecting elastic strains), true stress-strain values can be found from nominal values, using the standard expressions [9]:

$$\varepsilon_T = \ln(1 + \varepsilon_N) \quad \text{and} \quad \sigma_T = \sigma_N(1 + \varepsilon_N) \quad (2.3)$$

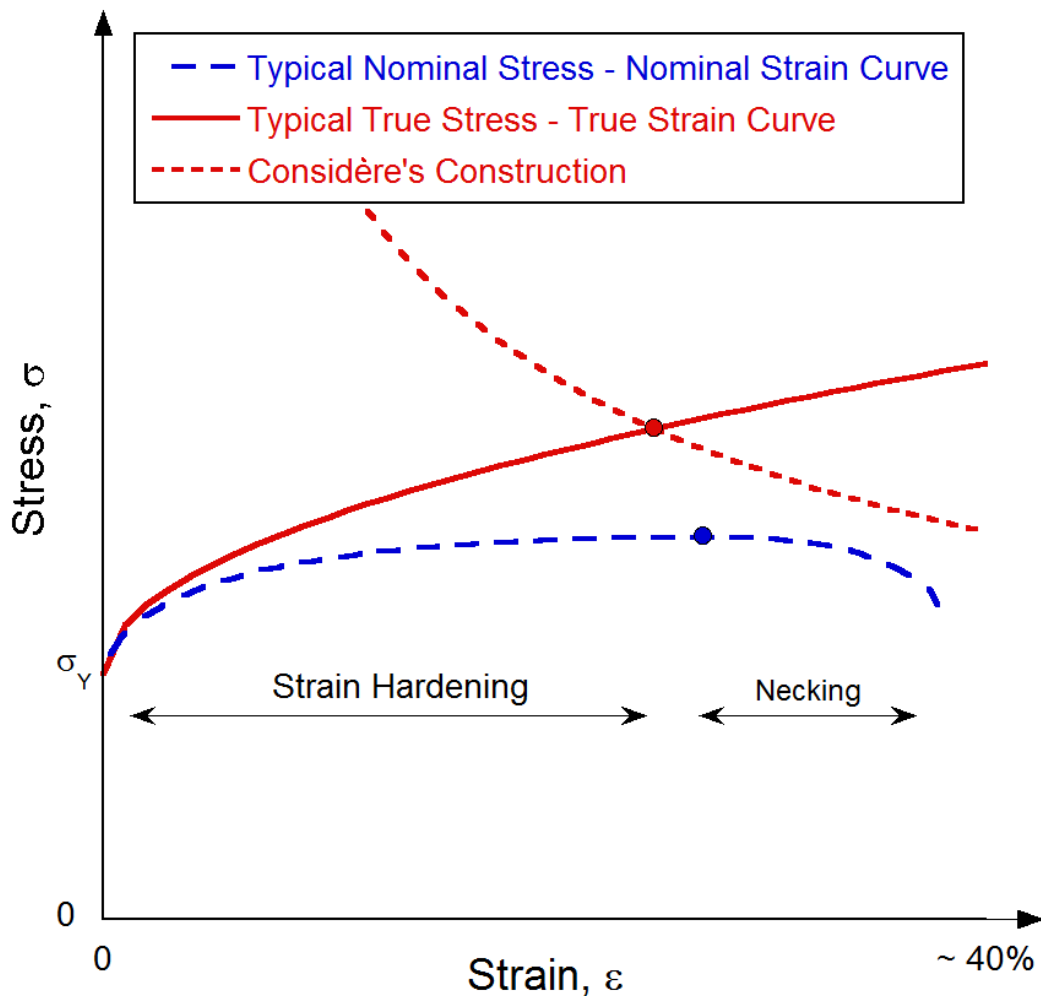


Figure 2.1 A typical tensile nominal stress-strain curve is shown, with the corresponding true stress-strain curve. A strain hardening region is seen, followed by necking, as predicted by Considère's construction. Elastic deformations have been omitted.

On progression of a uniaxial test to high strains (~20%), it is common for the approximation that the stress and strain fields are uniform to break down. Instability

phenomena (necking in tension and barrelling in compression) tend to lead to non-uniform cross-sectional areas, which in turn limits the usefulness of Equation 2.3 [8].

Necking is a geometrical phenomenon that may be observed when a sample is uniaxially loaded in tension. The susceptibility of a material to necking is closely linked to the work hardening rate. When a neck begins to form, the stresses locally rise relative to the rest of the specimen. For a material with negligible work hardening, this will in turn lead to further straining within the necked region and a further drop in the cross sectional area. This feedback loop will lead to failure of the specimen. For a material with a high work hardening rate, the flow stress within the necked region may increase sufficiently such that further deformation will occur in the regions of lower stress outside the neck. In this way, work hardening acts to suppress necking.

By assuming that the onset of necking occurs when an increase in the local strain produces no net increase in the load, Considère demonstrated that a neck would form when the rate of work hardening was equal to the true stress at that point, given by [9]

$$\sigma_T = \frac{d\sigma_T}{d\varepsilon_T} \quad (2.4)$$

Beyond the onset of necking, it is difficult to predict the behaviour. This construction has been shown on Figure 2.1, predicting the onset of necking in terms of the true strain. Equation 2.3 can then be used to calculate the nominal strain at which this occurs. The strain to failure becomes a function of specimen geometry and work hardening characteristics. Although possible in very ductile materials, it is very uncommon for the material to neck to a point and then fail. Engineering metals tend to experience some necking before fracture occurs within the necked region.

Barrelling is observed in compression samples, where friction at the compression interfaces constrains lateral movement of the sample. This leads to a bulging of the specimen between the compression surfaces and therefore to non-uniform stress and strain fields. It is more difficult to quantify this effect analytically and, although it does not lead to the failure of the sample, the expressions given in Equation 2.3 become less satisfactory.

Although it is possible to describe the true stress-true strain relationship as a set of data pairs, it can be beneficial to capture the behaviour with an appropriate constitutive relation [10]. A constitutive law is an (empirical) expression describing the material behaviour. For instance, the “flow stress” may be predicted as a function of strain, strain rate and temperature. For rate-independent plasticity, the Ludwik-Holloman and Voce laws are commonly used. The Ludwik-Holloman power law, [11], is expressed as

$$\sigma_{\text{flow}} = \sigma_Y + K\varepsilon_p^n \quad (2.5)$$

where σ_{flow} is the applied stress, σ_Y is the yield stress, K is the initial work hardening rate, ε_p is the equivalent plastic strain and n is the work hardening exponent. The Voce law, [12], has an exponential form

$$\sigma_{\text{flow}} = \sigma_s - (\sigma_s - \sigma_Y) \exp\left(\frac{-\varepsilon_p}{\varepsilon_c}\right) \quad (2.6)$$

where σ_s is a saturation stress and ε_c the characteristic strain for the exponential approach towards this stress level. Although entirely empirical, these constitutive laws can reliably capture the (true) stress-strain behaviour of many metals.

2.1.1 Deviatoric (von Mises) stress

In the simulation of plasticity, the deviatoric (shape-changing) component of the stress state will determine if a plasticity may occur. If the magnitude of this, often captured in the form of the von Mises stress (a scalar), surpasses the yield stress, then the criterion for onset of plasticity is met [13]. The von Mises stress can be thought of as a volume-averaged shear stress. It is given by

$$\sigma_{\text{VM}} = \sqrt{\frac{(\sigma_1 - \sigma_2)^2 + (\sigma_2 - \sigma_3)^2 + (\sigma_3 - \sigma_1)^2}{2}} \quad (2.7)$$

where σ_1 , σ_2 and σ_3 are principal stresses. As is the case with shear stresses, the von Mises stress is conventionally treated as a positive value. The hydrostatic stress, given by

$$\sigma_H = \frac{(\sigma_1 + \sigma_2 + \sigma_3)}{3} \quad (2.8)$$

can be either positive or negative. In this way, it differentiates between compressive and tensile stress states. The independence of the von Mises from the hydrostatic stress suggests the (uniaxial) tensile and compressive response should be the same, which is broadly observed.

2.2 An Introduction to Creep

Plasticity and elasticity describe an effectively instantaneous response of a material to a stress. Elastic strain is recovered when the stress is removed, whereas plastic strain is not – the state of the material has been changed. Time-dependent permanent deformation of a metal subjected to a stress below the yield stress is often known as creep. As with plasticity, creep deformation is stimulated solely by the presence of a deviatoric stress, with deformation occurring at constant volume [14, 15].

The effects of creep are an important consideration for many high temperature applications (aerospace, engine design and turbine blades). The homologous temperature (absolute operating temperature divided by absolute melting temperature) provides a good indicator for material suitability. In general, the creep strain rate becomes significant above a homologous temperature of around 0.3 [16], although this can be improved in some cases.

A typical set of tensile creep curves, for two stresses ($\sigma_1 > \sigma_2$), is shown in Figure 2.2. The terms primary, secondary and tertiary are often used to differentiate the different observed regimes. The primary regime is often associated with the setting up of a mechanistic balance. The form of this behaviour is dependent on the stress, temperature and time. This often approaches a steady-state secondary creep regime, with characteristics dependent on temperature and stress [14]. It is important to note that the distinction between these two regimes is often poorly-defined and it is often unclear whether a true steady state is really achieved.

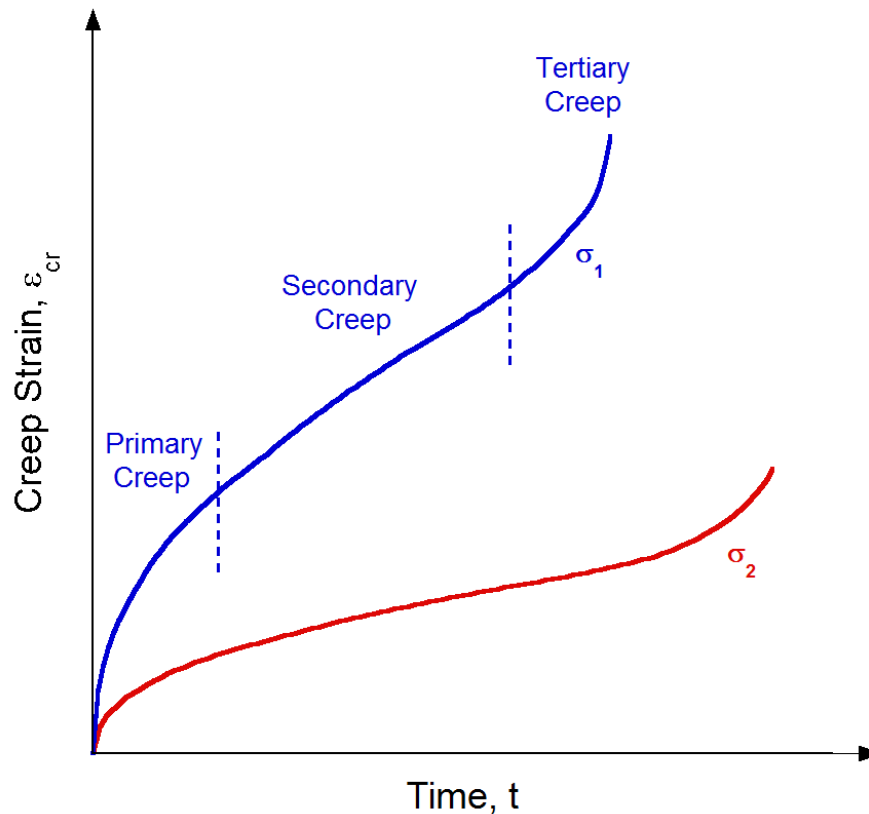


Figure 2.2 A typical set of creep curves for uniaxial tests measured at a single temperature, where $\sigma_1 > \sigma_2$.

Tertiary creep behaviour, where creep rates begin to increase with time, is often seen. This is often the case for tensile constant load creep tests, where an increase in creep rate can be explained by the true stress rising well above the nominal stress, as the cross sectional area drops with increasing creep strain. At the point of failure for such a test, a necked region may form and/or internal voids may have begun to coalesce [17]. This region is often short-lived, leading to the failure of the tensile specimen. The details of microstructural development (for example recovery and recrystallization) may also be significant to observation of a tertiary creep regime.

2.2.1 Mechanisms

The detailed mechanisms for creep tend to be complex. They are all inherently dependent on diffusion, which explains the time dependent nature of creep [18]. It is clear that temperature and stress have an effect on the dominant mechanism [15].

2.2.1.1 *Coble and Nabarro-Herring (Diffusion) Creep*

For stresses well below the yield stress, creep often solely occurs by the redistribution of atoms (and molecules) via diffusion [19]. This migration is driven by the applied stress, which sets a gradient in the hydrostatic stress component. For a tensile loading arrangement, hydrostatic tension will be created in the “polar” regions and hydrostatic compression in the “equatorial” regions of a grain. In this case, an overall change in shape is achieved by net the movement of atoms from the equatorial regions of the grain (more crowded) to the polar regions (less crowded), leading to the elongation of grains.

At high temperatures, Nabarro-Herring (N-H) creep often dominates [20, 21]. Higher homologous temperatures mean that diffusion of atoms can readily occur through the bulk. At low temperatures, Coble creep often dominates, with diffusion predominantly occurring via fast diffusion pathways (grain boundaries and dislocations) [22]. These pathways are more crystallographically disordered than the bulk, with lower activation energies for diffusion. Whilst the flux of diffusion through these regions will always be larger, bulk diffusion has a larger associated volume. It can therefore be expected that a finer grain structure will favour Coble creep over N-H creep.

2.2.1.2 *Dislocation Creep*

At higher stresses, it is common for creep to occur through the motion of dislocations. Several mechanisms have been identified for this behaviour [23-25]. However, they all involve some combination of dislocation climb and glide. When held up by an obstacle, climb processes facilitate the progressive motion of dislocations, such that a macroscopic permanent deformation is observed at stresses below the yield stress. Climb occurs through the emission and absorption of vacancies or interstitials at the dislocation core [26], allowing it to migrate to neighbouring slip planes. In this way, obstacles may be circumvented. It is generally assumed that these obstacles are immobile dislocations termed Lomer locks [27], created when two dislocation combine to produce sessile dislocation. In the same way that a mechanistic balance can achieved to a give a stress-strain plasticity response with (effectively) zero work hardening, a steady state creep rate is usually approached [23].

As with diffusion creep, high temperature and low temperature regimes exist for dislocation creep. At high temperature, bulk diffusion dominates. At low temperatures, the prominent fast diffusion pathway is along the core of the dislocation.

2.2.2 *The Effect of Microstructure*

At high temperature and over extended time periods (as is common for a creep test), changes in microstructure has the potential to be significant to the creep response [28]. It can be expected, particularly for dislocation creep, that the dislocation density will be relevant to observed creep rates. Whilst this may occur through a change in the balance between dislocation generation and annealing processes, a more dramatic effect may be seen if recovery or recrystallization is observed. In this instance, grain size will also be significant.

2.2.2.1 *Dynamic Recovery and Recrystallization*

Dynamic recovery and recrystallization are important factors in the creep response of metals [29, 30]. In high stacking fault materials, dynamic recovery effects act against those of straining such that a stationary state may be achieved [31]. This effect is commonly seen in the flow stress response of materials where work hardening rates often drop off with further straining. It is more commonly seen in materials with a high dislocation density, subject to a homologous temperature of ~ 0.3 or higher. Recovery is driven by a reduction in the overall internal stored strain energy by the rearrangement of defects - dislocations rearrange to annihilate completely and form arrays termed “sub-grains”. This leads to a slight drop in overall dislocation density. [32].

For materials with a low stacking fault energy, dislocations densities rise to high levels on straining which promotes dynamic recrystallization [31]. This process requires higher homologous temperatures (~ 0.6) and leads to a significant drop in dislocation density, particularly in heavily cold-worked material. This is achieved by the nucleation and growth of favourably oriented sub-grains following recovery. This leads to the formation of a significantly refined grain structure with high angle grain boundaries, which allows subsequent grain coarsening to occur rapidly [33, 34]. The drop in dislocation density is dramatic, and so the yield stress drops.

2.2.3 Conventional Creep Testing

In order to rank materials for applications where creep is significant, it must be possible to effectively characterise the creep behaviour. This is not necessarily straightforward, partly because testing can require high temperatures.

Conventional, constant (nominal) stress creep tests involve the application of a constant load under uniaxial loading conditions (tension or compression). It is generally assumed that no creep strain is accumulated whilst the sample is loaded, which is approximately true if loading is done sufficiently quickly. Whilst this sort of test is often not conducted as constant true stress, due to the effect of creep strain on stress levels at constant load, constant true stress is often assumed. This is a good approximation for low strain levels [35-38].

The stress relaxation test is an alternative loading arrangement that may be used to probe the creep response. This type of test is generally less popular for characterising the creep behaviour of metals due to compliance complications introduced by varying the load. The idea is to maintain constant strain in the sample by relaxing the applied stress/load [39].

2.2.4 Constitutive Laws for Creep

In many cases, the primary and secondary creep characteristics of a material will together describe the creep response in a range that useful for engineering purposes, given the association of tertiary creep with imminent failure. The Miller-Norton (MN) creep law is a popular expression that captures both primary and secondary creep regimes [40]

$$\varepsilon_{cr} = \frac{C_1 \sigma^{n_2} t^{m_2+1} \exp\left(\frac{-Q}{R_{gas} T}\right)}{m_2 + 1} \quad (2.9)$$

where C_1 is a constant, n_2 in the stress exponent, m_2 is the time exponent, Q is the activation energy (diffusion), R_{gas} is the gas constant and T is the local temperature. A creep strain rate can be found from

$$\dot{\epsilon}_{cr} = C_1 \sigma^{n_2} t^{m_2} \exp\left(\frac{-Q}{R_{gas} T}\right) \quad (2.10)$$

For characterising Q , creep tests are carried out at different temperatures. In taking the natural log of Equation 2.10, we get

$$\ln(\dot{\epsilon}_{cr}) = \ln(C_1) + n_2 \ln(\sigma) + m_2 \ln(t) - \left(\frac{Q}{R_{gas} T}\right) \quad (2.11)$$

It can be seen that a plot of $\ln(\dot{\epsilon})$ vs $1/T$ will have a gradient of $-Q/R_{gas}$, at a given time, for a given applied stress. If a sufficient range of temperature is well sampled, a form shown in Figure 2.3 is expected. A transition between bulk diffusion dominating at high temperatures and fast diffusion pathways dominating at low temperatures is shown [41].

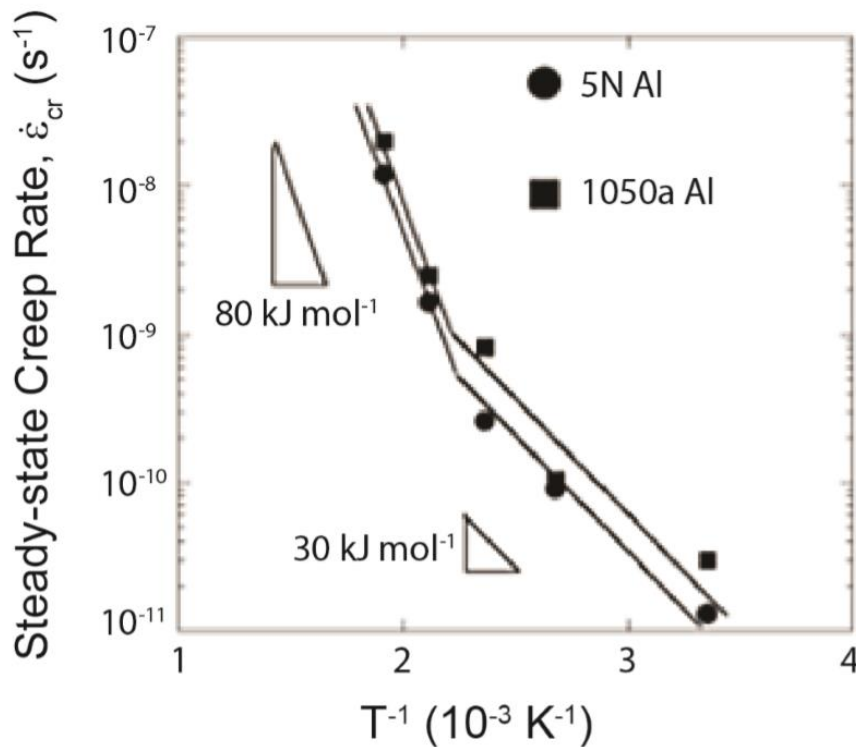


Figure 2.3 Arrhenius plot for the calculation of Q for two aluminium alloys. A transition is observed between “lattice” diffusion and fast pathway “defect” diffusion [41].

For tests carried out at a single temperature, Equations 2.10 and 2.11 may be simplified to

$$\dot{\epsilon}_{cr} = C_2 \sigma^{n_2} t^{m_2} \quad \text{and} \quad \ln(\dot{\epsilon}_{cr}) = \ln(C_2) + n_2 \ln(\sigma) + m_2 \ln(t) \quad (2.12)$$

where C_2 represents the product of the exponential term and C_1 .

Although the creep rates are higher in the primary creep regime, it is common for it to be neglected in characterisation. This is because the time over which the secondary (steady state) creep response can act is often much larger. This therefore has the potential to contribute far more to the overall creep strain. Following the assumption that the strain rate in the secondary (steady state) creep regime is time independent, Equations 2.10 and 2.11 can therefore be simplified to give

$$\dot{\epsilon}_{cr} = C_3 \sigma^{n_2} \exp\left(\frac{-Q}{R_{gas} T}\right) \quad \text{and} \quad \ln(\dot{\epsilon}_{cr}) = \ln(C_3) + n_2 \ln(\sigma) - \left(\frac{Q}{R_{gas} T}\right) \quad (2.13)$$

where C_3 represents the product of the time term and C_1 . Again, if considering a single temperature, this can be simplified to the following

$$\dot{\epsilon}_{cr} = C_4 \sigma^{n_2} \quad \text{and} \quad \ln(\dot{\epsilon}_{cr}) = \ln(C_4) + n_2 \ln(\sigma) \quad (2.14)$$

where C_4 represents the product of the exponential term and C_3 . In this way, the stress exponent can be extracted by carrying out uniaxial tests at several stress levels and plotting $\ln(\dot{\epsilon})$ against $\ln(\sigma)$. In increasing the stress, a transition is expected from diffusion creep to dislocation creep. In the diffusion creep regime, $n_2 \sim 1$. Dislocation creep generally has a higher sensitivity to the stress, with n_2 values in the range 2 – 5 common, though they can approach 10. A plot of the form shown in Figure 2.4 may be expected.

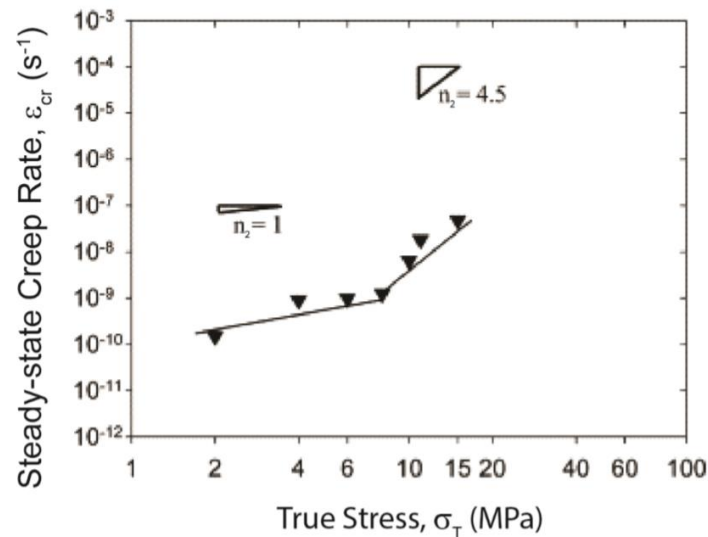


Figure 2.4 Measurement of the stress exponent, n , demonstrating greater sensitivity to the stress at high stresses, with $n_2 \sim 1$ for $\sigma < 10\text{MPa}$ and $n_2 \sim 4.5$ for $\sigma > 10\text{MPa}$ for a polycrystalline copper, measured at 723K [42].

It is worth noting that constant true stress levels are often not achieved, since setting up a test to do this is more complex than merely applying a constant load. For constant true stress levels, a feedback loop is necessary to monitor the strain and change the load accordingly. Tests are therefore based on engineering stress levels. Numerical FEM modelling is inherently based on true stress levels, so care is necessary when comparing to simulation with input parameters directly from fitting to experimental uniaxial creep test data. This effect is also evident when comparing measured creep curves from tension and compression tests, where, for the same true stress and temperature, they should agree fairly well. Instead, the accumulated creep strain will diverge with time, as the true stress increases in a tensile sample and decreases in a compressive sample. Compression tests involve friction between platens and specimen, which acts to slow down the creep rate [37, 43]. The effect of friction can easily be incorporated into an FEM analysis. In neglecting these effects, as is common, considerable errors may be introduced [43].

Chapter 3

The Effect of High Imposed Strain Rate on Plasticity and Fracture

There is considerable interest in characterising the high strain rate mechanical response of materials. Research and development of materials and components in high strain rate environments (ballistic events, armour, explosives, crash mechanics etc. [44]) is often destructive and costly. Simulations can cut down on this cost, however, for this to be effective, an appropriate high strain rate plasticity constitutive law must be identified and the parameters well characterised. The complexity of the high strain rate response of metals has led to a number of constitutive laws, with varying degrees of complexity and success. This is partly related to changes in plasticity response at high strain rates [45-47]. The inclusion of fracture and the modelling of crack propagation introduces another level of complexity [48-50].

3.1 Dynamic Plasticity

It is well established, at least at relatively high strain rates, that the relationship between flow stress and plastic strain is dependent on the strain rate [51], as in Figures 3.1 and 3.2. It is generally found that the yield stress and work hardening rate increase with increasing strain rate. Figure 3.2 presents data collected with Hopkinson bar [52], a method which is often used to explore the behaviour at strain rates up to around 2000 s^{-1} . At such strain rates, elastic and plastic wave propagation can affect the material response. A thermodynamic transition from isothermal to adiabatic deformation is also observed as conduction of heat away from locally deforming sites becomes slow, relative to the rate of deformation. Typically, 95% of plastic work is converted into heat [53]. Temperature rises under high strain rate conditions are therefore difficult to avoid and isolating the effect of strain rate can be problematic. If the effect of thermal softening

outweighs that of strain and strain rate hardening, an unstable, inhomogeneous plastic flow process can lead to the presence of adiabatic shear bands. These regions of intense plastic shear deformation are observed in many metals and are generally well understood [53-55].

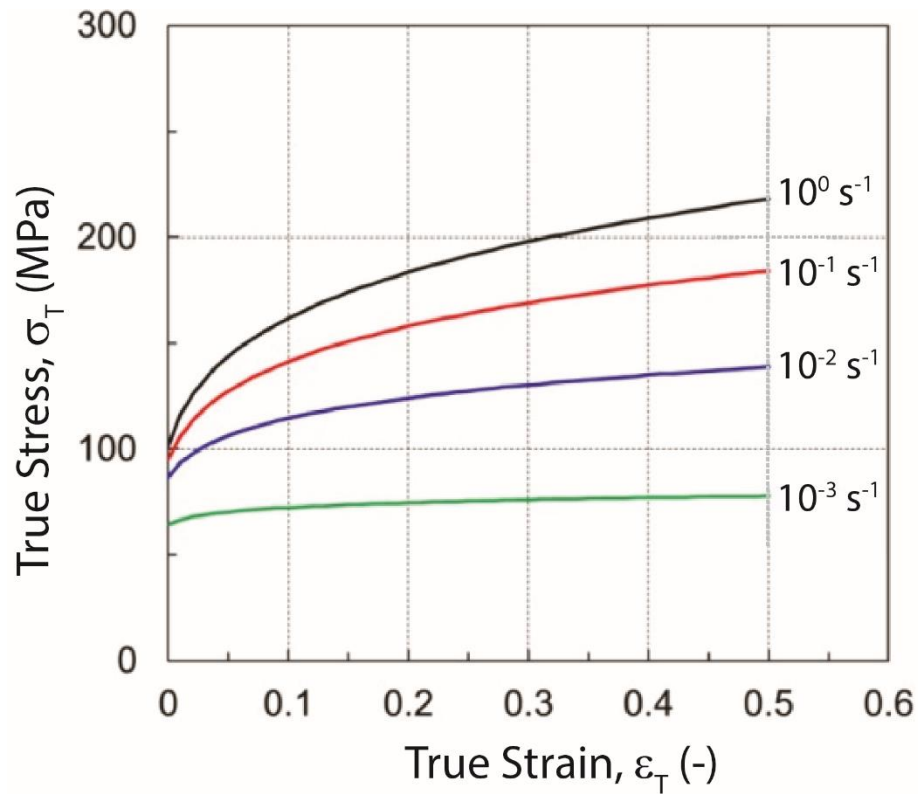


Figure 3.1 True stress vs true strain curves for AZ31B magnesium alloy at varying strain rates from uniaxial tensile testing at 250 °C [56].

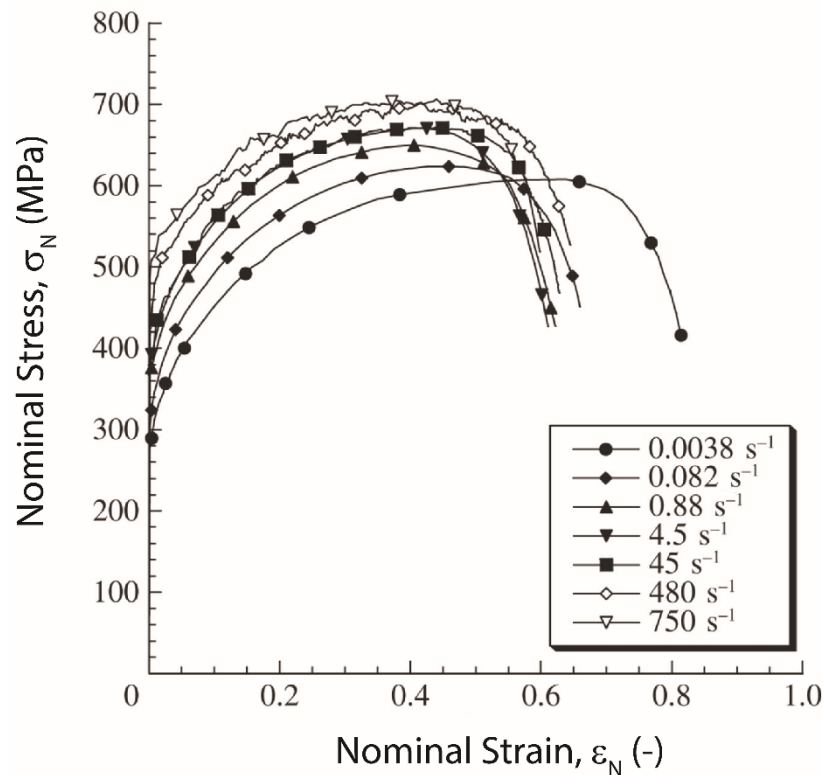


Figure 3.2 Flow behaviour of ASIS 316H stainless steel at different strain rates from room temperature Hopkinson bar testing [52].

3.1.1 Plasticity Mechanisms

The mechanisms responsible for plastic deformation when a stress is applied include; dislocation slip, twinning and shear phase transformations. Depending on the alloy and loading conditions, these may be present in different ratio. At quasi-static rates, slip is often the principal mechanism of plastic deformation. It relies on the presence of dislocations and their movement (glide) within the crystal structure. Dislocation glide commonly occurs in specific crystallographic directions and on specific crystallographic planes (together termed “slip systems”) [57]. These are commonly close-packed planes and directions (or the closest packed ones that are available). Von Mises demonstrated how a material must have five independent slip systems to accommodate plastic deformation [58], which is a feature of face centre cubic (FCC) and body centre cubic (BCC) crystal structures. At higher stresses, it is possible for slip planes with lower packing efficiencies to be activated to accommodate plastic deformation [59].

Dislocation motion can also occur by cross-slip (allowing a change of glide plane) and by climb. The latter involves absorption or emission of vacancies and so is thermally activated – it often makes important contributions to dislocation motion at high temperatures and is strongly involved in many creep processes [60-62].

There are various origins for strain rate hardening behaviour. Most notably, it can be put down to the suppression of dislocation mobility at high strain rates [63]. At very low, quasi-static strain rates, the effect of strain rate is negligible (assuming the effects of creep can be ignored). At intermediate strain rates, thermal activation will begin to influence stress-strain characteristics. At high strain rates, viscous drag mechanisms are thought to limit the mobility of dislocations.

Glide has little thermal activation and so can occur over a wide range of temperature, but, on average, takes place relatively slowly and so in many cases cannot deliver plastic straining at very high strain rates. Subsequently, at high strain rates, or in other situations where dislocation mobility is limited (e.g. low T, limited slip systems), mechanical twinning can contribute to plastic deformation of metals [64-66]. Twinning is more common in metals with low symmetry crystallographic structures, in which there are often a limited number of (low energy) slip systems available and those that exist are often more difficult to activate. Common examples include hexagonal metals such as zinc and magnesium, and tetragonal metals such as tin [65]. Deformation twins occur via the cooperative shear of atomic layers over sub atomic distances within a parent grain, such that a region is created in which the crystal structure is the same as that of the parent, but in a different orientation (mirrored across a twin plane) [64]. The motion of atoms during this process is rapid (~speed of sound in the material) so deformation twins form very rapidly. The overall shape they form is dictated by a minimisation of the overall free energy. Interfacial energies are minimised by the formation of coherent twin boundaries that do not deviate from a given plane [64]. In the case of a single crystal, deformation twins will therefore form planar twin boundaries, as seen in annealing twins (which form by a reconstructive process). In a polycrystalline material, elastic strain energy in both the parent and twinned material acts to impose constraints on the shape of the twin. These two energy considerations

often give rise to a discoidal structure that has predominantly planar coherent boundaries within the grain and comes to a sharp point at the grain boundaries. This can be seen in Figure 3.3. Grain size, twin boundary energy and temperature are other factors that can affect the prevalence of twinning [64].

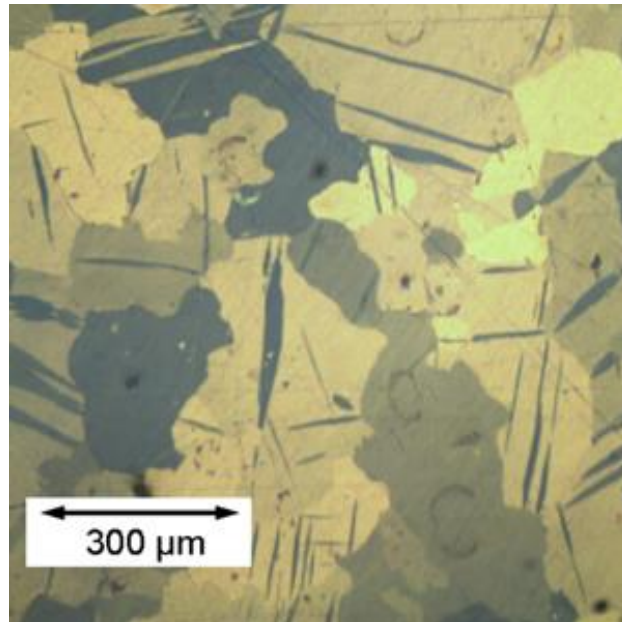


Figure 3.3 Cold rolled zinc microstructure showing deformation twins. From <http://www.doitpoms.ac.uk/tlplib/artefact/metals.php>.

Martensitic transformations are a form of phase transformation induced by shear. Much like twinning, they occur via systematic shear of atomic planes – but in this case, the product has a new crystal structure (rather than the same one in a new orientation). This too takes place very rapidly [66].

Thermal softening of metallic materials describes the drop in yield stress observed as the temperature is increased. For FCC metals, thermally activated dislocation motion generally dominates at lower temperatures, with diffusion controlled mechanisms activated as the temperature approaches the melting point. Athermal regions are sometimes seen at intermediate temperatures [67].

The effect of thermal coupling, and the many potential mechanisms, complicates plasticity at high strain rates. It is not surprising that a variety of strain rate sensitive effects are observed in different metallic materials. For instance, a dramatic increase in

sensitivity of the flow stress to a change in strain rate has been reported at high strain rates in testing of 316L steels [68], there are reports of cold work reducing the strain rate sensitivity in steels [69] and finer grain structures in FCC metals have been reported to increase the strain rate sensitivity [70].

Further thermal complications are found in the secondary effects of dynamic recovery and recrystallization. The high dislocation densities and homologous temperatures (~ 0.3) that develop during high strain rate deformation create a significant driving force for these to occur [71, 72]. The degree of cold-work will dictate the driving force for both processes, as the potential to lower the internal strain energy of the system becomes greater. This is true of materials during deformation, with the work hardening rate tailing off as the effects of recovery and dislocation density equilibrate. This equilibration is dependent on the strain rate and the temperature [31]. Deformation history and the microstructural developments associated with recovery and recrystallization may therefore be important, but are seldom considered in high strain rate plasticity constitutive relations [73, 74].

3.2 Strain Rate Sensitive Plasticity Characterisation

3.2.1 Constitutive laws

Robust modelling procedures require this behaviour to be captured effectively. This has implications for a variety of applications where strain rates and temperatures are high - notably aerospace engineering, ballistics and crash mechanics (e.g., the automotive industry) [44]. The effect of strain hardening, which is crucial to path-dependent material behaviour, is often captured with power law or exponential expressions, such as Ludwik-Holloman and Voce. Under high strain rate conditions, strains can often reach values exceeding 100% [45, 46]. It is important that parameters characterising the strain hardening behaviour are representable when extrapolated to such high strains.

The coupling of temperature and high strain rates, and the effect they have on plastic flow, complicates characterisation. Operative mechanisms can be expected to change

over a range of strain rates, with a switch from slip to twinning or martensitic phase transformations dominating as the strain rate rises [64]. The crystal structure, microstructure and conditions can all influence this transition. Capturing this behaviour in a single model over a large range of temperature and strain rate is not a trivial task. There are a number of constitutive laws that exist (empirically, phenomenologically and physically based) [73, 74]. However, none are completely satisfactory for all materials and conditions. It is also common for modifications to be made to existing constitutive laws, such that they can better fit a data set [75-77].

3.2.1.1 *Mechanism-based Laws*

Despite various attempts [73, 74], there are no models that successfully predict mechanical behaviour from a knowledge of microstructure and deformation mechanisms. Expressions are often complicated and contain multiple parameters. Parameterisation and computational implementation are subsequently demanding. Additionally, for a given set of parameters, these expressions are often limited in the range of strain, strain rate and temperature for which they are valid.

The Zerilli-Armstrong (ZA) formulations for flow stress were developed with a focus on the effect of dislocation mechanics. They include sensitivity to grain size and account for the effect of crystal structure on dislocation mechanics, with relations for both FCC and BCC structures. ZA can be represented by

$$\sigma_{\text{flow}} = A_a + A_1 \varepsilon_p^n \exp(-A_2 T + A_3 T \ln \dot{\varepsilon}_p) \quad (3.1)$$

which gives parameters A_1 , A_2 , A_3 and n_2 to be identified. A_0 is an athermal component given by

$$A_a = \sigma_g + \frac{k_h}{\sqrt{\lambda}} \quad (3.2)$$

where σ_g is an additional stress component, k_h is a microstructural stress intensity and λ is the average grain diameter.

The mechanical threshold stress (MTS) formulation is one that has received a lot of attention [73, 74]. It considers a mechanical threshold stress term, defined at 0 K, as an

internal (microstructural) state variable, from which a flow stress is found by accommodating thermal softening with an Arrhenius term. This Arrhenius term accounts for thermally activated dislocation motion [51]. The MTS has the form

$$\sigma_{\text{flow}} = \sigma_a + (S_i \sigma_i + S_e \sigma_e) \frac{g(p, T)}{g_0} \quad (3.3)$$

where σ_{flow} is the flow stress, σ_a is the athermal component of mechanical threshold stress, σ_i is the component of the flow stress due to intrinsic barriers to thermally activated dislocation motion and dislocation-dislocation interactions, σ_e is the component of the flow stress due to microstructural evolution with increasing deformation, S_i and S_e are temperature and strain rate dependent scaling factors (Arrhenius in form), $g(p, T)$ is the shear modulus as a function of pressure and temperature and g_0 is shear modulus at 0 K and ambient pressure.

ZA and MTS provide a fairly comprehensive overview of the “physically-derived” strain rate sensitive plasticity constitutive laws. They are generally cumbersome and modifications are often necessary to achieve acceptable accuracy. More recently, models have been developed with modelling and ease of parameterisation in mind [79-81].

3.2.1.2 *The (Empirical) Johnson-Cook Constitutive Law*

Empirical constitutive laws are derived from the fitting of experimental data. By far the most popular constitutive law is the entirely empirical Johnson-Cook (JC) model [82]. The JC expression is multiplicative, lending to its simplicity in implementation and parameterisation. It has the form

$$\sigma_{\text{flow}} = \left[A + B(\varepsilon_p)^n \right] \left[1 + C \ln(\dot{\varepsilon}_p^*) \right] \left[1 - (T^*)^m \right] \quad (3.4)$$

where ε_p is the equivalent plastic strain and A , B , C , n and m are constants. The terms

$$\dot{\varepsilon}_p^* = \frac{\dot{\varepsilon}_p}{\dot{\varepsilon}_{p0}} \quad \text{and} \quad T^* = \frac{(T - T_0)}{(T_m - T_0)} \quad (3.5)$$

where $\dot{\varepsilon}_p$ is the equivalent plastic strain-rate, $\dot{\varepsilon}_{p0}$ is the effective (reference) plastic strain-rate, T_0 is a reference temperature and T_m is the melting temperature. For this

particular model, there are 8 parameters to be found with T_m being the only one with any physical meaning, though A , B and n can be considered to be the conventional quasi-static plasticity parameters, σ_Y , K and n , respectively, as presented in Equation 2.5. This simplifies matters. The form of the JC model is such that it is divided into three uncoupled functions (by the square brackets in Equation 3.4). These independently account for deviations in flow stress due to changes in the equivalent plastic strain (quasi-static case), strain rate and temperature. These have three (A , B and n), two (C and $\dot{\epsilon}_{p0}$) and three (m , T_0 and T_m) parameters associated with them, respectively. This simplifies optimisation somewhat, since the effect of varying the strain rate depends only on the parameter C . The form of the JC model, and the sensitivities to C and m are illustrated in Figures 3.4 - 3.6. In each case, the same parameter values for A (500 MPa), B (500 MPa), n (0.5), T_0 (300 K) and T_m (1000 K) have been used. In Figure 3.4, a reference case is presented, for which a strain rate sensitivity value of 0.05 has been chosen. This represents a relatively standard sensitivity to the strain rate. In Figure 3.5, parameter m has been decreased to yield a pronounced increase in the sensitivity to temperature, with the flow stress dropping and the material behaving more softly. In Figure 3.6, C is decreased to give a less pronounced hardening effect as strain rate increases. This is why little separation in the curves is seen despite strain rates varying over four orders of magnitude.

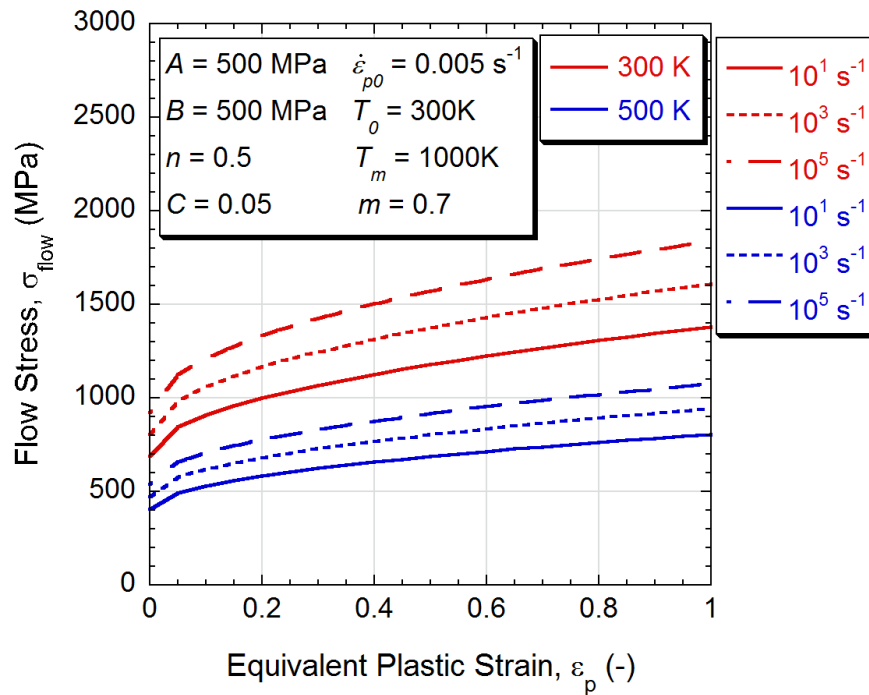


Figure 3.4 JC stress strain curves with reference parameter value set for two different temperatures. In considering a single temperature, the effect of the strain rate hardening can be seen. The effect of thermal softening is also captured.

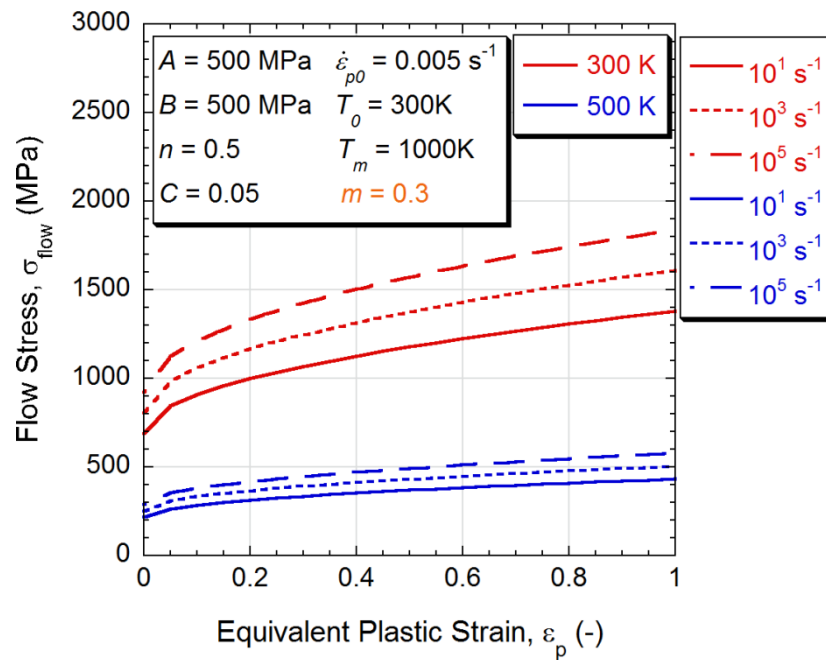


Figure 3.5 JC stress strain curves with a reduced m , demonstrating the sensitivity of the JC formulation to m (by comparison with Figure 3.4).

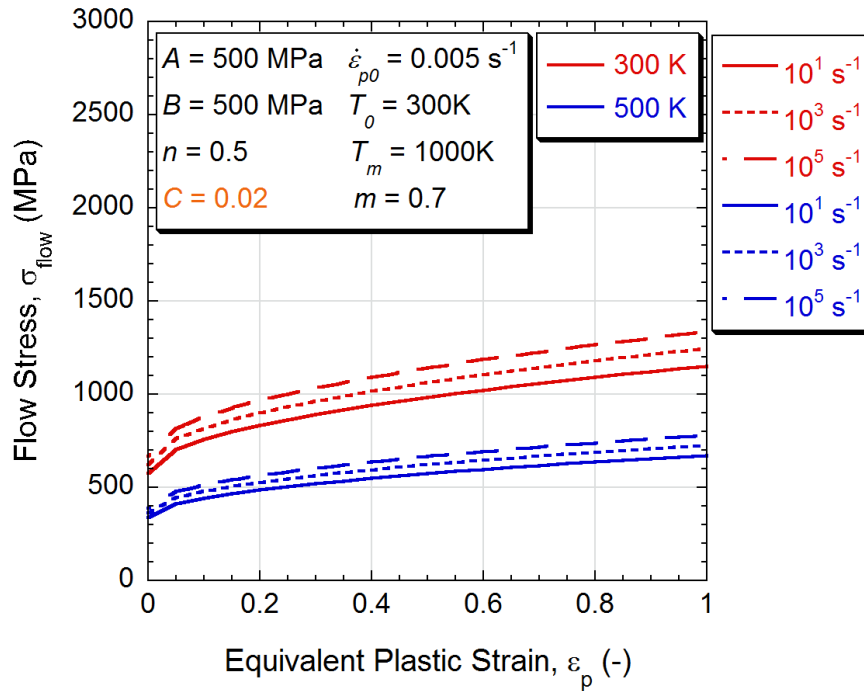


Figure 3.6 JC stress strain curves with a increased C , demonstrating the sensitivity of the JC formulation to C (by comparison with Figure 3.4).

When both strain rate and temperature are considered, an abundance of procedures for evaluating the JC parameters are available [83]. The assumption that the effects of temperature and strain rate can be optimised and considered independently gets progressively less valid as the strain rate is increased. This is not surprising, given that roughly 95% of plastic work is converted to heat in the deformation process [53], since higher strain rates will further limit the time this has to diffuse away from areas where local plastic deformation is high. This ultimately results in a large change in temperature local to deforming areas in experiments, such as impact testing. This is termed thermal softening [84].

With no prior knowledge, experimental stress-strain hardening data needs to be collected at various strain rates and temperatures. Optimisation generally begins by setting T_m equal to the melting temperature. Next, a “quasi-static” experiment at low strain rates and temperature is carried out. Parameters A , B and n are fitted to this curve. It is also not uncommon for A to be set equal to the yield stress [85]. The strain rate and temperature used for this “quasi-static” case become the reference values $\dot{\varepsilon}_{p0}$ and T_0 , respectively. The strain rate sensitivity parameter (C) and temperature parameters (m)

are then independently optimised with a set of hardening functions taken at either T_0 and $\dot{\epsilon}_{p0}$, respectively, whilst varying the other. For the strain rate parameter, this will involve a set of functions of varying $\dot{\epsilon}_{p0}$ at temperature T_0 [44, 47]. An overview of 5 popular methods for parameter optimisation is given in [83].

It is generally considered that the physically derived models (MTS, ZA, etc.) will produce a more accurate representation of high strain rate plasticity behaviour, particularly for FCC metals [85]. This was supported in a study comparing the JC, a modified ZA and an Arrhenius-based equation in modelling experiments that varied both strain rate and temperature, reporting better agreement with experimental data with the modified ZA and Arrhenius-based formulations, stating that the JC model was inadequate in accounting for the coupled effects of strain rate and temperature in a 9Cr-1Mo steel [75]. In a comparison of the popular JC and MTS models, it was found that they performed very similarly over a large range of strain rates, with the MTS model allowing for easier parameter optimisation and the JC model faster simulations [86]. Given the inclusion of the JC model in the ABAQUS software suite and its generally well-documented success, it has been chosen for use in the initial stages of this project.

3.2.2 *Conventional Testing Methods*

Although it has long been known that the dynamic mechanical response of metallic materials differs from the quasi-static response, experimental capability limited study until the advent of the Hopkinson pressure bar (HPB) in 1905 [87]. This setup was designed to study the wave propagation phenomena following impact. It wasn't until 40 years later that a quantitative approach for plasticity parameter evaluation was developed by Taylor [88]. Kolsky developed the split Hopkinson pressure bar (SHPB) technique shortly after, claiming the advantages of more uniform stress fields and strain rates [89]. These both relied on analytical expressions and made rather crude assumptions to evaluate stress-strain characteristics at high strain rates [90].

Practically, it is possible to use conventional uniaxial testing [91], although this presents severe experimental difficulties at strain rates above about 10^3 s^{-1} (which is the regime where departure from quasi-static behavior starts to become significant [92]). The most common approach is still the split Hopkinson bar (SHB) test [93, 94] and the

Taylor cylinder test [95-97], where relatively high strain rates ($\sim 10^3 - 10^5 \text{ s}^{-1}$) are observed, although they are subject to some uncertainty, arising from various sources [98, 99]. Nevertheless, values of C have been obtained many times [100-104] in this way for different metals, ranging in magnitude from about 0.001 to around 0.05.

The SHPB involves sandwiching a specimen between two bars (the incident and transmitted bars, designed to remain elastic throughout the test) and sending a stress wave through the system, such that a transmitted portion of this wave travels through the specimen (usually cylindrical) and then the transmitted bar and, in the process, causes plastic deformation of the specimen [105]. Strain gauges are then set-up to measure the strain in the incident pulse, ε_{inc} , the reflected pulse, ε_{ref} , and the transmitted pulse, $\varepsilon_{\text{trans}}$. Full analysis, found in [106], gives the following analytical equations for the nominal strain rate, strain and stress

$$\dot{\varepsilon}_{\text{psN}} = \frac{-2\varepsilon_{\text{ref}}}{L_s} \sqrt{\frac{E_b}{\rho_b}} \quad (3.6)$$

$$\varepsilon_{\text{psN}}(t) = \int_0^t \dot{\varepsilon}_{\text{psN}}(\tau) d\tau \quad (3.7)$$

and

$$\sigma_{\text{sN}} = \frac{E_b \psi_b}{\psi_{\text{sO}}} (\varepsilon_{\text{trans}}) \quad (3.8)$$

where the subscripts b, s, p, N, T and O refer to the bar, specimen, plastic, nominal values, true values and original values, respectively, Ψ is the cross-sectional area, L_s is the specimen length and τ has been introduced as a dummy time variable. This is then converted to true strain rate, true strain and true stress by

$$\dot{\varepsilon}_{\text{psT}} = \frac{\dot{\varepsilon}_{\text{psN}}}{1 - \varepsilon_{\text{psN}}} \quad (3.9)$$

$$\varepsilon_{\text{psT}} = -\ln[1 - \varepsilon_{\text{psN}}] \quad (3.10)$$

and

$$\sigma_{sT} = \sigma_{sN} (1 - \varepsilon_{psN}). \quad (3.11)$$

Several assumptions are normally made in this analysis. These are that [107]:

- a) A stress equilibrium has been reached - that is to say the forces on the two ends of the specimen are the same;
- b) The interfaces are frictionless;
- c) The specimen deforms at constant volume;
- d) Uniaxial stress conditions apply;
- e) 1-D wave propagation occurs in the bars without dispersion.

These assumptions are not entirely satisfactory. It has been shown, for example, with FEM analysis that inhomogeneous deformation occurs within the specimen [108]. Other limitations include the ability to only test materials with a yield stress below that of the test bars, the influence and treatment of thermal softening and the small imposed strains (many high strain rate applications require stress-strain descriptions up to large strains) [109, 110].

3.2.3 *Characterisation by Inverse Finite Element Method*

The inverse FEM procedure allows for the evaluation of material property parameters from the outcomes of a given experiment. Whilst conventional methods rely on geometries that enable the application of analytical equations for the analysis of experimental data, the numerical aspect of inverse FEM means experimentation is not constrained in this way, allowing much simpler and more versatile testing arrangements with arbitrary geometry and external conditions. Indentation is an example of this, however, there are examples of many experimental procedures being used for the evaluation of many different property parameters values [45, 46, 111-114]. It should be noted that, whilst conventional methods are often uniaxial in form and can readily measure anisotropy in materials through testing in different orientations, experiments such as indentation probe a multiaxial response. This makes the study of anisotropy more complex and introduces a potential source of error when compared with uniaxially

measured material property values (the indentation inferred plasticity response would represent some average of tensile test data from the different directions [3]). It is, however, common for modelling problems to be simplified with an isotropic material property description where multiaxially measured material property data may be more appropriate. Additionally, testing may probe a range of the material response that is not possible with uniaxial testing – for instance, plasticity descriptions beyond a few percent strain, where necking may limit uniaxial test data.

The concept of inverse iterative FEM is simple. An experiment (such as an indentation test) is carried out and an outcome (such as a load-displacement plot or a residual indent profile) is obtained. The test is modelled with FEM, using trial material property parameter values (such as the σ , K and n in the Ludwik-Holloman plasticity formulation). A comparison is then made between predicted and measured outcomes and an iterative process is employed to obtain “best fit” values of the property parameters [3]. The inverse FEM procedure is simple in principal, but a number of issues and factors are likely to affect the reliability and accuracy of the outcome.

Some of these factors relate to the FEM model (geometry, initial conditions, boundary conditions, mesh, materials properties and constitutive relations). The constitutive relation is clearly important. It needs to accurately capture the behaviour of the material over the range of conditions (stress, strain, temperature, strain rate, etc.) concerned [115]. Capture of the material response is always going to be limited to the fidelity with which it can be represented by the constitutive law. The mesh must be sufficiently fine to give mesh-independent results, without excessive demands on computing time. The boundary conditions must be well-defined - this is usually straightforward for indentation [3]. Central to the method is some sort of quantification of the level of agreement between measured and modelled outcomes.

Key issues include sensitivities and uniqueness. The experimental setup should be sensitive to the input property parameter values being sought [116]. Model sensitivity, which refers to the relative change in output with respect to a change in the input property data [117], is also important. A more sensitive experiment-model system is desirable, since it will result in a larger change of outcome with changing property

parameter values. This should in theory mean low errors, with inferred values being close to the “true” values. Tip geometry is an example of how this may be controlled for indentation experiments. Different tip shapes will result in different distributions in the stress and strain fields beneath the indenter tip and will therefore be sensitive to different proportions of the yield and work hardening behaviour [118].

Ideally, the inverse FEM procedure will identify a unique solution. That is, the procedure will converge on a single set of input property parameter values, giving the best agreement with experimentally acquired data. For scenarios with more than one unknown property parameter, it is possible that multiple combinations give equally good agreement. This can be the case for the extraction of plasticity property parameter values, where identification of a unique solution is sometimes difficult [119-124]. This issue relates to the nonconvex nature of an iterative inverse FE method, where multiple locally optimal parameter set values may be possible. This results in optimisation efficiency drawbacks and may lead to misleading results.

FEM is particularly useful for simulating high strain rate experiments [44, 85]. Generally, the stress, strain, temperature and strain rate fields will be non-homogeneous and will therefore require numerical analysis. Account can also be taken of friction and instability phenomena such as necking (tensile tests) and wave propagation (dynamic tests). Disadvantages include the computing power required and time taken for iterative simulation in inverse FEM (particularly as the set of parameter values to be optimised is large).

The JC constitutive law has been used extensively to simulate high strain rate experiments. This includes conventional techniques such as; HPB [44], SHPB [47, 96, 102, 103, 125], a specially designed direct-impact Kolsky bar device [126] and Taylor tests (ballistic) [127]. It has successfully captured the behaviour for a variety of materials, including steels [128], aluminium alloys [129] and oxygen-free copper [130]. Characterisation includes output data from machining [45, 46] and cutting processes [47].

There have also been FEM studies covering ballistic impact [B1-B4], with iterative simulation being used to obtain values of C giving the best fit between experimental and predicted outcomes (such as penetration characteristics, obtained via high speed photography). Such approaches have the capability to predict plastic flow characteristics at very high strain rates (up to 10 s^{-1}) with reasonable reliability.

3.3 Dynamic Fracture

There has been significant recent interest in the study of dynamic fracture. There are many technological applications where damage can result from rapidly applied loads (mining, explosives, ballistic munition, etc.). Simulating the fracture response of materials, however, is complex. Not only must a suitable failure criterion be identified and the fracture response be well characterised, but often, and particularly in the case of most engineering metals, a high strain rate plasticity description is simultaneously necessary. Ballistic impact provides a controlled way of imparting a finite amount of energy to a projectile, which will in some cases result in fracture. As such, it may be of some use in the characterisation of the dynamic fracture response of materials.

It is well-established that holes and cracks can act as stress concentrators. Inglis [B5] developed the following expression relating the stress at the tip of an ellipsoidal crack

$$\sigma_{\max} = \sigma_f \left[1 + 2 \left(\frac{c}{r} \right)^{1/2} \right] \approx 2\sigma_f \left(\frac{c}{r} \right)^{1/2} \quad (3.12)$$

where c is the crack length (internal length $2c$), r the tip radius and σ_f the far-field stress developed from a tensile load applied perpendicular to the plane of the crack. On moving away from the crack tip, the stress drops, approaching that of the far-field, applied stress at large distances. For a circular hole ($c = r$), there is a stress concentration factor of 3 at the crack tip. This is significant and will be larger still for sharp crack tips ($r \ll c$). In reality, however, engineering materials do not fail readily just because a sharp crack is present.

This observation was resolved by the pioneering work of Griffiths [B6]. He adopted an energy-based approach, stating that, for a crack to propagate, the overall energy of

the system must decrease. The strain energy released on propagating a crack provides the driving force, whilst absorption processes (creation of free surfaces, plasticity ahead of the crack tip, etc.) resist propagation.

Since the free surfaces of the crack are unable to support a normal stress, material in the proximity of the crack are “shielded” from the applied stress [136] . This leads to a region of low stress, which is seen to expand as the crack grows. During this expansion, strain energy is released according the equation

$$U = \frac{\sigma_f^2}{2E} \quad (3.13)$$

where U is the strain energy per unit volume and E is the Young’s modulus [136]. The shape of this stress free region can be reasonably approximated to an oval-like shape, with an area equal to twice that of a circle of radius c . This gives a strain energy release rate, G , calculated per (projected) unit area of new crack created

$$G = \frac{dW}{\text{new crack area}} = \frac{(2\sigma_f^2 \pi c t \, dc/E)}{(2t \, dc)} = \pi \left(\frac{\sigma_f^2 c}{E} \right) \quad (3.14)$$

where t is the plate thickness and W is the work done [136]. A critical strain energy release rate, G_c , describes the strain energy release rate required to supply the energy needed for crack propagation. For a “ideally” brittle material, a crack will propagate when

$$G \geq G_c = 2\gamma \quad (3.15)$$

where 2γ is the energy required to create two new surfaces in growing the crack (and this is the only active absorption process) [136]. G_c is a useful material parameter. It requires no prior knowledge of the crack tip geometry, which may undergo a degree of blunting upon loading prior to fracture initiation, or measurement of the true crack area, which is likely to be rough due to crack deflection mechanisms. From Equations 3.14 and 3.15, the critical stress at which fracture will occur, σ_* , can be predicted for a material containing a known flaw size

$$\sigma_* = \left(\frac{2\gamma E}{\pi c} \right)^{1/2} = \left(\frac{G_c E}{\pi c} \right)^{1/2} \quad (3.16)$$

In reality, engineering metals are not ideally brittle. Fracture is often preceded by plastic flow throughout and then locally at the crack tip [137]. In this way, energy is dissipated (predominantly as heat). Due to the stress concentration effect, plasticity in the proximity of the crack tip is often unavoidable. A “plastic zone” develops as material plastically flows, which may involve some degree of work hardening of the material, raising the local flow stress. The plastic flow will often act to blunt the crack tip, reducing the stress concentration effect [138]. Equations 3.15 and 3.16 are often adapted to include the energy dissipative plasticity processes in the γ term to better describe the behaviour of ductile metals. This results in significantly larger γ values for ductile materials, but also suggests that the critical stress should have same sensitivity to the flaw size, c . This is not found to be the case, with there being little sensitivity to the flaw size in ductile materials [139].

The introduction of the stress intensity factor, K_f , allowed for a more robust treatment of stresses at the crack tip for the prediction of fracture. From Equation 3.12, for crack propagation, we have

$$\sigma_f \sqrt{c} \geq \text{critical value} \quad (3.17)$$

where the critical value is material dependent. Irwin extended this relation to give the following

$$K_f = \sigma_f \sqrt{\pi c} \quad \text{and} \quad K_c = \sigma_* \sqrt{\pi c} \quad (3.18)$$

such that, when K reaches a critical value, K_c , crack propagation initiates [140]. From Equations 3.16 and 3.18, we have

$$K_f = \sqrt{EG} \quad \text{and} \quad K_c = \sqrt{EG_c} \quad (3.19)$$

That the energy and stress approaches are relatable in this way is reassuring, in fact, G and K_f are largely equivalent [141].

The critical fracture toughness (K_c) describes how well a material resists crack propagation. It characterises the stress state near the tip of a sharp crack. There is therefore significance in the loading geometry and resulting stress state in which a crack propagates. Irwin considered three propagation modes, Figure 3.7 [139]. These may act individually or in some sort of combination. The additive nature of K_f allows the contributions of the different modes to be discerned in a way that becomes complicated when considering G . Mode I, the opening mode a crack experiences when a tensile force is applied perpendicular to the plane of the crack, is assumed in the analysis above. Strictly, G_c and K_c in Equations 3.16 and 3.18 should therefore be referred to as G_{Ic} and K_{Ic} . In general, mode I has the lowest associated K_{Ic} and G_{Ic} values. Subsequently, if the geometry allows it, it is usually assumed that mode I fracture dominates. Modes II and III are driven by shear stresses [142].

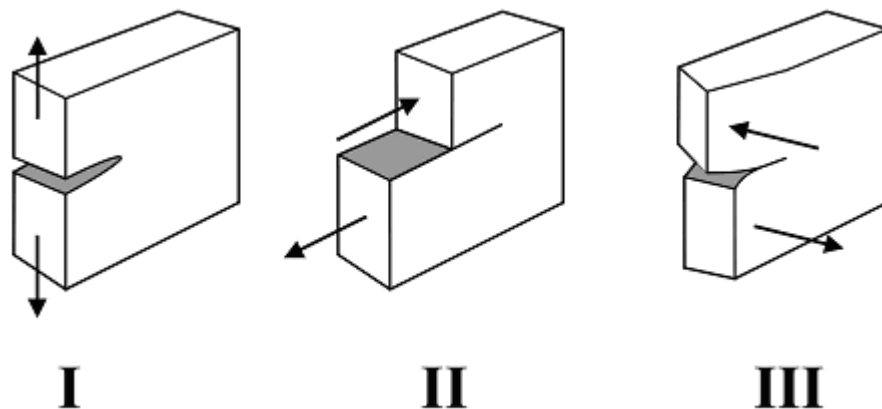


Figure 3.7 Fracture modes by which crack propagation occurs - from https://www.doitpoms.ac.uk/tlplib/brittle_fracture/same.php

This early work provided the basis for linear elastic fracture mechanics (LEFM). It accounted well for the behaviour of brittle materials, where non-linear behaviour is limited to small regions at the crack tip. Popular extensions that account for greater degrees of plastic deformation are crack tip opening displacement (CTOD) and J contour integral analyses. Both give nearly size-independent measures of the fracture toughness, which correlates well with observation for fracture in ductile materials. CTOD was formulated following Wells observation that the degree of blunting scaled with the fracture toughness [143, 144]. CTOD, δ_{CTOD} , can be expressed as

$$\delta_{CTOD} = \frac{4K_I^2}{\pi\sigma_Y E} = \frac{4G}{\pi\sigma_Y} \quad (3.20)$$

The J contour integral uses a non-linear elastic approach to represent plasticity [145]. The key here is that both will increase monotonically. However, plasticity may exhibit path dependent behaviour. For cases where minimal unloading takes place, this analysis should perform well [146]. The value J represents an energy release rate, similar to G , and can be expressed as

$$J = \frac{dW}{\text{new crack area}} = \frac{K_I^2}{E'} \quad (3.21)$$

where E' describes non-linear elastic behaviour [145]. In Equation 3.14, dW includes just the effect of strain energy release rate, however here it includes the effect of work done by plasticity. As with K_f and G , the CTOD and J integral are equivalent [141, 147]. Both models break down with significant plastic deformation and crack growth [148]. Crack tip conditions transition from plane strain to plane stress as the plastic zone becomes comparable with specimen dimensions. In measuring all the material fracture parameters discussed so far, it is important that plane strain conditions are maintained [149]. The size of the plastic zone is known to scale with the applied stress, but the shape is also dependent on the loading geometry.

In order to describe dynamic fracture, further extensions are necessary. The effects of inertia forces, strain rate sensitive plasticity and stress wave phenomena all serve to complicate the picture. When the applied load changes abruptly, a portion of the work done is converted to kinetic energy, which results in oscillating stresses associated with the inertia of the system. As discussed in §3.1, plasticity of metals is strain rate dependent. The effect high strain rates will have on crack propagation will be complicated, as we can expect more energy absorption for a certain strain, but also, a smaller degree of blunting, with the material behaving harder. Stress waves reflected off specimen boundaries and crack faces interact constructively and destructively to give highly complex stress states at the crack tip. Subsequently, the stress based fracture toughness approach becomes difficult to characterise. In the case where the plastic zone at the crack tip remains small, the LEFM approach remains applicable with small

modifications. This is the basis of elastodynamic fracture mechanics [139]. In general, however, we can expect that certain metals will exhibit a significant degree of plasticity.

The crack speed becomes significant in the case of dynamic fracture. For crack propagation speeds approaching 0 m s^{-1} , the toughness corresponding to the arrest of crack propagation, K_{IA} , tends to be lower than that of the quasi-static toughness, K_{IC} , as the degree of blunting is reduced and the plastic zone is smaller. Kinetic energy terms may also be significant at high strain rates. At higher speeds, these inertia effects become greater still and act to dissipate energy, acting to raise the fracture toughness. The dynamic fracture toughness, K_{ID} , is seen to vary with crack speed [150]. When K_I falls below K_{ID} , crack propagation halts.

It is clear that a stress intensity approach for characterising dynamic fracture is non-trivial in practice. The energy-based approach, which provides a more global parameter and less focus on the stress state at the crack tip, is more attractive. In fact, the expression for J can be adapted to account for the effects of inertia forces and strain rate plasticity with relative ease [151, 152]. In Equation 3.21, dW represents the change in strain energy and the work done to propagate the crack. This can be extended further to give a complete description

$$dW = dF - dU - dE_k \quad (3.22)$$

where F is the work done by external forces, U is the strain energy per unit volume and E_k is the kinetic energy [153]. In the original derivation proposed by Griffith, it is assumed that $E_k = 0$, so this is a natural extension. Strain rate sensitive plasticity effects can be accounted for by appropriate modifications to the work done expression. The effect of stress waves is difficult to incorporate. However, this can be circumvented by considering the system at long times, when stress waves have travelled the extent of a specimen several times [139].

The J integral approach provides a procedure to calculate a strain energy release rate for dynamic fracture experiments. The global nature of J means it is not necessary to have knowledge of exactly what is happening at the crack tip [146].

3.3.1 *Embrittlement Mechanisms*

Characterising the fracture behaviour of materials has obvious benefits to industry, where failure may be costly. A useful extension of this is the monitoring of materials that experience embrittlement in service. Embrittlement stems from a loss of ductility for certain materials in certain environments. Mechanisms include the absorption of certain compounds, stress corrosion cracking and radiation damage [154-156].

Hydrogen embrittlement is a common form of embrittlement that involves the uptake of atomic hydrogen into metallic crystal structure [154]. Proposed mechanisms for this are based on dislocation nucleation and include the hydrogen embrittlement decohesion (HEDE), hydrogen embrittlement local plasticity (HELP) and more recently, the defect acting agents (Defactant) models [157]. The Defactant model has so far shown the most promise in accounting for all findings. It is based upon hydrogen reducing the formation energy of defects via atomic diffusion [157, 158].

Embrittlement via the absorption of hydrogen is a problem for many metallic materials. In aluminium, the excursion behaviour seen with steels was observed with nanoindentation [159]. The fatigue crack growth rate was found to increase with hydrogenation for a 7075 aluminium alloy [160]. In palladium, hydride phases are seen to form at H:Pd ratios from 0.03 to 0.62. Palladium samples were cycled within this miscibility gap and tested with tensile testing techniques to reveal a dependence of strength, hardness and ductility on the degree of hydrogen uptake and the number of cycles. This was put down to dislocations being introduced into the palladium matrix [161].

There are other cases of embrittlement via absorption of an element into the matrix. Oxygen in copper is an example, where oxygen rich regions form in the vicinity of the grain boundary due to segregation [162]. Cu_2O can then form to disrupt the lattice.

3.3.2 *Conventional Characterisation Methods*

Fracture characterisation tests can be used to test both materials and components, though material testing is more common. Accurate characterisation generally relies on a material being sufficiently brittle that a plastic zone of the scale of the test specimen

does not form. Such plastic zones will lead to failure by plasticity mechanisms. It is important that plane strain conditions are maintained in the characterisation of (mode I) fracture energies [139].

The most common experimental setup for characterising quasi-static fracture properties are tensile loading of a compact tension (C(T)) specimen and three point bend loading of a single edge notched bend (SE(B)) specimen, Figure 3.7. Both these require a great degree of control and are costly in material usage [139].

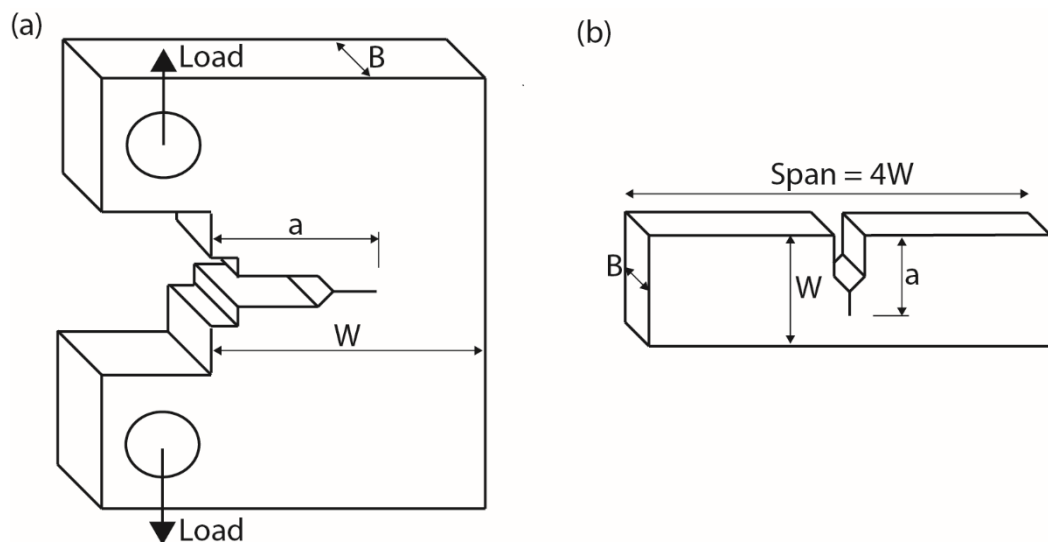


Figure 3.8 Standardised fracture mechanics test specimens: (a)C(T) specimen and (b)SE(B) specimen (as per ASTM).

The Charpy and Izod impact tests are the most common method for dynamic fracture characterisation. In both cases, a small notched bar is impacted by a pendulum, where a 3 point bend test arrangement and a cantilever arrangement, respectively, are used. The energy of the pendulum is assessed prior to and following impact to calculate a fracture energy. Again, the assumption that plane strain conditions are maintained is not necessarily applicable. This will act to give a fracture energy that is larger than the true value [139].

3.3.3 Dynamic Fracture in FEM

For the modelling of the dynamic fracture of metals, use of a high strain rate plasticity constitutive law is necessary. JC, and variants of it [163-165], are widely used.

In general, the basic form is considered to be quite reliable, provided the values of the constants in it can be obtained for the material concerned. For the fracture event, even if it is accepted that only empirical formulations are likely to be feasible, this presents a more severe challenge, since fracture is inevitably a complex process. A number of reviews [48-50] cover the issues involved in (FEM) simulation of the fracture of metal samples under impact conditions. This is particularly complex when the sample is in the form of relatively thin plate, for which there have been specific studies on petalling phenomena [166, 167], shear plugging failure [168, 169] and dishing [170].

Despite these complexities, attempts have been made to identify universal analytical expressions for the prediction of fracture under high strain rate conditions. For example, Johnson and Cook [110] proposed the following expression for the critical strain, ε_f , at which fracture will occur

$$\varepsilon_f = \left[D_1 + D_2 \exp \left(D_3 \left(\frac{\sigma_H}{\sigma_{VM}} \right) \right) \right] \left[1 + C \ln(\dot{\varepsilon}_p^*) \right] \left[1 + D_4 (T^*) \right] \quad (3.23)$$

where $D_1 - D_4$ are empirical constants. It can be seen that the dependence on strain rate is the same as the one that these authors proposed for the flow stress (Equation 3.5) and the dependence on temperature is similar. The dependence on the (local) stress state is captured in the first term with the presence of the stress triaxiality – the ratio of hydrostatic to deviatoric (von Mises) components. The formulation is plausible in a general sense, since it is common to assume that fracture occurs when a critical level of plastic strain has been reached (i.e. the ductility of the metal has been “exhausted”), and the general suitability of this is widely accepted [171-177]. Also, a high stress triaxiality often favours fracture (over plasticity) and some sensitivity to temperature and strain rate is also expected (with the sense of these dependences controlled by the signs of the empirical constants). On the other hand, the formulation has no mechanistic basis (in terms of the magnitude of the strain energy release rate for crack propagation or the fracture energy of the material). This also applies to various attempts that have been made [178] to identify a “damage development parameter”, and to correlate this with the equivalent plastic strain.

Detailed attempts to assess the reliability of predictions obtained using Equation 3.23, and other empirical relationships based on critical strain levels, have sometimes concluded that this approach yields poor agreement. For example, Sharma et al [179] found that they could not use it to capture the fracture behaviour of an Al alloy being penetrated by hard spheres, although they did claim that there was some correlation with the (tensile) hydrostatic stress level. Dey et al [180] reported rather similar findings and attempts to use other criteria, such as those of Mohr-Coulomb [181] or Bao-Wierzbicki [182], also encountered limitations.

Of course, the observations on which such comparisons are based are often relatively crude. One of the difficulties is that the kind of fracture being produced during testing has in many cases [183, 184] been a “plug” shear failure, in which large amounts of plastic deformation have been produced in the vicinity of the projectile. The final fracture event is often not one of well-defined crack propagation, but simply that of pushing the plug out of the rear face of the sample. In cases such as this, very large plastic strains may be created under conditions such that fracture cannot occur. In fact, a similar effect can in some cases be produced during a conventional (quasi-static) tensile test – with a highly ductile material, the failure event may involve necking almost down to a point, with the fracture characteristics per se of the material playing little or no role [185].

There have been at least some fracture mechanics-based investigations of sample failure during impact loading. For example, Xu and Li [186] examined the conditions created during Hopkinson bar testing, using FEM and evaluating the “Dynamic Fracture Toughness” as a function of the crack tip conditions created with different operational parameters (such as striker impact velocity). However, their main conclusion was that this is a very complex area, and that it’s not even clear whether an increase in the imposed strain rate should raise or lower the fracture toughness (or fracture energy). This is in fact plausible, since, while a higher strain rate might be expected to inhibit plastic flow at the crack tip, reducing the toughness, the associated increase in temperature could promote such plasticity, having the opposite effect.

There have also been energy-based (if not fracture mechanics-based) analyses of projectile perforation through thin sheets, one of which [187] highlighted the potential

significance of the kinetic energy of ejected fragments. There have also been many studies [188] confirming that the fracture toughness of a material tends to be substantially reduced by high levels of prior plastic strain. Of course, this is well established in a general sense, but such measurements don't really provide useful information about how fracture is likely to occur in situ during an impact event, which is in most cases a highly dynamic process.

Nevertheless, it should in principle be possible to use an impact test to obtain a value of the fracture energy from observations of the crack patterns induced under different impact conditions and use of FEM to estimate the strain energy release rate at the point where crack propagation was initiated.

Chapter 4

Indentation Testing

Instrumented indentation is the controlled and monitored penetration of a hard body (the tip) into a sample. In the case of quasi-static indentation and indentation creep methods, load and displacement can be monitored as a function of time with high accuracy. Load-displacement-time data from such tests contain information about the elastic, plastic and creep (time-dependent) response of the material. Extracting this information reliably and robustly presents challenges. A number of approaches have been developed by researchers, over a range (nm-mm) of scales, with varying degrees of success. In this chapter, the attractions and issues associated with indentation are discussed. Well-accepted procedures and recent developments for material characterisation from indentation data are introduced and appraised.

4.1 Indentation Material Characterisation

Development of indentation methods for the characterisation of materials is an active research area. A key attraction of indentation lies in the ease of experimental implementation, with sample preparation usually consisting simply of producing a flat surface. There is scope for examining and mapping local properties over a surface – for example across a weld section [189] – although the interrogated volume must be large enough to give a representative response, which usually means that it must contain at least several grains. Other benefits include: small quantities of material can be tested, testing can be done in-situ on real in service components, it can be effectively non-destructive and there is the potential to test coatings.

The main issue with these techniques lies in the evaluation of mechanical property parameters. In contrast to conventional uniaxial testing methods, stress and strain fields are not uniform (and also change as indenter penetration occurs) [118, 190, 191].

Obtaining a stress-strain curve (or other information, such as a creep strain-time curve) from indentation data is therefore far from simple. Analytical approaches generally fail to account for this complexity, limiting their accuracy. Despite this, a series of analytical approaches have been proposed. The Inverse FEM method, on the other hand, is a transparent and tractable approach. FEM inherently has the capability of accounting for spatially and temporally complex stress and strain fields (provided suitable constitutive laws are available). The inverse procedure involves initially using a trial set of property parameter values, running the FEM model, comparing the outcome (e.g. load-displacement plot) with the experimental one and then iteratively changing the input property parameter values until optimum agreement is reached. This is a simple concept, but challenging in terms of ensuring that the inferred property parameter values are reliable and accurate [116, 117, 119-124, 191].

4.1.1 Hardness

In general, hardness is a poorly-defined material “property” that provides a semi-quantitative measure of the resistance to plastic deformation. It is not a fundamental property, since its value depends on the test geometry (indenter shape) and applied load, as well as on yielding and work-hardening characteristics. Also, and rather more fundamentally, a whole range of combinations of these characteristics can lead to the same hardness number. Qualitatively ranking material hardness dates back to 1882, with the establishment of the Mohs mineral hardness scale [192]. The advent of the hardness tester allowed a slightly more quantitative measure of the hardness, often termed the ‘indentation hardness’. The indentation hardness is defined as [1]

$$H = \frac{P_{max}}{A_c} \quad (4.1)$$

where P_{max} is the maximum load reached during indentation and A_c the contact area at this point. This area is calculated from the known tip geometry and the residual indent extent, which is often assessed (in lateral directions) optically after the specimen is unloaded. Elastic recovery on unloading is assumed to be negligible, as are sink-in and pile-up effects [193, 194].

Important developments started in the 1970s when the longstanding hardness test was developed into “instrumented” (displacement-sensing) indentation [195]. It has often been termed “nanoindentation”, although the most important point is not so much the very fine scale over which the measurements are made, but the continuous monitoring of both load and displacement to a high precision. With knowledge of the penetration displacement and the tip area function, A_c can be obtained for the calculation of the hardness. For the purposes of this study, where the scale of indentation is large (of the order of mm), many of the details of nanoindentation are not of central importance.

4.1.2 *Plasticity*

The complexity and variety in material stress-strain relationships makes inverse FEM methods an attractive method for characterisation via indentation data. Prior to the application of inverse FEM methods, proposed procedures and the corresponding analytical expressions were generally unsatisfactory or only applicable to particular materials [191].

Although there were previous attempts [196], Campbell et al. [191] demonstrated an inverse FEM procedure successfully for the characterisation plasticity behaviour from indentation data, highlighting many of the issues involved in such a procedure and fully characterising a number of metallic materials through comparisons with load-displacement data. Benefits were identified in the sensitivity of the method to the plasticity behaviour when performing shallow indents (15% of the radius) and considering the residual indent profile outcome [3]. Figure 4.1 shows the agreement between uniaxial tests and indentation tests in conjunction with the inverse FEM procedure for an annealed copper, as-received copper and aluminium. The study highlighted the significance of anisotropy and how the indentation response could be expected to be a combination of the plasticity response from axially and radially oriented samples from an extruded rod, tested uniaxially. Indentation is inherently a test that samples some kind of direction-averaged property, so this is unsurprising.

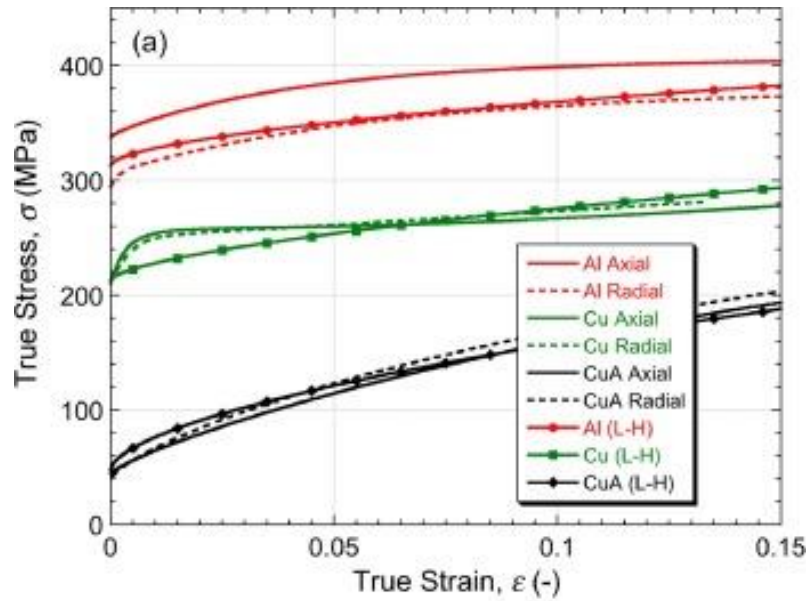


Figure 4.1 Results showing indentation inferred parameters (solid line) and axially and radially oriented specimen parameters tested uniaxially [3].

4.1.3 Indentation Creep

Many of the attractive aspects associated with indentation tests also apply to indentation creep. Compared with conventional methods, the size and shape requirements are far less demanding, the small scale of indents mean properties can be mapped over a surface and tests can be almost non-destructive. The ability to create a range of (deviatoric) stress levels in a single test is also beneficial [191].

As with most conventional testing methods, indentation creep methods take place at constant load or constant displacement. Constant load tests are, again, more common. The displacement-time outcome for a typical creep indent is shown in Figure 4.2. Although similar in form to that of a conventional creep test, the relation between the load and the displacement and stress and strain is far more complicated, and realistically, an analytical approach is always going to be limited.

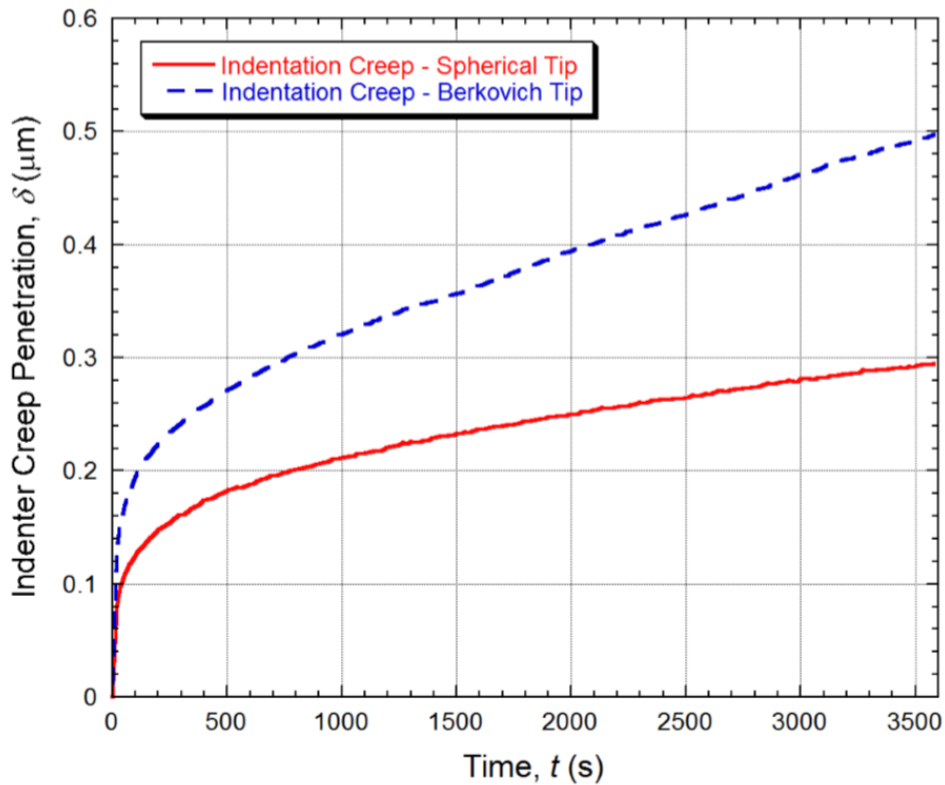


Figure 4.2 Typical indentation creep curves from both a spherical tip and Berkovich tip. Time-dependent creep occurs during a constant load dwell [197].

An important point when considering indentation creep is the possibility of conventional (time-independent) plasticity and the effect this may have on the material. In all current indentation creep procedures, indentation is carried out on a flat surface. In order to penetrate to a suitable depth, such that a creep response of a metallic material is detectable, the stresses will be very high initially, so a degree of plasticity must occur. This can act to change the microstructure of the material and effect subsequent creep behaviour. The effect of plasticity can introduce considerable errors in indentation creep analysis. However, this is often neglected [198].

4.1.3.1 *Stable Indenter Velocity Method*

The ‘stable indenter velocity’ method is a popular analytical approach for analysis of indentation creep data to extract the creep stress exponent. It relies on a series of major assumptions [199, 200]:

- a) A representative and uniform stress exists in the material for a given load and contact area, defined by

$$\sigma_r = \frac{P_{\max}}{A_p} \quad (4.2)$$

where A_p is the projected area.

- b) A representative and uniform strain rate exists in the material, defined by [201]

$$\dot{\epsilon}_r = \frac{1}{\delta} \cdot \frac{d\delta}{dt} \quad (4.3)$$

- c) All deformation that occurs in the hold period can be attributed to secondary (steady state) creep.

From these assumptions and Equation 2.13 (which describes the creep rate in the steady state creep regime) we have

$$\frac{1}{\delta} \cdot \frac{d\delta}{dt} = C_3 \left(\frac{P_{\max}}{A_p} \right)^{n_2} \exp\left(\frac{-Q}{R_{\text{gas}} T} \right) \quad \& \quad \ln\left(\frac{1}{\delta} \cdot \frac{d\delta}{dt} \right) = \ln(C_3) + n_2 \ln\left(\frac{P_{\max}}{A_p} \right) - \left(\frac{Q}{R_{\text{gas}} T} \right) \quad (4.4)$$

From this, both the stress exponent and activation energy can be calculated by plotting $\ln(\dot{\epsilon}_r)$ against $\ln(\sigma_r)$ and $1/T$, respectively.

There are examples of activation energies extracted from indentation creep data that compare well with measured values from literature [202-205], although in many cases, no attempt was made to measure an activation energy with conventional methods for the particular test material.

Values of the stress exponent obtained in this way have in general proved to be very unreliable, casting doubt on the assumptions made [199, 206, 207]. Values of $n_2 > 20$ have been reported [208] and the tip shape has been found to have a dramatic effect on the extracted value [209]. Again, there have in many cases been no attempt to compare these values with conventionally measured values or those from literature. Dean et al. [190] measured the stress exponent for tin and copper samples via both indentation and

conventional methods. The agreement was found to be very poor and indentation-derived values varied with indenter shape, maximum applied load, loading rate and loading time.

Many authors have shown using FEM that the stress and strain rate fields beneath an indenter tip are in fact far from uniform [190, 199, 210]. Ignoring the effects of primary creep regime behaviour also leads to major discrepancies [190, 199, 211]. This applies irrespective of testing time, since the creep strain field is continually expanding, and hence there is always material in the early (primary) part of the creep strain history. This methodology can now be regarded as completely discredited.

4.1.4 *Ballistic (Dynamic) Indentation Methods*

In dynamic indentation, higher loading rates can prompt a response similar to that of quasi-static instrumented indentation, but with greater significance given to high strain rate parameters, with very high strain rates (up to $\sim 10^6 \text{ s}^{-1}$) generated [107]. Many of the attractions that apply to instrumented indentation also apply to ballistic indentation. However, it is often more difficult to monitor than (quasi-static) instrumented indentation. At the relevant strain rates (10^2 s^{-1} to 10^6 s^{-1}), deformation can be complete within a few microseconds. High-speed cameras and strain gauges can be used to monitor deformation in situ and residual profiles provide another useful experimental output.

Due to such difficulties, there has been relatively little work in the area of property parameter extraction from dynamic indentation data. Unsurprisingly, the technique has lent itself well to the assessment of materials for in-service parts likely to suffer impact, particularly in the study and development of armour [212, 213].

Ballistic instrumented indentation experiments have been carried-out to give good correlation between values obtained from experiment and those obtained through FEM simulation [214]. A moiré interferometry-based displacement measurement technique was used to measure the indentation depth and a quartz load transducer was used to measure the load. This is such that the indentation depth-time, load-time and load-depth histories can be found at all times. Effective strain rates can be expressed as

$$\dot{\varepsilon}_{\text{eff}} = \frac{\varepsilon_{\text{eff}}}{t_0} \quad (4.5)$$

where t_0 is the duration of loading and ε_{eff} is a representative effective strain that has been demonstrated to exist beneath a sharp indenter tip [215]. Again, this “effective” strain rate is potentially misleading. These were then plotted against normalised flow stress values for various impact velocities to gauge the strain rate sensitivity. Simulations were carried out based on the constitutive relation

$$\sigma_{\text{flow}} = (\sigma_Y + K\varepsilon) \left[1 + \left(\frac{\dot{\varepsilon}}{\dot{\varepsilon}_0} \right)^C \right] \quad (4.6)$$

where σ_Y is a reference yield stress, $\dot{\varepsilon}_0$ is a reference strain rate and C is a strain rate sensitivity parameter. Adjustment of C was carried out to fit the simulated data to the experimental data (depth-time, load-time and load-depth histories) and flow stresses normalised with quasi-static values were calculated to compare with the experimental values. This comparison can be seen in Figure 4.3 [214]. Although this was only used for strain rates up to 2500 s^{-1} and included monitoring of the load, it suggests an inverse FEM methodology is potentially sound and could be used for extracting rate sensitivity parameters.

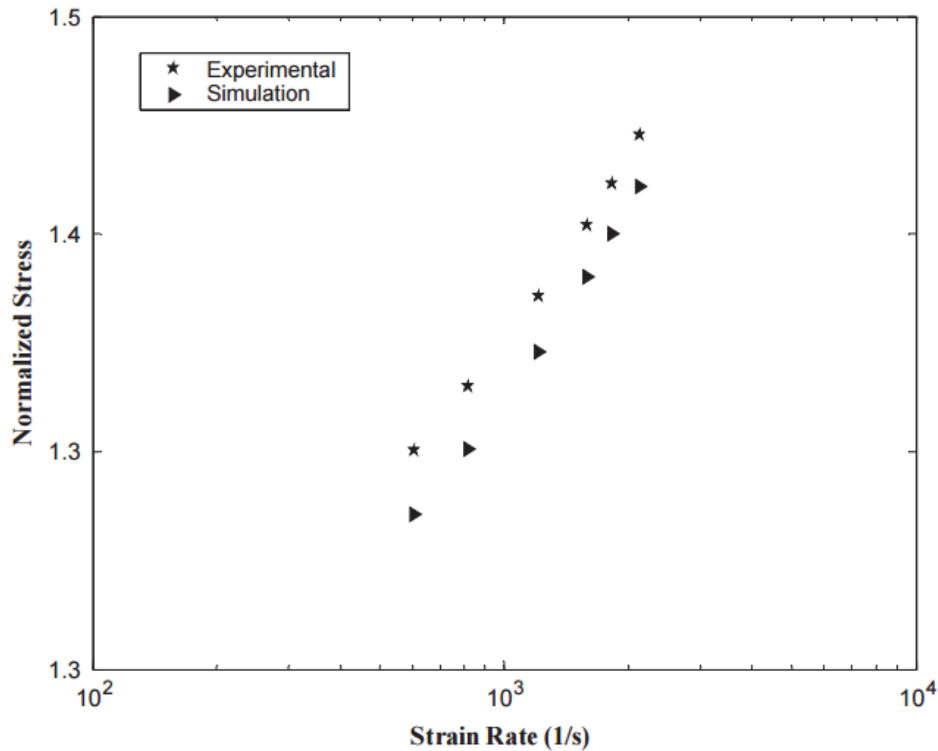


Figure 4.3 Normalised flow stress as a function of strain rate for OFHC copper from simulated and experimental data for dynamic indentation experiments [214].

4.1.5 Indentation Methods for the study of Fracture

Methods looking at crack propagation from the corners of indents carried out by nanoindentation have been developed for the estimating K_{Ic} [216]. The indentation microfracture (IM) method uses crack morphology and the extent of these cracks to do this with models such as those provided by Anstis [217] and Laugier [218]. Assumptions in these models rely on the formation of Palmqvist and halfpenny cracks. Such morphologies are seen at the corners of cube corner tips, though lateral cracks in certain materials were difficult to avoid and introduced problems regarding the assumptions of the models [219].

What is ideally required is application of the principles of fracture mechanics (i.e. the energetics associated with fracture events) to experimental situations that create high strain rates (often with high local strain levels), and also well-defined fracture events. An energy-based approach is usually the most fruitful one for fracture, since crack advance must be energetically favourable. However, the energy absorbed (during

fracture of a given material) depends on the geometry, which determines the crack propagation mode mix [158, 159, 161] and whether the stress field ahead of the crack tip corresponds to plane stress or plane strain (or intermediate) conditions. The fracture energy tends to be quite sensitive to these variations. This is further complicated for ballistic impact by the fact that the stress field varies rapidly with position and time throughout the process. There has in fact been quite longstanding interest in trying to obtain fracture characteristics from crack patterns around (static) indents, but various severe challenges have been recognized [220-223]. Also, if the interest is in metals, then it is in most cases very difficult to induce cracking at quasi-static loading rates, particularly using spherical indenters (and “sharp” indenters introduce uncertainties into both the experiments and the modelling of them).

4.1.6 *Indentation of Coatings*

The extension of indentation techniques to coated systems is of interest, since it is one of the few methods for measuring their mechanical properties. Following the success with bulk systems, methodologies employing nanoindentation and inverse FEM to characterise plasticity have been extended to coated systems [224-227]. Initial work was done to assess the viability of these methods for relatively thick coatings [224, 227]. Figure 4.4 shows comparisons between model and experiments from Reed et al. [224]. The method requires knowledge of substrate properties. The coating was not bonded in any way to the substrate, which was consistent with the modelling. The iterative process was then carried out for the coating material. Campbell et al. [226] used the approach to characterise the plasticity of plasma sprayed turbine blade coatings. In order to avoid complications from the effect of the substrate and interface, indent depths were limited to 10% of the coating thickness. Due to geometrical arrangement of coated systems, it is clear that inverse FEM procedures have significant potential for coatings (as well as for bulk samples).

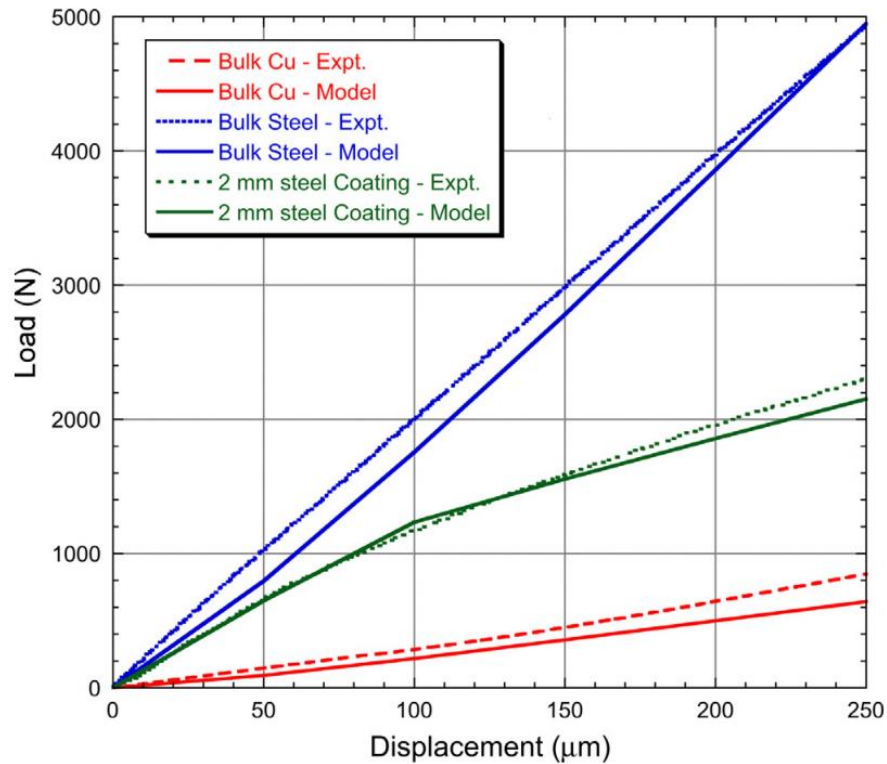


Figure 4.4 Measured and predicted load-displacement data for indentation of bulk copper, bulk steel and a 2mm thick copper on steel with a 3mm diamond WC sphere [224].

4.2 Factors Influencing Indentation Outcomes

There are a number of issues concerning the reliability of indentation data, some of which can become more significant as the scale of the indentation is reduced. In this study, the scale of indentation is large (\sim mm). The main issues with indentation (both creep and ballistic) at this scale are discussed.

4.2.1.1 *Thermal Drift*

Thermal drift can arise from contractions and expansions of the sample and indenter tip as they change temperature (equilibrate) during loading/unloading. The resulting measured displacements can be confused with those due to creep, although there are precautions and correction procedures that can help rectify this [228]. It is often more significant at relatively high temperatures, with the need to equilibrate tip and sample temperatures prior to indentation becoming more challenging [229, 230].

4.2.1.2 *Friction*

Friction experienced between the indenter tip and the sample surface has been found to affect the strain field beneath the indenter with FEM simulations [231]. Effects were also reported on the contact area, A_c , as a function of indent depth, and on the degree of pile-up [191, 232]. It was concluded that the inclusion of friction in inverse FEM of indentation data is needed.

4.2.1.3 *Interrogated Volume*

When indenting a single crystal, the crystallographic orientation will tend to influence the response [233], particularly the plastic deformation. Of course, this is expected from Schmid factor variations. It follows that, in a polycrystalline sample, indentation such that most indents lie within single grains will lead to a wide scatter in results and these indentation responses will not represent (even as averages) the bulk response [118]. For a bulk response, many grains must be sampled by the indenter tip during each indent (the grain boundary response, as well as the texture, is likely to affect the bulk response). There are, however, examples where single grain response is preferential. For example, nanoindentation has been used to study the effect of individual dislocations and their emission to support the hydrogen-enhanced localised plasticity model for hydrogen embrittlement. This requires dislocation free volumes, which is readily achievable with nanoindentation, since it probes small volumes [234].

4.2.1.4 *Tip Geometry*

It is not surprising that different tip shapes and sizes probe different portions of the relevant response characteristics, since the associated stress and strain fields can be vastly different [196]. This limits the use of analytically-based expressions that are not tip geometry specific and is another benefit of FEM modelling for analysing indentation data. For a ballistic event, tumbling of projectiles may be a problem. Controlling projectiles fired from a gas gun such that they impact with a particular orientation is difficult. The effect of tumbling projectiles, and measures to control it has been studied [235], though the use of spherical projectiles can largely solve these issues.

Chapter 5

Experimental Techniques

5.1 Experimental Procedures

5.1.1 *Specimen Production*

Four metallic materials were used in this study. These were obtained from commercial sources. A 9.5 mm diameter extruded nickel rod of 99 % purity was used for the study of creep. A 25 mm diameter extruded OFHC copper bar was used both in the as-received state and after an annealing treatment. This annealed copper material was produced by machining the as-received copper to 16 mm diameter and annealing it for two hours at 800 °C in a sealed ampoule (backfilled with argon). This treatment caused recrystallization and hence a substantial drop in the hardness of the material. Both the as-received and annealed copper materials were the subject of the strain rate sensitivity study. A cast (commercial purity) magnesium ingot with dimensions of about 150 mm by 75 mm in transverse section and originally about 300 mm long was used for the study of (impact) fracture.

5.1.2 *Sample Preparation*

Uniaxial tensile and uniaxial compression samples from the extruded nickel rod material were produced by lathe. For both uniaxial tensile plasticity and creep testing, samples were in the form of cylindrical dog-bone samples, with a gauge section diameter of 3.1 mm and a length of 22 mm. Cylindrical compression specimens with the (as-received) 9.5 mm diameter and 10 mm height were machined. Indentation samples were machined in the same way as the compression samples prior to the creation of the recess, §5.1.2.1.

Uniaxial compression samples from the as-received copper and annealed copper were produced by electrical discharge machining (EDM). Cylindrical compression specimens of 6 mm height and 5 mm diameter were produced in the on-axis (extruded) and radial directions. Ballistic samples were obtained for the as-received copper rods by machining into cylinders of diameter 25 mm and height 30 mm. For the production of annealed ballistic samples, as-received extruded rod material was machined into cylinders of 16 mm and 20 mm height prior to annealing.

All uniaxial compression and ballistic samples from the cast magnesium material were produced by EDM. Uniaxial compression samples of 10 mm height and 10 mm diameter and ballistic samples of 20 mm height and 16 mm diameter were machined.

All indentation surfaces were prepared to a 1 µm diamond polish finish. The grain structures of all materials used in this study were examined with application of the etchants used are summarised in Table 5.1 following preparation with 1 µm diamond impregnated paste.

Material	Etchant
Nickel	Oxide polishing suspension (OPS)
Copper (as-received and annealed)	960 ml methylated spirit, 20 ml HCl, 50 g ferric chloride.
Magnesium	Nital

Table 5.1 Summary of etchants used for each material.

5.1.2.1 *Indentation Creep Recess Preparation*

The recess, with a depth of 1.0 mm, was produced by first using a spherical end drill of diameter 4 mm to remove the bulk of the recess material. This was honed using an identical sphere to that used in the creep testing (4 mm diameter Si₃N₄), attached to the end of a drill bit. SiC polishing paste (~1 µm) was inserted into the recess before this honing operation. This ensured that the shape of the recess closely matched that of the

indenter, which was checked using a profilometer, as described in §5.1.9. The depth was measured by taking the difference between the height of the sample with a ball placed in the recess and the sum of the sample height alone and known ball diameter. The honing process was found to result in an increase in the indent depth of $\sim 40\ \mu\text{m}$ – this was, in part, to ensure minimal effect from work hardened material in the vicinity of the drilled machining.

5.1.3 *Indentation Creep*

The indenter used was a sphere of 4 mm diameter, made of Si_3N_4 (supplier Bearing Warehouse Ltd). Creep tests were carried out over a period of $5 \times 10^4\ \text{s}$ (~ 14 hours). Constant load was applied through the duration of the test. Loads of 0.85 and 1.0 kN were used, with loading rates chosen so as to avoid creep effects during this operation (max load reached after $\sim 2\ \text{s}$). FEM simulation was used to ensure that, with this configuration, and with these loads, the peak (von Mises) stress created under the indenter was below the uniaxial yield stress (at the temperature concerned). Indentation creep curves at 750°C were obtained using an Instron LCF testing machine. Displacement measurements were taken from the crosshead. Great care was taken to make sure the system had thermally equilibrated, such that thermal expansion and contraction of the loading column did not affect the measured displacement. The samples were cylinders of diameter 9.5 mm and thickness 10 mm.

A potentially important issue, particularly when testing highly creep-resistant materials, concerns the possibility of inelastic deformation occurring within the housing of the indentation sphere during the test. This housing is most conveniently made of metal, but this leads to the possibility of creep occurring within it close to the indenter, in a similar way to that occurring in the sample. This would introduce errors in the measured displacement-time data. This was eliminated in the current work by using two identical samples, both with recesses, located above and below a free-standing (ceramic) sphere. Not only does this eliminate the possibility of errors arising from an unknown contribution to the displacement from deformation within the housing, but also the magnitude of the measured displacement is doubled, thus improving the accuracy of the data. This setup is depicted in Figure 5.1.

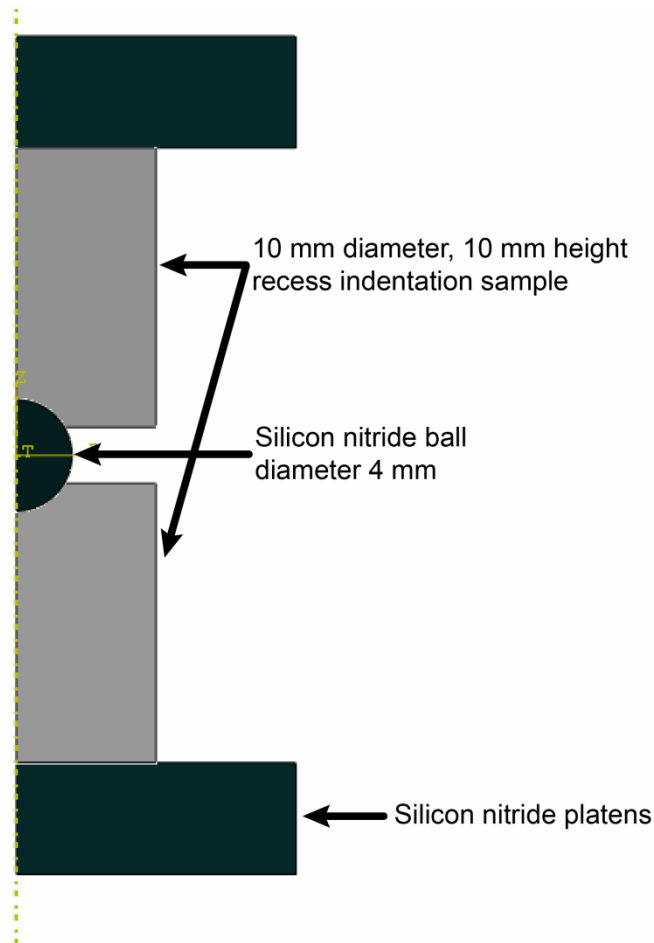


Figure 5.1 Axisymmetric schematic depiction of the Indentation creep setup.

5.1.4 Uniaxial Tensile Testing

Tensile samples were gripped using collets made of CMSX-4. Strain was measured using an MTS 632.54F-14 axial extensometer (clip gauge), with a gauge length of 12 mm. Tensile stress-strain curves at 750°C were obtained using an Instron LCF testing machine. Several repeat tests were carried out. Both stress and strain levels were converted from nominal to true values, using the standard expressions given in Equation 2.3.

5.1.5 Uniaxial Tensile Creep Testing

Uniaxial tensile creep testing was carried out using the same machine, sample dimensions and set-up as for the stress-strain testing (§5.1.4). Stress levels were chosen to ensure that they were below the measured yield stress, so that conventional plasticity

did not occur, with loading rates chosen so as to avoid creep effects during this operation (max load reached after ~ 2 s). The target duration for these tests was $5 \cdot 10^4$ s (~ 14 hours).

5.1.6 *Uniaxial Compression Testing*

Uniaxial compression testing was carried out between rigid (hardened steel) platens. Specimens were tested at room temperature ($22 \text{ }^\circ\text{C} \pm 2 \text{ }^\circ\text{C}$), using MoS_2 lubricant to minimise barrelling. Displacements were measured using an eddy current gauge, with a resolution of about $1 \text{ }\mu\text{m}$. Testing was carried out under displacement control (at a rate of 2 mm min^{-1}), using an Instron 5562 screw-driven testing machine, with a load cell having a capacity of 30 kN. The strain rate generated during these tests, which was taken to be the reference (quasi-static) rate for use in Equations 6.2 and 6.3, was thus about $5.5 \cdot 10^{-3} \text{ s}^{-1}$. Tests were done up to displacements of about 1.5 mm (25% nominal plastic strain), so that each test took about 45 s to complete. It was confirmed that barrelling was negligible over this strain range.

Tests were carried out over a range of temperature, up to $300 \text{ }^\circ\text{C}$. It was confirmed by FEM modelling - see §8.3.1 – that temperatures reached during ballistic impact were lower than this, except possibly for very short transients in a thin surface layer.

Several repeat tests were carried out. Again, both stress and strain levels were converted from nominal to true values, using the standard expressions given in Equation 2.3, with the strains in this case being negative (compressive), so that the true stress has a magnitude lower than the nominal value, while the true strain has a larger magnitude than the nominal strain.

5.1.6.1 *Swaging*

For the purposes of this study, it's important to be able to simulate the stress-strain curve over a wide range of strain (perhaps up to 200% or more, depending on the depth of projectile penetration). This is well beyond the levels to which conventional uniaxial testing can be carried out (since necking/failure tends to occur in tension and barrelling in compression). This is not such a problem for the as-received (work-hardened) material, since the rate of further work hardening is low and the flow stress will tend to remain approximately constant up to large strains. For the annealed material, however,

the initial work hardening rate is high and extrapolating this behaviour to strains beyond the measurable regime (typically only up to about 20-25%) is subject to considerable error. This problem was tackled by applying three swaging operations to the annealed material, each inducing a well-defined level of (true) plastic strain, extending up to about 200%. These materials were tested in compression and the yield stress taken as a flow stress level for the annealed material at the strain concerned. This allowed the stress-strain curve to be simulated (as a set of data pairs) over the complete strain range of interest.

5.1.7 *Ballistic Impact (Gas Gun)*

The set-up employed is depicted in Figure 5.2. The gas gun used is based on three coaxial components - a 2 m barrel and two high-pressure chambers. The barrel is separated from one high-pressure chamber by a thin copper membrane (several tens of microns in thickness), with a similar membrane between it and a second chamber. Both chambers are filled with nitrogen, with pressure drops between the barrel and the first pressure chamber, and between the two pressure chambers, both set to values (just) insufficient to burst the membranes. The first chamber is then evacuated, creating pressure differences across both membranes that are sufficient to cause bursting. The expanding gas then drives the projectile, held inside an high density polyethylene sabot, along the barrel of the gun. At the end of the barrel the sabot is stripped from the projectile by a "sabot stripper", so that only the projectile (a 5 mm diameter WC-Co cermet ball) strikes the sample. The impact velocity is controlled, at least approximately, via manipulation of the thickness of the membranes and the pressure in the chambers. All impacts were at normal incidence, with samples rigidly supported at the rear, employing impact speeds in the range 50–300 m s⁻¹.

It was found to be important to secure the sample rigidly on its rear surface. The modelling covered everything happening within the sample, but one of the boundary conditions was that it was supported on an immovable surface and it was important to ensure that this condition was closely approached in practice. A massive, rigidly-held steel plate was used to provide this support.

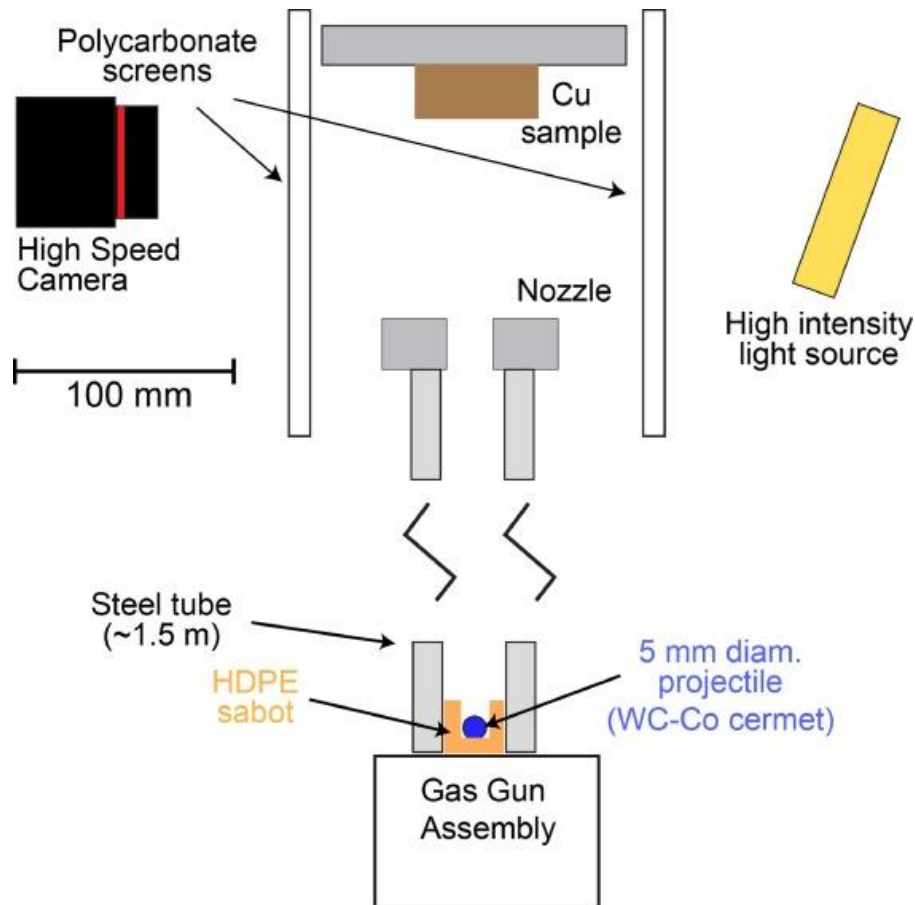


Figure 5.2 Schematic depiction of the gas gun set-up for ballistic indentation.

5.1.8 High speed photography

A Phantom VI2.1 high-speed camera was used to record impact events, with a time resolution of $\sim 1.4 \mu\text{s}$ (frame rate of $717,948 \text{ s}^{-1}$) and exposure time of $0.285 \mu\text{s}$. There was thus a dead-time between exposures of about $1.1 \mu\text{s}$. This was done deliberately, in order to obtain a combination of minimal blurring of individual images and data capture over a relatively long period, within the memory limit of the camera. Linear spatial resolution of $\sim 50 \mu\text{m}$ per pixel was achieved and images comprised 128×24 pixels. From video sequences and known calibration factors, time-displacement histories were then extracted for the projectile motion, with attention being focussed on the location of the rear of the projectile.

5.1.9 Residual indent topography

A Taylor Hobson (Talysurf) profilometer (i.e. a contacting stylus), with a wide-range inductive gauge and $20 \mu\text{m}$ radius cone recess tip, was used to measure residual indent

profiles. Scans were carried out in two perpendicular directions, both through the central axis of the indent (found by carrying out several closely-spaced parallel scans). The height resolution of these scans is about 25 μm . Tilt correction functions were applied to the raw data, based on the far-field parts of the scan being parallel. The average profile from the two orthogonal scans was taken.

5.1.10 X-ray Computed Tomography

A Bruker Skyscan 1272 x-ray was used in conjunction with the Simpleware Scanip software to reconstruct subsurface crack structure. The source voltage and source current used were 100 kV and 100 μA , respectively. An Al 1 mm filter, exposure time of 1500 ms and rotation step of 0.15 degrees were used. The resultant resolution was 9 μm per pixel. Ballistic samples were scanned in their entirety.

Chapter 6

Computational Methods

6.1 Computational Issues

6.1.1 *FEM Formulation for the (Recess) Indentation Creep*

An axi-symmetric FEM model for simulation of (spherical) creep indentation, with prior production of a recess, was built within the ABAQUS package. Both indenter (Si_3N_4) and sample (nickel) were modelled as deformable bodies and meshed with second order triangular elements. The volume elements in the model were CAX6M types (axisymmetric stress), with about 8000 elements in the sample and about 4000 in the projectile. This is shown in Figure 6.1. Meshes were refined in regions of the sample close to the indenter. Sensitivity analyses confirmed that the meshes employed were sufficiently fine to achieve convergence, numerical stability and mesh-independent results. The complete sample was included in the simulation. Creep behaviour was captured with the MN constitutive relation.

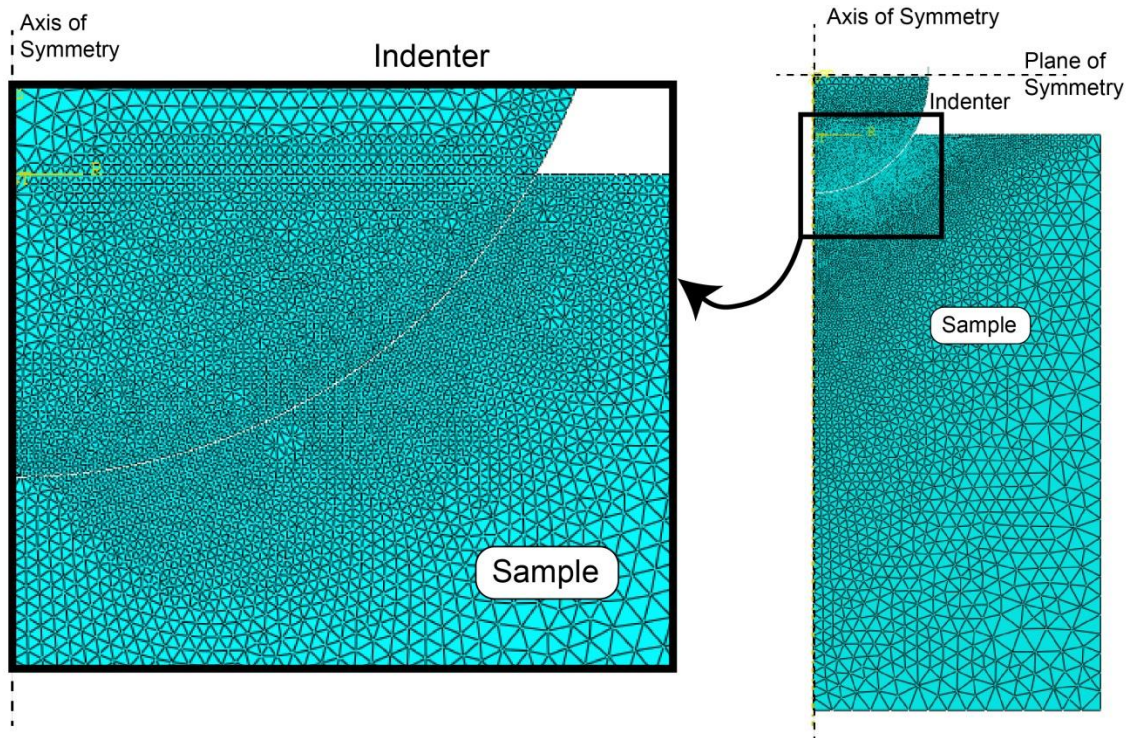


Figure 6.1 Initial FEM Mesh for simulation of indentation, using a recess and a double sample.

6.1.2 FEM Formulation for Ballistic Indentation (No Fracture)

An axi-symmetric FEM model for simulation of impact and rebound was built within the ABAQUS package. Both projectile and target were modelled as deformable bodies and meshed with first order quadrilateral elements. The projectile is expected to remain elastic throughout, although it can be important in high precision work of this nature not to treat it as a rigid body: not only is it possible for its elastic deformation to make a significant contribution to the overall displacement, but its lateral Poisson expansion could affect the outcome, particularly if attention is being focused on the shape of the residual impression. Such modelling also allows a check to be made on whether there is any danger of the projectile being plastically deformed.

The volume elements in the model were CAX4RT types (linear coupled temperature-displacement), with about 5000 elements in the sample and about 2000 in the projectile. Meshes were refined in regions of the sample close to the indenter. Sensitivity analyses confirmed that the meshes employed were sufficiently fine to achieve convergence, numerical stability and mesh-independent results. The complete sample

was included in the simulation, with its rear surface rigidly fixed in place. In modelling the complete sample, contributions to the displacement caused by its elastic deformation (as well as plastic deformation) are fully captured. A typical set of meshes is shown in Figure 6.2. Heat transfer from sample to projectile was neglected, however, the generation and transfer of heat was modelled within the sample. The strain rate sensitive plasticity behaviour of the target material was simulated with the JC constitutive relation (in some cases, the first term describing the quasi-static plasticity response was represented with data pairs).

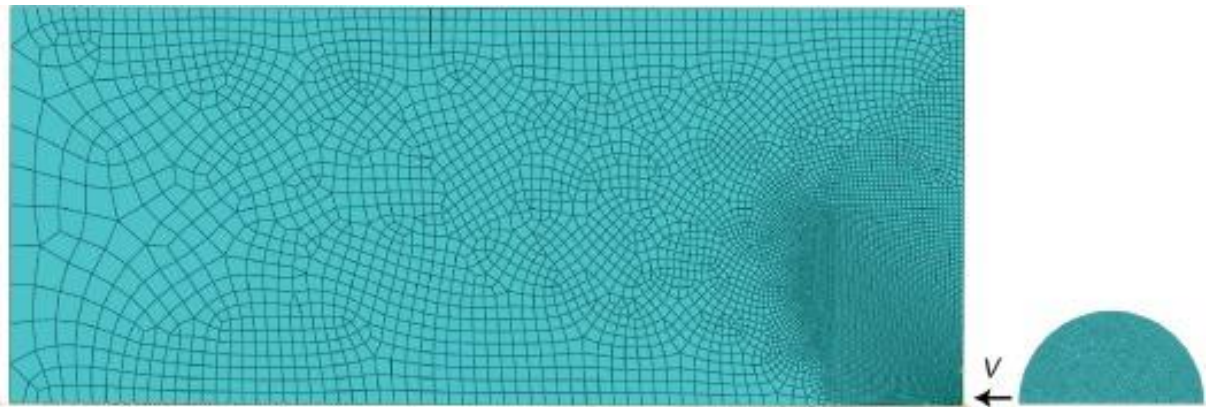


Figure 6.2 Typical mesh configurations for the FEM modelling of ballistic impact.

6.1.3 FEM Modelling of Crack Propagation

In order to simulate the crack propagation event, a 3-D (cylindrical polar) model was used. A mirror boundary condition enabled modelling of half of the experimental geometry. Both projectile and target were modelled as deformable bodies and meshed with first order tetrahedron elements. The volume elements in the model were C3D4T types (linear coupled temperature-displacement), with about 530000 elements in the sample and about 140000 in the projectile. Meshes were refined in regions of the sample close to the indenter and crack tip region. A typical set of meshes is shown in Figure 6.3. The strain rate sensitive plasticity behaviour of the target material was simulated with the JC constitutive relation.

Simulation of the impact event was “halted” at the point when the residual energy contained in the projectile had fallen to 20% of its initial kinetic energy content - the predicted stress fields suggested that this was approximately the stage at which crack

initiation took place, determined from the conditions generated in a low impact velocity case where no fracture was observed. This involved constraining the projectile to stop and maintain its position. Following this, propagation of the crack was modelled by the presence of a cylindrical interface along which the (circular) crack front would advance. Initially, this interface was fully pinned - ie the boundary concerned was a fully cohesive one. The elastic strain energy stored in the system was evaluated. The interface was then unpinned (so that it was free to slide and/or open), up to a selected crack length, and this energy audit was repeated for the new (partially relaxed) stress field. This operation was repeated for different extents of crack front penetration, with the crack front effectively allowed to penetrate instantaneously. For each crack length (and associated crack face area), the strain energy release rate was taken to be the difference between the original and the new levels of stored elastic strain energy, divided by the new crack area created. In order to implement this procedure, while avoiding numerical instability, the time increment was reduced significantly.

It should be clarified at this point that this (pre-defined) cylindrical crack geometry is naturally only a crude reflection of the observed behaviour. The cracks certainly did not form as perfect cylinders. In fact, it would be difficult to establish exactly what crack path would be favoured, even for an isotropic, homogeneous continuum, and the (anisotropic, inhomogeneous) microstructure adds a further complication. Nevertheless, this crack geometry can be taken as broadly representative of the behaviour of the system.

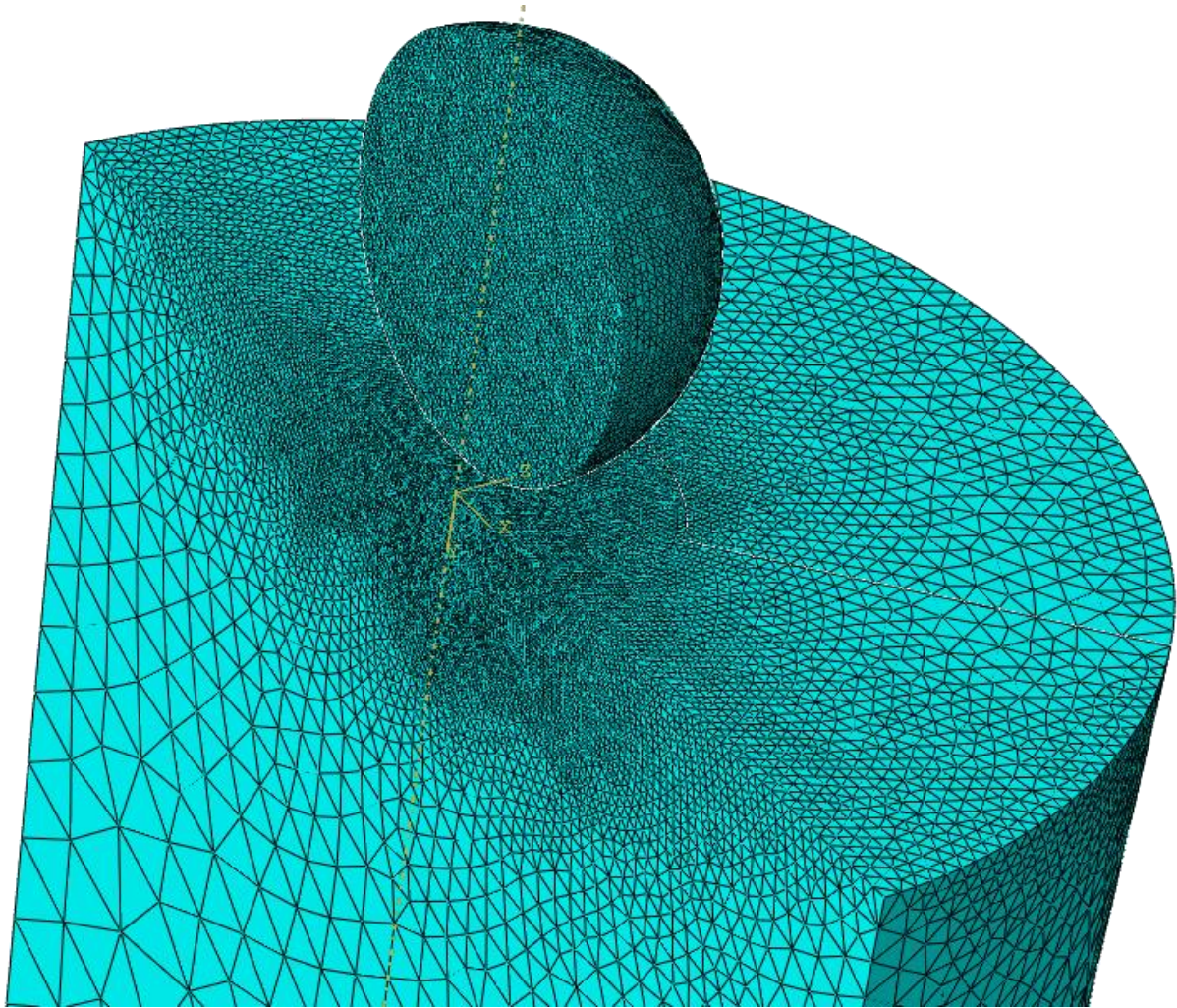


Figure 6.3 Typical mesh configurations for the FEM modelling of crack propagation in a ballistic event

6.1.4 Constitutive Laws

As with any FEM implementation of a constitutive law in the form of a family of curves, a rationale is required concerning the progressive deformation of individual volume elements. This will ideally be characterised by a small number of parameters. In the current work, it has been assumed that the cumulative (von Mises) strain defines the “state” of (a volume element of) the material. For the case of plasticity, this fixes the point on the appropriate stress-strain curve where the gradient is to be evaluated. This gradient defines what will now occur – i.e. determines the increase in flow stress needed to generate an imposed strain increment or, equivalently, determines how much straining will result from the availability of an increment of flow stress. By using the von Mises stress and strain in an expression based on uniaxial (quasi-static) testing, the von

Mises yielding criterion is implicitly being used to predict the onset of plasticity. This is common, although the effect of varying this criterion between von Mises and Tresca limits has been explored in the recent paper by Holmen et al [216]. A similar procedure is used for creep, where the accumulated creep strain, stress and temperature will determine the local creep strain rate, as depicted by Figure 6.4.

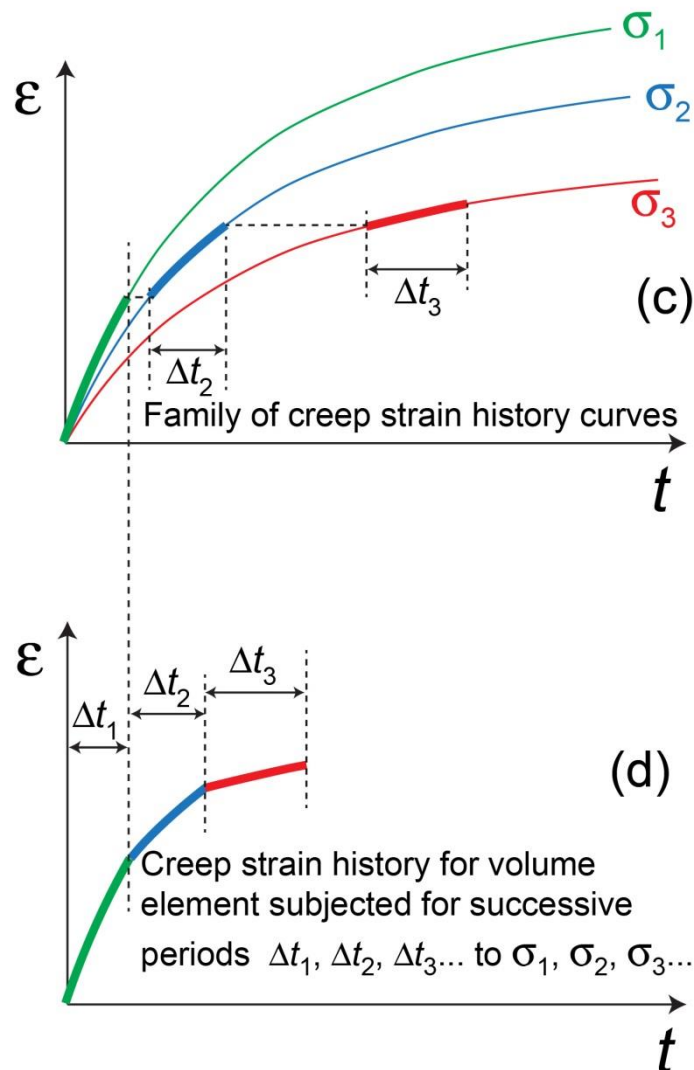


Figure 6.4 Schematic illustration of how the creep strain history of a volume element is assumed to be composed of a series of incremental strains, each dependent on the creep curve for the stress level concerned and the prior cumulative creep strain experienced by the element.

6.1.4.1 Creep

The expression used in the current work was the MN law [40], simplified for use at a single temperature, which may be written

$$\varepsilon_{\text{cr}} = \frac{C_2 \sigma^{n_2} t^{m_2+1}}{m_2 + 1} \quad (6.1)$$

where C_2 is a constant (units of $\text{MPa}^{-n_2} \text{s}^{-(m_2+1)}$), t is the time (s), n_2 is the stress exponent and m_2 is a dimensionless constant. This law is designed to capture both primary and secondary regimes of creep (and the transition between them). This is essential [199] for indentation creep work, in which a steady state (purely secondary creep) is never established. By differentiating with respect to time, we get

$$\dot{\varepsilon}_{\text{cr}} = C_2 \sigma^{n_2} t^{m_2} \quad (6.2)$$

which can be employed in order to obtain the increments of strain generated in a given volume element as it experiences a changing (deviatoric) stress throughout the test. The time can thus be expressed in terms of both strain rate and strain

$$t = \left[\frac{\dot{\varepsilon}_{\text{cr}}}{C_2 \sigma^{n_2}} \right]^{1/m_2} = \left[\frac{(1 + m_2) \varepsilon_{\text{cr}}}{C_2 \sigma^{n_2}} \right]^{1/(1+m_2)} \quad (6.3)$$

Eliminating t and rearranging allows the strain rate to be expressed as a function of the strain

$$\dot{\varepsilon}_{\text{cr}} = \{C_2 \sigma^{n_2}\}^{1/(1+m_2)} [(1 + m_2) \varepsilon_{\text{cr}}]^{m_2/(1+m_2)} \quad (6.4)$$

It is assumed that the cumulative creep strain defines the “state” of (a volume element of) the material, with the instantaneous creep strain rate determined by the current stress and the prior strain: the creep strain rate can thus be expressed solely as a function of the creep strain. This is depicted in Fig.6 and details of the algorithm are supplied elsewhere [236]. In summary, during each time increment, the net displacement of the indenter is found (within Abaqus) by monitoring the cumulative creep strain in each element up to that point, taking account of the (von Mises) stress in it, using Eqn.(4) to obtain the further strain that will arise in it during the time interval and then using compatibility conditions to solve and give the overall shape change of the domain.

6.1.4.2 Strain Rate Sensitive Plasticity

The strain rate sensitive plasticity properties were simulated using the JC constitutive relation,

$$\sigma_{\text{flow}} = \left[\sigma_Y + K (\varepsilon_p)^n \right] \left[1 + C \ln(\dot{\varepsilon}_p^*) \right] \left[1 - (T^*)^m \right] \quad (6.5)$$

For cases where Ludwik-Holloman was unable to effectively capture the quasi-static behaviour, the term characterising this was represented by a set of data pairs, to give

$$\sigma_{\text{flow}} = [\text{Data Pairs}] \left[1 + C \ln(\dot{\varepsilon}_p^*) \right] \left[1 - (T^*)^m \right] \quad (6.6)$$

Given that convergence involves only for the strain rate sensitivity parameter, C , the use of data pairs is not a computationally demanding adaptation, but allows for more flexible characterisation of the quasi-static plasticity.

6.1.5 Effect of Interfacial Friction

There is also the issue of the nature of the frictional contact between indenter / projectile and sample during the penetration. The standard representation of this effect (within ABAQUS) is to ascribe a coefficient of friction, μ , to the interfacial contact, such that sliding between the two surfaces requires a shear stress, τ , given by

$$\tau = \mu \sigma_n \quad (6.7)$$

where σ_n is the normal stress at the interface. The value of μ is clearly expected to depend on the surface roughness (of projectile and sample), and possibly on other factors, and so cannot be predicted *a priori*. For this work, the value used was 0.1.

6.1.6 Model Input Data

All material properties were assumed to be isotropic. The input data included the Poisson ratios and Young's moduli of material and indenter. Values for the material were taken directly from handbooks. The elastic constants for both the cermet and ceramic indenter materials were provided from the supplier, Bearing Warehouse Ltd.

The simulation of creep was carried out in load control, with the max load specified. Simulation of the ballistic experiment required specification of the thermal conductivity and heat capacity. Again, these were taken from handbooks. It was also necessary to specify an initial velocity for the projectile, after which it moved in free flight to strike the sample at normal incidence. The fraction of the plastic work converted to heat (Taylor–Quinney coefficient) was set at 95%. Slightly different values are sometimes used, but there is in any event no solid theoretical basis on which to estimate it - the underlying idea is that the remaining 5% goes mainly into the creation of new dislocations, so the value could be higher for a material that is already work-hardened, but it is not really viable to attempt any prediction. The values for all the material data used in this study are detailed in Tables 6.1 - 6.6.

Property	Units	Value	Source
Young's modulus	GPa	300	Handbook
Poisson's ratio	(-)	0.26	Handbook

Table 6.1 Summary of the Si_3N_4 indenter material property parameters values used in the study of creep behaviour.

Property	Units	Value	Source
Young's modulus	GPa	200	Handbook
Poisson's ratio	(-)	0.31	Handbook
C_2 (MN)	$\text{MPa}^{-n_2} \text{s}^{-(m_2+1)}$	$4.3\text{e}10^{-8}$	Indentation inferred
n_2 (MN)	(-)	2.46	Indentation inferred
m_2 (MN)	(-)	-0.65	Indentation inferred

Table 6.2 Summary of nickel material property parameter values used in the study of creep behaviour.

Property	Units	Value	Source
Young's modulus	GPa	650	Supplier
Poisson's ratio	(-)	0.21	Supplier
Density	kg m^{-3}	14800	Supplier

Table 6.3 Summary of the WC cermet projectile material property parameters values used in the study of strain rate sensitive plasticity and fracture.

Property	Units	Value	Source
Young's modulus	GPa	120	Handbook
Poisson's ratio	(-)	0.30	Handbook
Density	kg m ⁻³	8960	Handbook
Thermal conductivity	W m ⁻¹ K ⁻¹	401	Handbook
Heat capacity	MJ m ⁻³ K ⁻¹	3.45	Handbook
Inelastic heat fraction	(-)	0.95	Handbook
T_m (JC)	K	1356	Handbook
σ_y , K and n (JC)	Data-pair description		Quasi-static compression
m (JC)	(-)	1.09	Quasi-static compression
$\dot{\epsilon}_{p0}$ (JC)	s ⁻¹	5e-3	Quasi-static compression
T_0 (JC)	K	298	Quasi-static compression
C (JC)	(-)	0.016	Indentation inferred

Table 6.4 Summary of as-received copper material property parameters values used in the study of strain rate sensitive plasticity.

Property	Units	Value	Source
Young's modulus	GPa	120	Handbook
Poisson's ratio	(-)	0.30	Handbook
Density	kg m ⁻³	8960	Handbook
Thermal conductivity	W m ⁻¹ K ⁻¹	401	Handbook
Heat capacity	MJ m ⁻³ K ⁻¹	3.45	Handbook
Inelastic heat fraction	(-)	0.95	Handbook
T_m (JC)	K	1356	Handbook
σ_y , K and n (JC)	Data-pair description		Quasi-static compression
m (JC)	(-)	1.05	Quasi-static compression
$\dot{\epsilon}_{p0}$ (JC)	s ⁻¹	5e-3	Quasi-static compression
T_0 (JC)	K	298	Quasi-static compression
C (JC)	(-)	0.030	Indentation inferred

Table 6.5 Summary of annealed copper material property parameters values used in the study of strain rate sensitive plasticity.

Property	Units	Value	Source
Young's modulus	GPa	45	Handbook
Poisson's ratio	(-)	0.29	Handbook
Density	kg m ⁻³	1740	Handbook
Thermal conductivity	W m ⁻¹ K ⁻¹	156	Handbook
Heat capacity	MJ m ⁻³ K ⁻¹	1.77	Handbook
Inelastic heat fraction	(-)	0.95	Handbook
T_m (JC)	K	923	Handbook
σ_Y (JC)	MPa	30	Quasi-static compression
K (JC)	MPa	830	Quasi-static compression
n (JC)	(-)	1	Quasi-static compression
m (JC)	(-)	0.60	Quasi-static compression
$\dot{\epsilon}_{p0}$ (JC)	s ⁻¹	1e-3	Quasi-static compression
T_0 (JC)	K	298	Quasi-static compression
C (JC)	(-)	0.026	Indentation inferred

Table 6.6 Summary of magnesium material property parameters values used in the study of strain rate sensitivity study and fracture.

6.1.7 Model Output Data

For the creep indentation experiment, the model output was displacement-time data. For the ballistic simulations, the model output was displacement-time and residual profile. For the residual profile, the height from the target surface as a function of the radial position was compared with experiment. An internal energy audit was used to assess the strain energy released during crack propagation.

6.1.7.1 Binned Plastic Strain Rates

An investigation has also been made into how the plastic work is distributed in terms of the local strain rate during the deformation. After each increment of time, for each volume element, the stress, incremental strain and strain rate are recorded. The work done during that time interval is evaluated (= stress \times strain \times volume) and that increment of work is associated with the strain rate concerned. Expressed mathematically, the increment of work done in the j th volume element during the k th time increment is

$$\Delta W_{j,k} = \sigma_{j,k} \Delta \varepsilon_{j,k} V_j \quad (6.8)$$

Clearly, the work done during the k th time increment is given by

$$\Delta W_k = \sum_{j=1}^{j=M} \Delta W_{j,k} \quad (6.9)$$

where the summation is over the total number (M) of volume elements, and the total work done is

$$\Delta W_{tot} = \sum_{k=1}^{k=Z} \Delta W_k \quad (6.10)$$

with this summation being over the total number (Z) of time increments. The total strain rate range is divided into a number of sub-ranges (bins) and the work done within each range is then evaluated after a binning operation. This can be expressed as

$$\Delta W_{bin,p} = \sum_{k=1}^{k=Z} \sum_{j=1}^{j=M} (\Delta W_{j,k} f_{j,k,p}) \quad (6.11)$$

where $f_{j,k,p}$ is a function ascribed a value of 1 or 0, depending on whether the strain rate associated with the increment of work $\Delta W_{j,k}$ does or does not fall within the range of the p th bin.

6.2 Convergence Procedure

6.2.1 Convergence Algorithm and Procedure for Creep Indentation

For the characterisation of creep parameters, the algorithm used to converge in parameter space on the best fit combination of parameter values is the Nelder-Mead simplex search [237]. This was chosen in view of its robustness and adaptability, particularly with respect to noise. The procedure used is based on that of Gao and Han [238], and was built using the Scientific Python and Numeric Python packages [239, 240]. Full details are available elsewhere [191]. In order to check the presence and successful identification of a global minimum, convergence procedures were initiated from multiple points in C_2 , m_2 and n_2 space. Convergence should lead to the same set of C_2 , m_2 and n_2 values in each case.

The goodness-of-fit between target and modelled data (displacement-time data) is characterised here via a dimensionless parameter S_{red} , a “reduced sum of squares of the residuals”.

$$S_{red} = \frac{\sum_{i=1}^N (\delta_{i,M} - \delta_{i,E})^2}{N \delta_{N,E}^2} \quad (6.12)$$

where $\delta_{i,M}$ and $\delta_{i,E}$ are respectively the modelled and experimental values of the displacement, at times varying from 0 up to t_{max} (split into increments of Δt and with the counter i varying from 1 to N). The actual number of measured values would commonly run into thousands, but a typical value of N would be of the order of 500, so some filtering and averaging of the raw data was employed. The normalising displacement, $\delta_{N,E}$, is the experimental value at the end of the run ($i = N$). The convergence procedure is terminated when a criterion is met. This can be defined as a minimum change in S_{red} from one iteration to the next.

This operation could be carried out for just a single run – i.e. for a single value of the applied load, P . However, in the current work, two runs (with different values of P) were carried out, so two $\delta_{i,E}$ datasets were available. For each combination of MN parameter values (giving a $\delta_{i,M}$ dataset for each P), the S_{red} value was calculated in each case and the numerical average taken. In this way, equal weighting was given to the two runs. Of course, more runs could be included in this operation, although it is important to note that even a single run creates a wide range of (changing) stress levels within the sample, up to a level predetermined by the load P and the penetration ratio of the recess ($\delta_{o,E} / R$, where R is the indenter radius).

For ballistic experimentation, an equivalent form of Equation 6.12 was used. For the displacement-time data, values of δ were compared at time intervals of the order of 1.4 μ s. For the residual indent shape, displacement (height) differences were evaluated at r intervals of about 100 μ m. The total number of points at which comparisons were made (N) for the displacement-time data was 30 for the as-received copper and the magnesium samples and 50 for the annealed samples. (These values of N were chosen to ensure similar weighting was given to the penetration and rebounding parts of the motion.) For the residual indent shape data, $N = 50$ was used for all samples.

As for the corresponding parameter for plasticity [3], S_{red} is thus a positive dimensionless number, with a value that ranges upwards from 0 (corresponding to perfect fit). Modelling that captures the material creep response well should lead to a solution (set of parameter values) for which S_{red} is relatively low – say, less than 10^{-3} . This effectively constitutes a health check on the solution – if, for example, no solution can be found giving a value smaller than, say, 1%, then this suggests that there can only be limited confidence in the inferred set of values. This could be due to experimental deficiencies and/or an inability to capture the behaviour well with the constitutive law being used. In fact, during the work described here, a solution with an S_{red} value well below 10^{-3} was found, representing very good agreement.

Chapter 7

A Methodology for obtaining Primary and Secondary Creep Characteristics from Indentation Experiments, using a Recess

7.1 Introduction

The (indentation creep, with iterative FEM) procedure, as previously employed, incorporates a major difficulty. It is important, when carrying out creep testing, to avoid (time-independent) plastic deformation. During conventional (uniaxial) creep testing, this is easily achieved by ensuring that the applied stress level is below the yield stress (for the temperature concerned). During indentation creep testing, however, the induced stress levels tend to be very high initially (when the contact area between the indenting sphere and the flat surface of the sample is small). Some plasticity is difficult to avoid during this phase, even if attempts are made to ramp up the applied load in some controlled way. This is doubly unfortunate, since (a) the displacement due to plasticity is difficult to separate from that due to creep during this initial period and (b) inducing plastic deformation may change the microstructure in such a way as to affect the creep response.

During the current work, a spherical recess was introduced in the sample before the start of the test, with the same radius as the indenter. This innovative measure reduces the stress levels induced in the sample when the load is applied (removing the need for any phase during which it is ramped up). For any selected recess depth, use of the FEM model will allow the stress field in the sample to be predicted, making it easy to ensure that the maximum (deviatoric) stress does not exceed the yield stress. Furthermore,

selection of the depth provides a measure of control over the complete range of stress levels that will arise during the test (for a given applied load).

The shape of the recess should match that of the indenter. It may in practice not be important for the matching to be very good (since local irregularities are likely to be quickly removed once the creep testing has started), but in the present work an attempt was made to obtain excellent matching. It should be noted that a typical indenter radius is expected to be of the order of 1-2 mm. Since this is relatively coarse (ensuring that a representative volume of the sample is being mechanically interrogated), the scale of the recess is such that conventional machining procedures can be employed to create it. On the other hand, the region being tested is still relatively small, so the sample can be small and the mapping of properties over a relatively large sample is still possible.

A recess of approximately the desired shape and depth was first created, following the procedure outlined in §5.1.2.1. The process of honing the recess (by ~40 μm) is expected to remove the bulk of surface material, which is likely left in a work-hardened state. The scale of the indentation, with the stress field penetrating to a depth on the order of 1 mm should mean that surface effects from the machining stage are negligible. Furthermore, by using a profilometer (optical or contact), the actual shape of the indent can be accurately captured and this can be used both to check on whether the surface finish and overall topography are acceptable and also to create the FEM mesh that will be used during iterative simulation of the indentation test. Since the depth of the recess is likely to be of the order of at least several hundred microns, the resolution requirements of the profilometry are relatively undemanding - a value of the order of 1 μm is typically sufficient. A scan to the axis of the recess is shown in Figure 7.1.

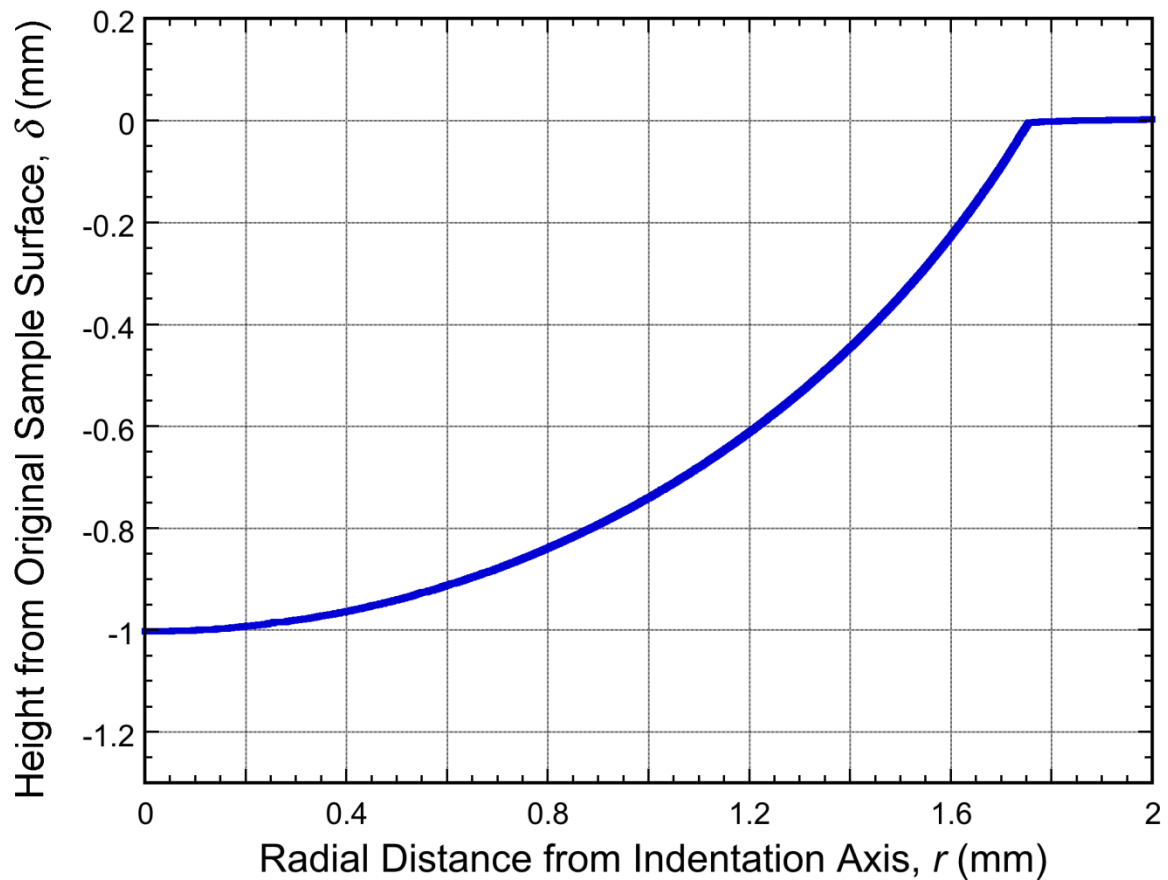


Figure 7.1 Profile across a recess, measured using a contact stylus.

7.2 Microstructure

An optical micrograph is shown in Figure 7.2, where it can be seen that the grain size was around 50-100 μm and the grain structure was approximately equiaxed. The temperature of all tests was fixed at 750°C. It was confirmed that the degree of oxidation of these samples, at this temperature, was negligible.

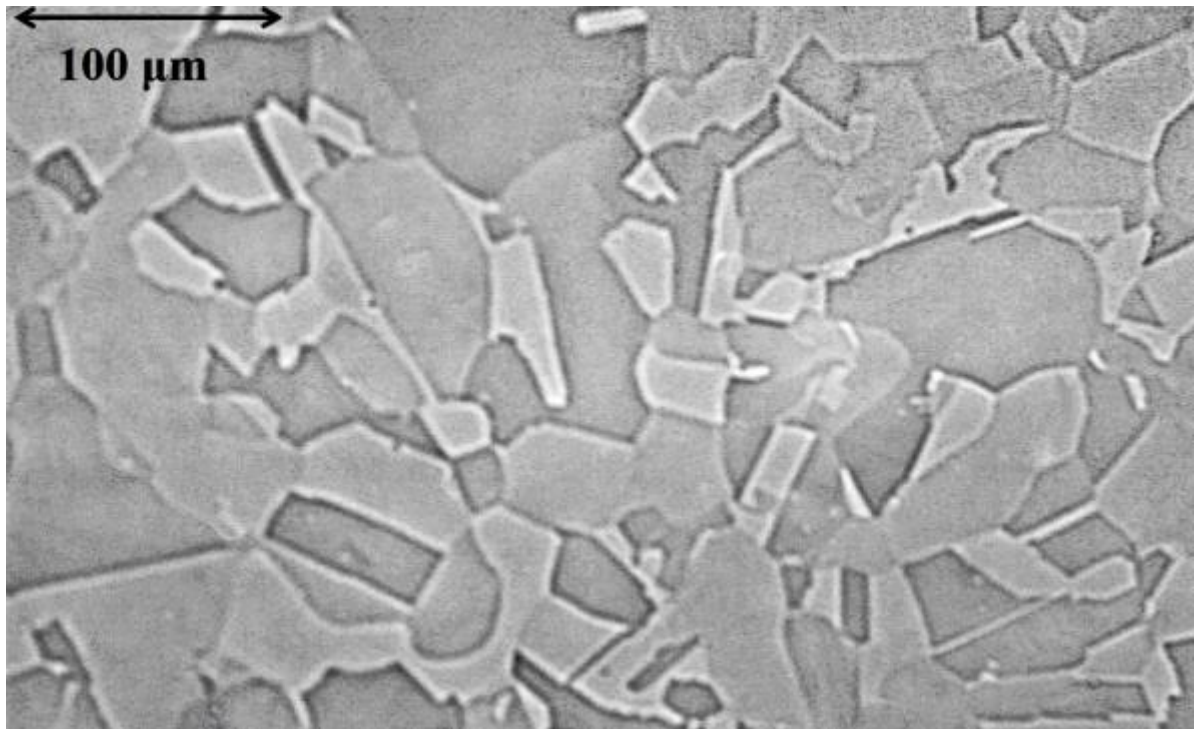


Figure 7.2 Optical Micrograph of the nickel.

7.3 Quasi-static Plasticity

A typical outcome for uniaxial plasticity at 750°C is shown in Figure 7.3, which presents the data as both nominal stress against nominal (plastic) strain and true stress against true plastic strain. It can be seen that the yield stress is about 66 MPa, with some subsequent work hardening. In order to avoid the onset of plasticity in the uniaxial creep experiments, the (nominal) stress levels employed were 35, 45 and 55 MPa.

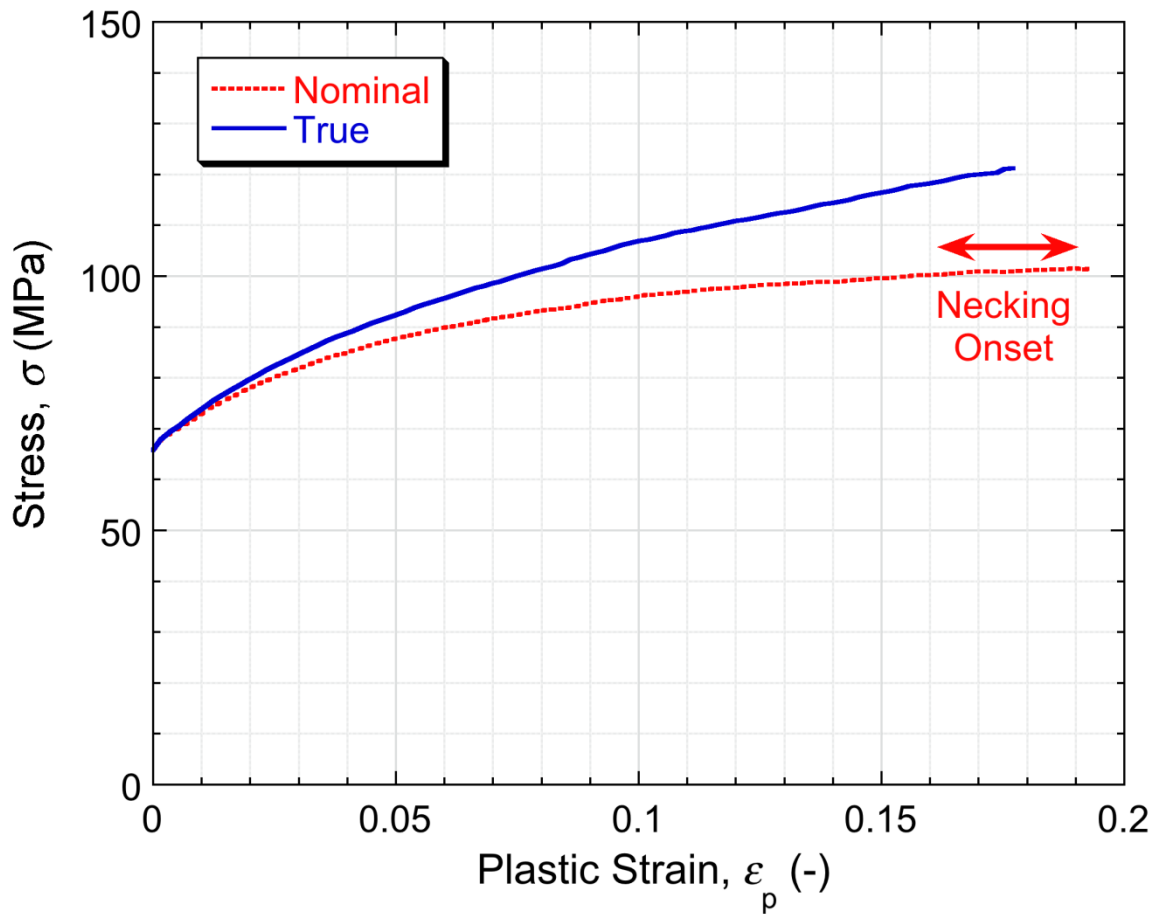


Figure 7.3 Tensile stress-strain curves for the nickel at 750°C, plotted as both nominal stress v. nominal strain and true stress v. true strain (obtained via the analytical relationships, assuming that the stress and strain fields remained uniform throughout).

For a creep recess indentation test, the von Mises stress field created when a load of 1 kN is first applied is shown in Figure 7.4. It can be seen that, save for a tiny volume, the stress levels in the sample do not reach the yield stress. It may be noted that, during this type of test, the stress levels will tend to fall as the indenter penetrates more deeply into the sample. This is not necessarily the case during conventional plastic deformation, when work hardening can cause stress levels below an indenter to rise as it penetrates more deeply.

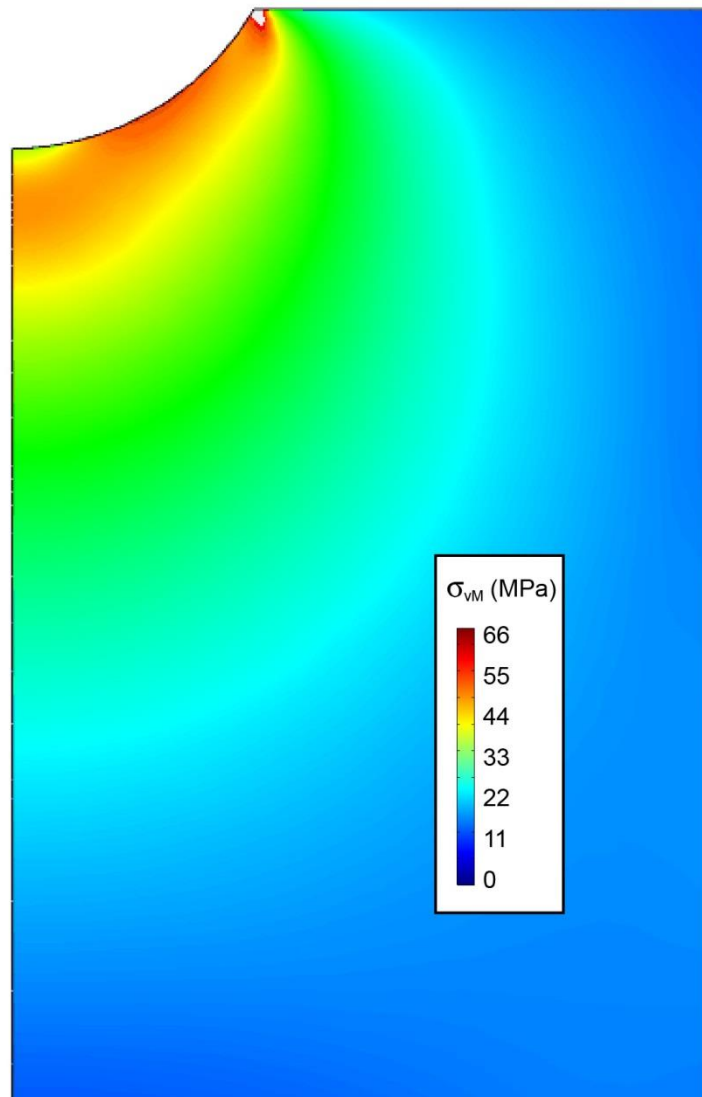


Figure 7.4 Predicted von Mises stress field within the sample on application of a load of 1 kN to an indenter of radius 2 mm, with a prior spherical recess created in the sample, having the same radius as the indenter and a depth of 1 mm.

7.4 Uniaxial Tensile Creep Results

The outcomes of tensile creep testing with the 3 different levels (35 MPa, 45 MPa and 55 MPa) of applied (nominal) stress are shown in Figure 7.5. It can be seen that these all exhibited shapes broadly expected of creep strain curves, with those for the higher stress levels showing what appear to be “tertiary” regimes of increasing strain rate towards the end of the test - i.e. at strains of the order of 10%. There is also a clear “primary” regime in all cases, which for these tests constituted a significant proportion of the test (in terms

of both strain and time). In fact, at least for the two higher stress levels, there is not really any well-defined “secondary” regime of constant strain rate. This is actually quite representative of much creep testing, at least with relatively high stress levels.

It may be noted that, at least for the 55 MPa test, the true stress level started to exceed 60 MPa, and thus became quite close to the measured yield stress (of about 66 MPa) in the “tertiary” regime. For the 45 MPa test, on the other hand, the true stress was still below 50 MPa at the time when the strain rate started to rise. This effect can be seen in Figure 7.5, where the rise in true stress over the duration of each test is shown on axis y_2 .

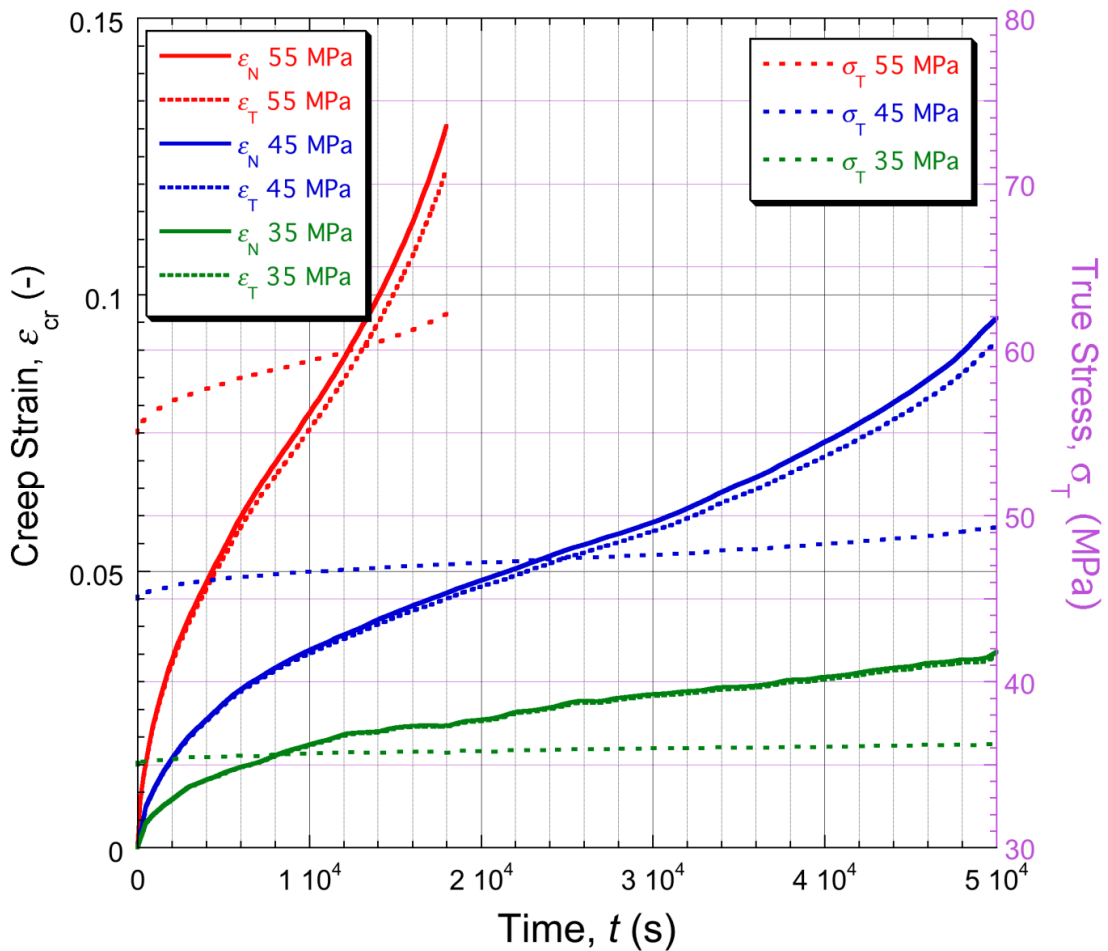


Figure 7.5 Experimental data from tensile creep testing with three different (nominal) stress levels. Both nominal and true creep strains are plotted. Also shown are the changing values of the true stress during each of these tests.

7.5 Indentation Creep Results

The experimental indentation (displacement-time) data for the two loads employed are shown in Figure 7.6, together with corresponding predictions for the (best fit) set of MN parameter values shown. Also shown are the final S_{red} values obtained in each case. Convergence on these best fit values is illustrated by the plots shown in Figure 7.7, in which the misfit parameter value is the average of those for the two loads. It can be seen that convergence was achieved within about 60-80 iterations. This is broadly typical, although it does depend on the starting point in parameter space. A series of random starting points (one of which can be seen by inspection of Figures 7.7(b), 7.7(c) and 7.7(d)) were used in this work to help ensure a global minimum had been identified. If there were some prior information available about the likely values of the parameters, then a starting point could be chosen that was closer to the “correct” answer, in which case convergence would be quicker. The real time required to reach a solution was fairly short, although of course this will depend on the computational power available.

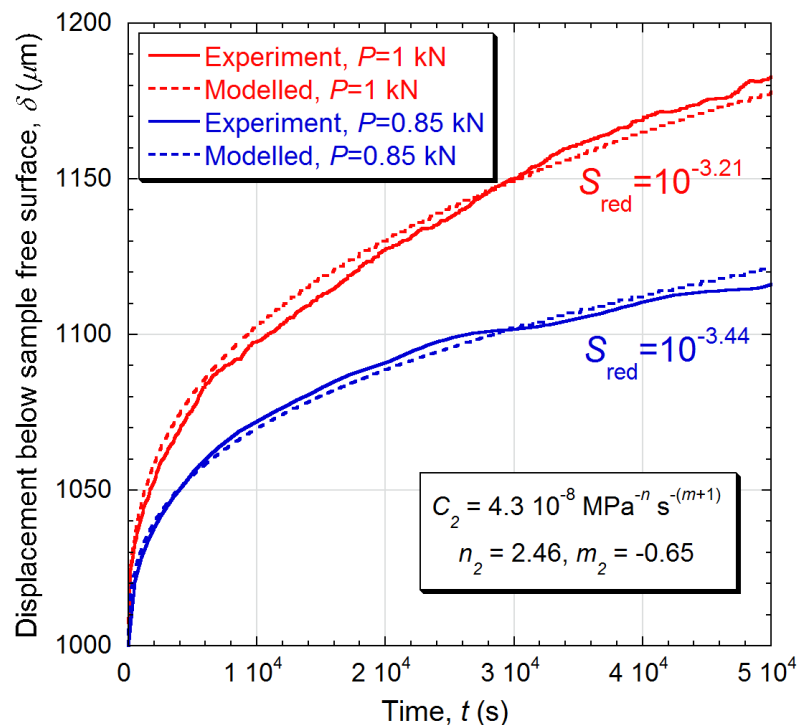


Figure 7.6 Comparison between measured and (best-fit) modelled penetration histories during indentation with two different applied loads. Also shown are the best fit MN parameter values and the final values of the misfit parameter in each case.

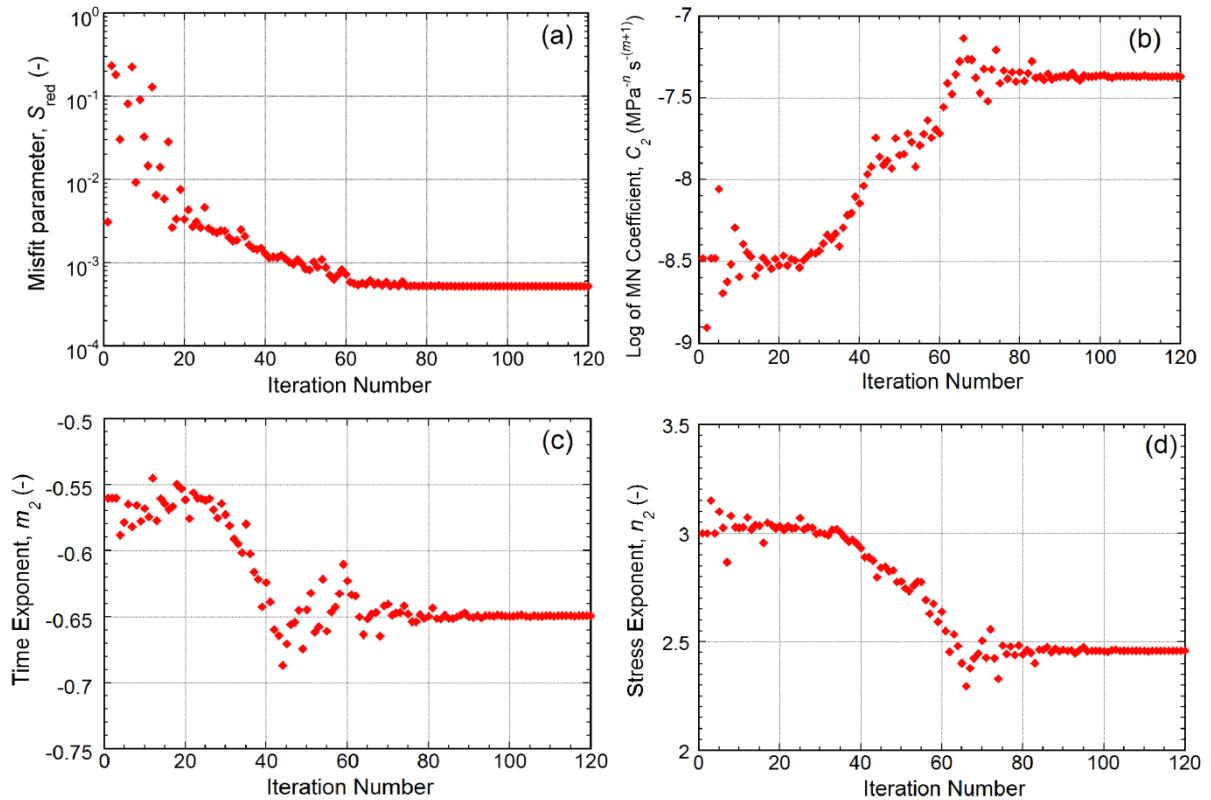


Figure 7.7 Nelder-Mead convergence on an optimal MN parameter set, targeting the two displacement-time plots during indentation, showing the evolution with iteration number of: (a) the goodness-of-fit parameter, S_{red} , (b) the MN coefficient, C_2 , (c) the time exponent, m_2 and (d) the stress exponent, n_2 .

7.6 Tensile Creep Curves from Indentation Outcomes

The main objective is to obtain conventional (tensile) creep data (for any selected level of applied stress), at least in primary and secondary regimes, solely from indentation experiments - in fact, essentially from a single indentation experiment. All that is required is the best fit set of MN parameter values. These can then be used to predict the outcome of creep testing with any configuration, including, of course, the simple one of uniaxial tensile testing. In fact, for that case, it's not even necessary to carry out any further FEM modelling, since a tensile creep test is one in which the stress and strain field tends to remain homogeneous. This is not true for compressive creep, when friction and barrelling tend to be significant. A comparison between the outcome of

a tensile creep experiment and a prediction based on indentation-derived values of the MN parameters can therefore be made via simple manipulation of the MN equation (§6.1.4.1).

The outcome of such an operation can be seen in Figure 7.8, where the experimental plots of the nominal creep strain as a function of time (from Figure 7.5) are compared with corresponding predicted plots obtained using the indentation-derived MN parameter values. Two sets of these are shown. The first is simply the curve corresponding to Equation 6.1, with the true creep strain obtained in that way converted to a nominal strain and the stress used in the equation being fixed at the nominal value. The second is based on the strain rate form of the MN expression – i.e. Equation 6.2. This has been implemented by stepping through a series of time increments, calculating the latest strain rate by taking into account the changing value of the true stress. This is how the MN expression should be used, since both the stress and the strain in it are true values. It can be seen that doing this makes a significant difference to the predicted curves, although in these cases it does not lead to any increase in the overall strain rate with increasing time. This would tend to happen at higher strains, depending on the value of n_2 .

The most striking feature of Figure 7.8 is that the agreement between conventional tensile creep testing and the indentation-derived outcome is in general very good, at least within the primary and secondary regimes. The “tertiary” regime, which is quite noticeable with the highest level of applied stress, is not captured, even by using the MN formulation in a way that takes account of the increasing level of true stress in such tests. It is possible that this discrepancy is due to the true stress starting to approach the yield stress at the temperature concerned. If this happens, then it is expected that the behaviour will not be captured well using a creep model of this type, and plasticity characteristics (including the work hardening rate) are likely to have an effect. In fact, any analytical formulation, such as the MN law, is likely to be reliable only within a certain range of (true) stress. The corresponding creep strain rate against time plot can

be seen in Figure 7.9, from which a similar set of conclusions can be drawn. Only the indentation inferred curves from Equation 6.2 are shown.

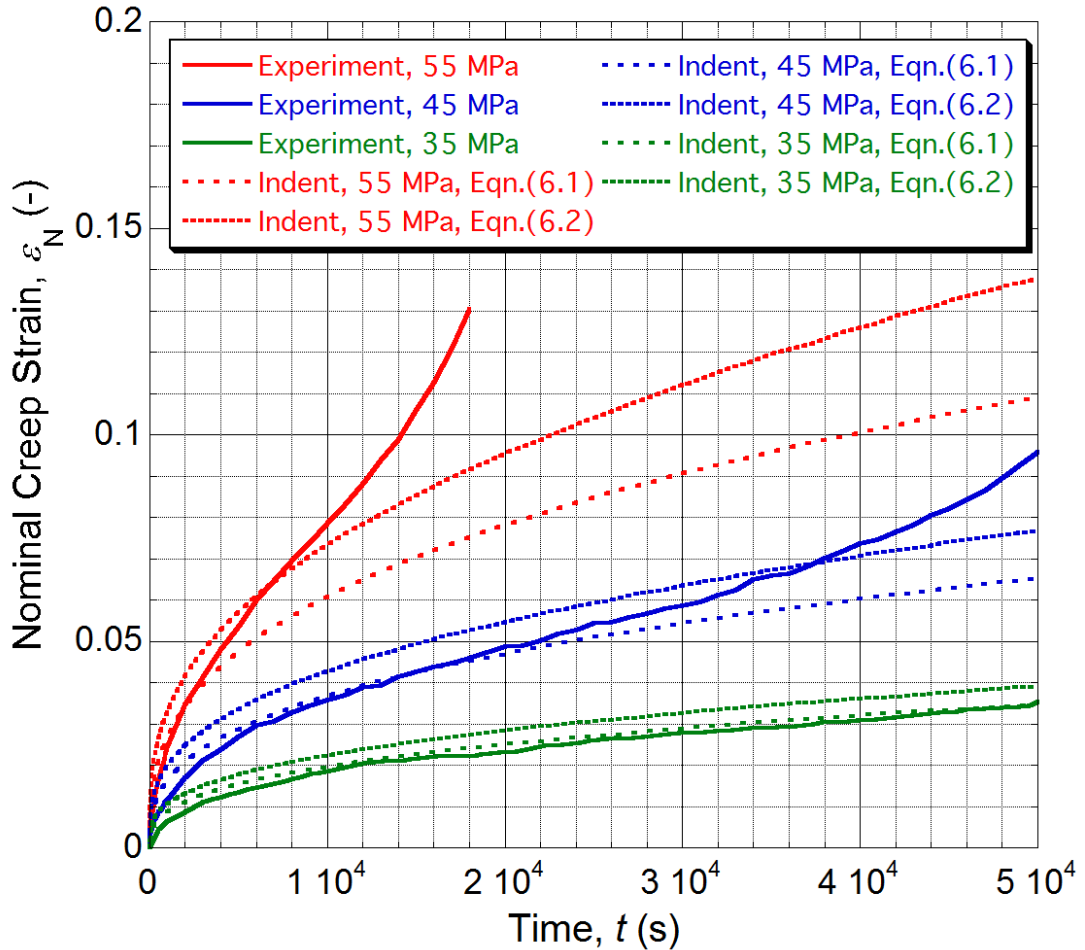


Figure 7.8 Comparison between creep strain curves obtained by conventional tensile testing, with a fixed nominal stress, and those obtained via iterative FEM modelling of indentation creep with a constant applied load, using the MN expression in one of two forms.

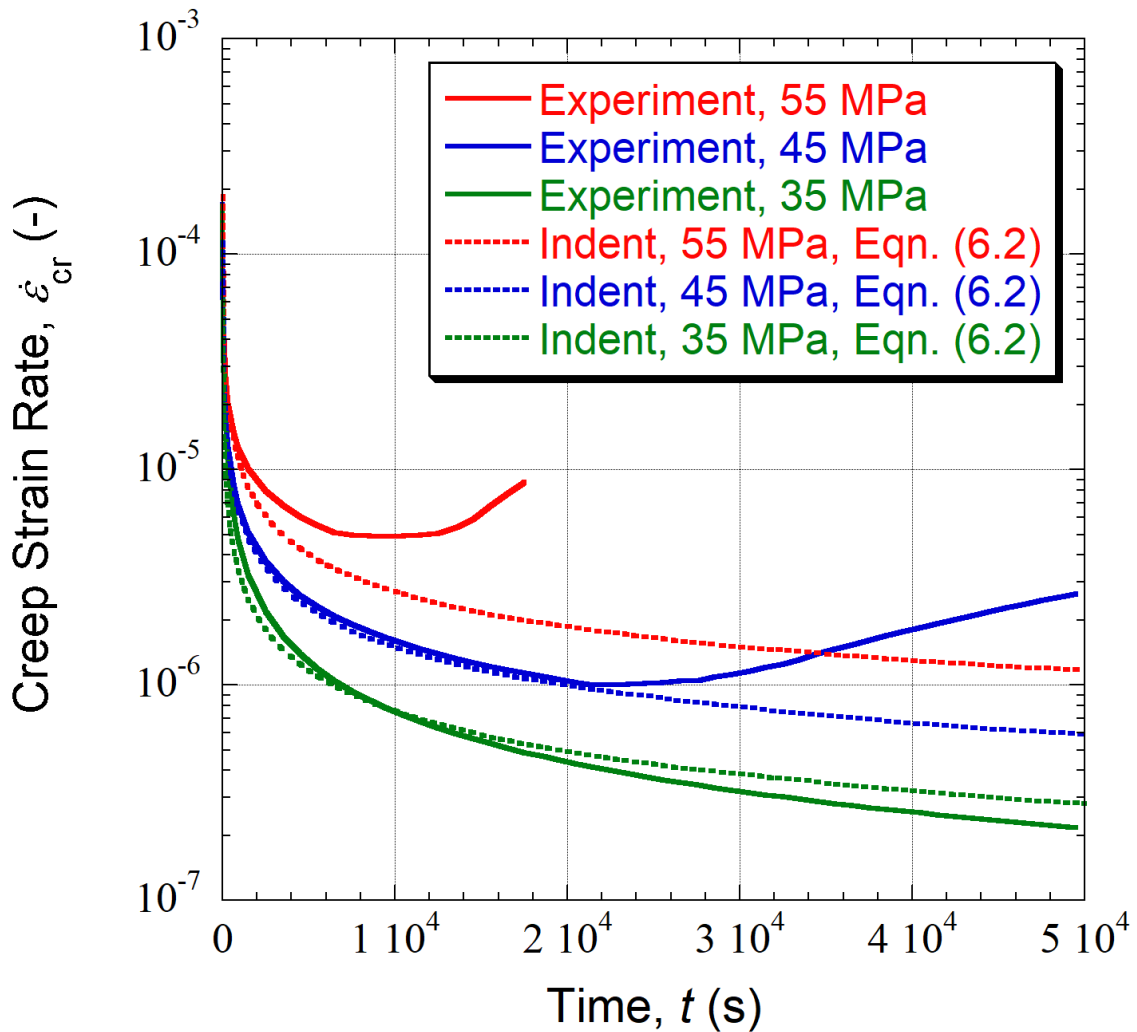


Figure 7.9 Comparison between creep strain rate curves obtained by conventional tensile testing, with a fixed nominal stress, and those obtained via iterative FEM modelling of indentation creep with a constant applied load, using the MN expression.

It is of interest to note the range of stress and strain generated within an indentation test of this type, since it is clear that creep characteristics well outside of these ranges are unlikely to be captured well by such a test. Figure 7.10 shows fields of (von Mises) stress and creep strain within the sample at the end of the simulation with an applied nominal stress of 55 MPa. This is actually after a time of 5×10^4 s, whereas the corresponding tensile creep test was stopped after about 1.8×10^4 s, when the strain rate was becoming very high. This case therefore reflects a relatively severe test, in terms of generating high stresses and strains. It can immediately be seen, on comparing Figure 7.10(a) with Figure 7.4, that the stress levels have relaxed somewhat as the indenter has

penetrated, and all of these stresses are well below the yield stress. It can also be seen from Figure 7.10(b) that the creep strains generated within the sample range up to about 10-15%, which is appropriate for the comparisons shown in Figure 7.8.

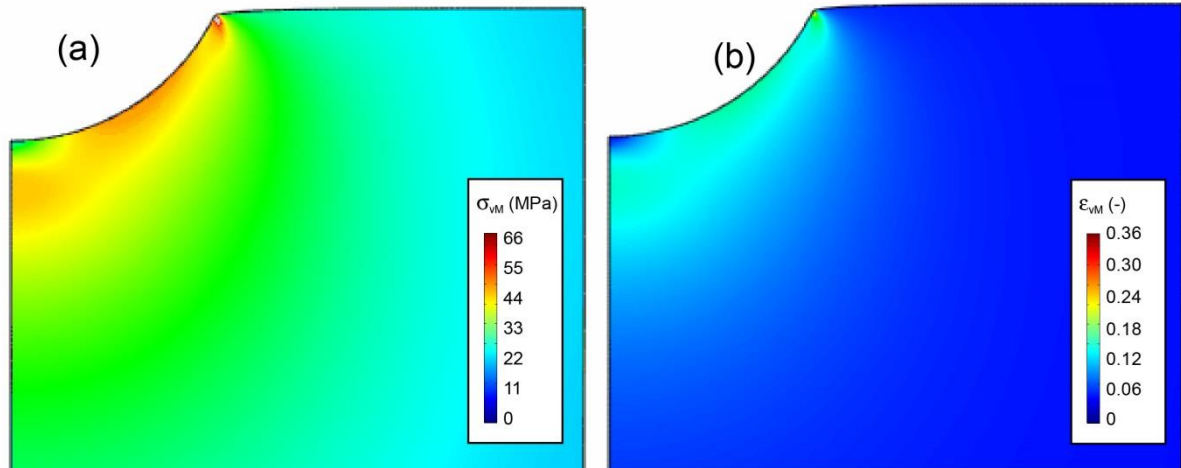


Figure 7.10 Predicted von Mises (a) stress and (b) strain fields within the sample 5 10⁴ s after application of a load of 1 kN to an indenter of radius 2 mm, with a prior spherical recess created in the sample, having the same radius as the indenter and a depth of 1 mm.

Finally, it can be seen in Figure 7.10 that there is some “pile-up” around the indent, although it is not very pronounced. Of course, during conventional plastic deformation, such pile-ups can be quite noticeable, particularly for materials that exhibit little work hardening (allowing large plastic strains to develop near the pile-up). In general, while there is no clear analogue during creep deformation to a “work hardening” effect, there is a tendency for the stress and strain fields to become more “diffused” than during plastic deformation, such that pile-up (or “sink-in”) effects are likely to be small.

7.7 Summary

A procedure is described for iterative FEM simulation of the creep deformation that takes place during penetration of a spherical indenter into a sample (under constant applied load). The target outcome is a penetration-time dataset and convergence is obtained via optimisation of the set of 3 parameter values in the MN creep law (covering both primary and secondary regimes). An important part of the procedure is the prior production on the sample surface of a recess that matches the (spherical) shape of the

indenter. This ensures that the stresses in the sample can be kept below the yield stress throughout the indentation test, so that conventional plasticity (and the associated complications) can be avoided.

Experimental work has involved a single material (pure nickel) at a single temperature (750°C). Both conventional uniaxial (tensile) creep tests, using three values for the applied (nominal) stress, and creep indentation testing, under a constant applied load, have been carried out. It is recognized that this constitutes a fairly limited dataset and the results presented are intended mainly to demonstrate the methodology and to obtain some preliminary indications regarding its reliability. Good agreement is observed between the strain-time plots obtained by conventional testing and by using the (MN) creep parameter values inferred via the indentation testing. The stress exponent obtained in this way has a value of about 2.5.

A final “tertiary” regime was observed with the higher stress level tensile tests, which was not captured well in the indentation-derived MN curves. It seems likely that this arose because the true stress was approaching the yield stress, such that conditions were outside the regime that could be represented at lower stress levels by a MN creep law with a single set of parameter values. Indeed, it may be that some conventional plastic deformation was starting to take place in the “tertiary” regime.

Chapter 8

Johnson-Cook Parameter Evaluation from Ballistic Impact Data via Iterative FEM Modelling

8.1 Microstructure

The grain structures (in transverse section) are shown in Figure 8.1. It can be seen that the grain size was of the order of 30–50 μm in the as-received material, but had coarsened to about 300–400 μm after annealing (following recrystallization and grain coarsening) . Some annealing twins are also present.

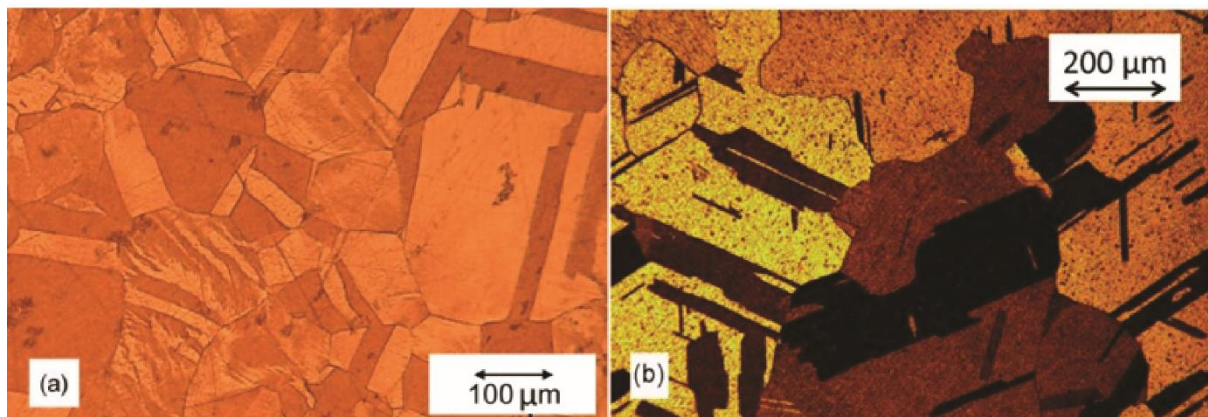


Figure 8.1 Optical micrographs of transverse sections of the extruded copper (a) as-received (b) after annealing.

8.2 Quasi-static plasticity

8.2.1 Stress-strain plots for ambient temperature

Data from typical compression tests (along the extrusion axis) with each material are shown in Figure 8.2(a), plotted as both nominal and true values. The variation between tests was in general very small (<1%). It can be seen that, as a true stress – true strain

relationship, the as-received material (Figure 8.2(a)) exhibits little or no strain (work) hardening. This is not unexpected, since the extrusion process left the material in a heavily cold-worked state. The annealed material, on the other hand, exhibits substantial strain hardening from the outset (Figure 8.2(b)), with the relative change in flow stress during straining being much greater than that for the as-extruded material. This is also unsurprising for an annealed material. However, it does lead to a complication in the present context, in terms of representing the behaviour using Equation 6.5. It should be noted that, while these uniaxial experiments often cannot be regarded as reliable beyond strains of the order of 20–25% (due to necking / failure in tension and barrelling in compression), strain levels well above this (perhaps of the order of at least 200%) can be generated during projectile impact, and are thus likely to be employed in the FEM model.

Under these circumstances, use of the Equation 6.5 with Ludwik-Hollomon parameter values fitted over the low strain regime leads to prediction of unrealistically high flow stresses at high strains. In practice, the flow stress is not expected to exceed that of the as-received material - they are, of course, basically the same material, apart from work-hardening effects. This behaviour therefore can't be represented realistically over a large strain range using the L-H equation. The solution adopted for the annealed material has therefore been to use sets of data pairs in the FEM model, conforming to the experimental outcome for low strains and constrained to conform to the yield stress values for the swaged samples (after well-defined degrees of prior cold work). This is illustrated in Figure 8.2(b), which compares experimental data with extrapolated sets of data pairs, extending in both cases up to very high strains (~300%), as per Equation 6.6.

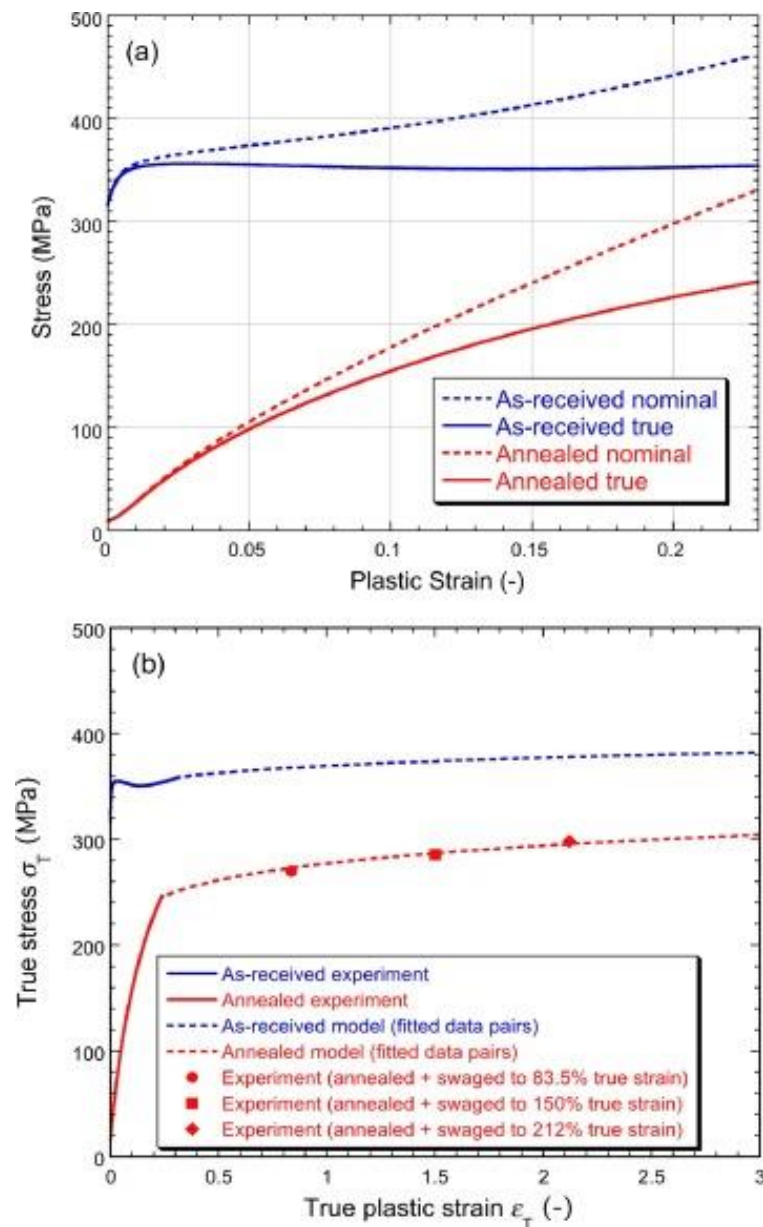


Figure 8.2 Room temperature experimental and modelled quasi-static stress-strain plots for the two materials, showing (a) typical compression test data and (b) comparisons between modelled and measured plots of true stress against true strain, with the model representations shown up to high strain levels.

A comment is needed here with regard to the outcome of this procedure for the annealed material. It's clear that the curve does not have the expected shape around the transition between the directly measured range (up to about 20%) and the regime in which the flow stress has been obtained from the swaged samples. In practice, a smoother transition in gradient is expected. There are possible explanations for this discrepancy. For example, the swaging would have created more heating than the quasi-

static loading, which may have promoted a degree of microstructural recovery during the process, hence softening the material somewhat. However, it would be difficult to compensate in any way for such effects and it seems simpler to just follow the described procedure, accepting that there are inevitably limits on the reliability of the (quasi-static) stress-strain curves.

The effect of anisotropy (due to crystallographic texture) is illustrated in Figure 8.3, which compares the plots obtained by loading in axial or radial directions, for both materials. It can be seen that there is an effect, which is slightly more noticeable for the annealed material. Of course, the ballistic indentation was carried out only in the axial (extrusion) direction, but in that case the deformation is much more multi-axial than during compression testing, so that the overall response is expected to lie between the axial and radial extremes. If the objective were to obtain the quasi-static stress-strain curve from indentation data, and comparisons were being made with uniaxial outcomes, then this anisotropy would need to be taken into account. However, since the focus here is on the strain rate sensitivity, the exact shape on the base stress-strain curve is not expected to have a strong influence and so the data from axial testing were used in the modelling.

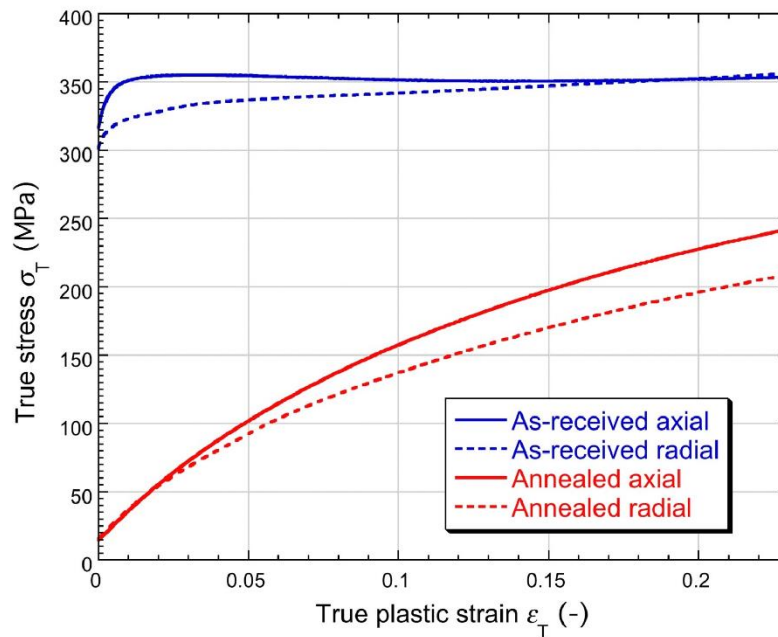


Figure 8.3 Experimental uniaxial compression stress-strain plots for both materials, showing outcomes from loading in both axial and radial (transverse) directions.

8.2.2 Stress-strain plots for elevated temperatures

True stress – true strain plots are shown in Figure 8.4 for the four temperatures employed, together with best-fit modelled curves. In the temperature sensitivity part (third term in Equation 6.6), the melting temperature, T_m , was taken to be 1356 K and ambient temperature, T_0 , to be 295 K. The dependence of the flow stress on temperature is reflected in the value of m (in Equation 6.6), with a low value giving a high sensitivity. It can be seen in the figure caption that the best-fit values of m were respectively 1.09 and 1.05 for as-received and annealed material.

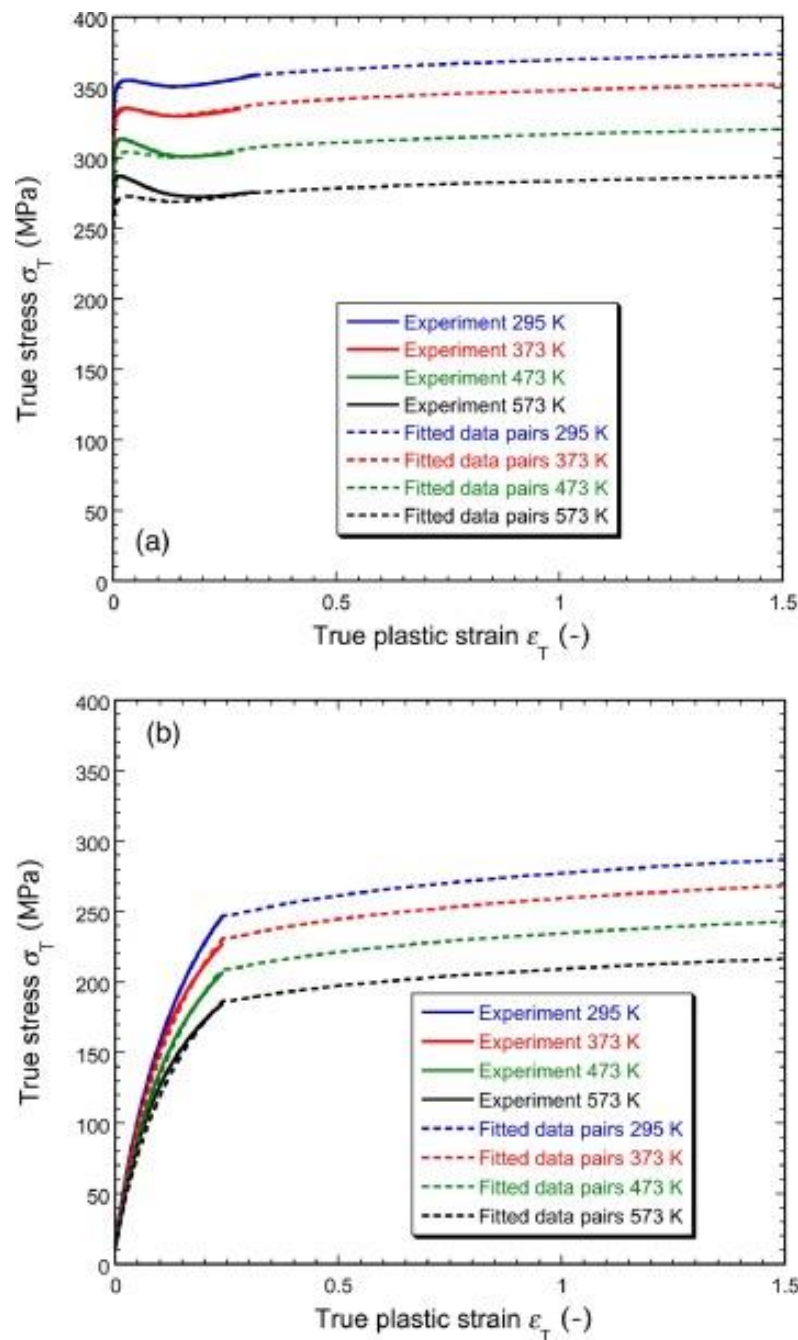


Figure 8.4 Quasi-static true stress - true strain plots (experimental and modelled) over a range of temperature, for (a) as-received and (b) annealed materials. The value used for the temperature dependence parameter, m , is 1.09 in (a) and 1.05 in (b).

There are difficulties associated with only being able to obtain experimental data over a strain range that is considerably smaller than the range likely to be experienced during an impact event, and also with the fact that this is purely an empirical curve-fitting exercise. Nevertheless, these modelled curves probably capture the quasi-static

behaviour reasonably well. The as-received material does appear to undergo a small degree of initial strain softening (under axial loading), perhaps associated with liberation of some dislocations as straining starts (in an initially strain-hardened material).

8.3 Evaluation of the strain rate sensitivity parameter, C

8.3.1 Conditions during projectile penetration

The local conditions (fields of stress, strain, strain rate and temperature) after different degrees of penetration (δ/R values) naturally depend on both the incident velocity and the hardness (plasticity characteristics) of the sample. The present work covers two materials with very different hardness levels and, in each case, a range of impact velocities (covering a factor of about 3). It is helpful to be broadly aware of the nature of these fields in different cases, since this will give an indication of the ranges of strain, strain rate and temperature over which the stress-strain curves are expected to affect the response of the material.

Such predicted outcomes can, of course, only be obtained if a value is assumed for C . However, while this is unknown *a priori*, simply taking a value in the range that is broadly expected (eg. ~ 0.03) is acceptable for the present purposes. A set of illustrative outcomes is shown in Figure 8.5, which refers to the annealed material subjected to impact at 70 m s^{-1} , for 3 times after initial impact (the last corresponding to the point when the projectile has reached maximum penetration depth). The cumulative strains are shown in Figure 8.5(a), where it can be seen that these peak at around 60%, with the region that has experienced fairly substantial strains ($> \sim 30\%$) extending by the end of penetration to significant depths below the surface ($\sim 1 \text{ mm}$). The strain rates (Figure 8.5(b)) peak at $\sim 3 \cdot 10^5 \text{ s}^{-1}$, but these occur only transiently in a small volume and most of the plastic deformation takes place at rates below 10^5 s^{-1} . Nevertheless, the figure does confirm that, even with this relatively low velocity, most of the plastic deformation takes place above 10^4 s^{-1} . This is related to Figure 8.5(c), which shows that the flow stress at which much of the plastic deformation occurs is above the quasi-static value in the strain

range concerned, which is ~ 300 MPa (at ambient temperature) - see Figure 8.4(b). This confirms that strain rate hardening effects are significant (for this value of C). Finally, Figure 8.5(d) confirms that the temperature rises are not very significant (less than 60°C). This is a relatively low impact velocity (and copper is a very good conductor, assisting in dissipation of the heat evolved).

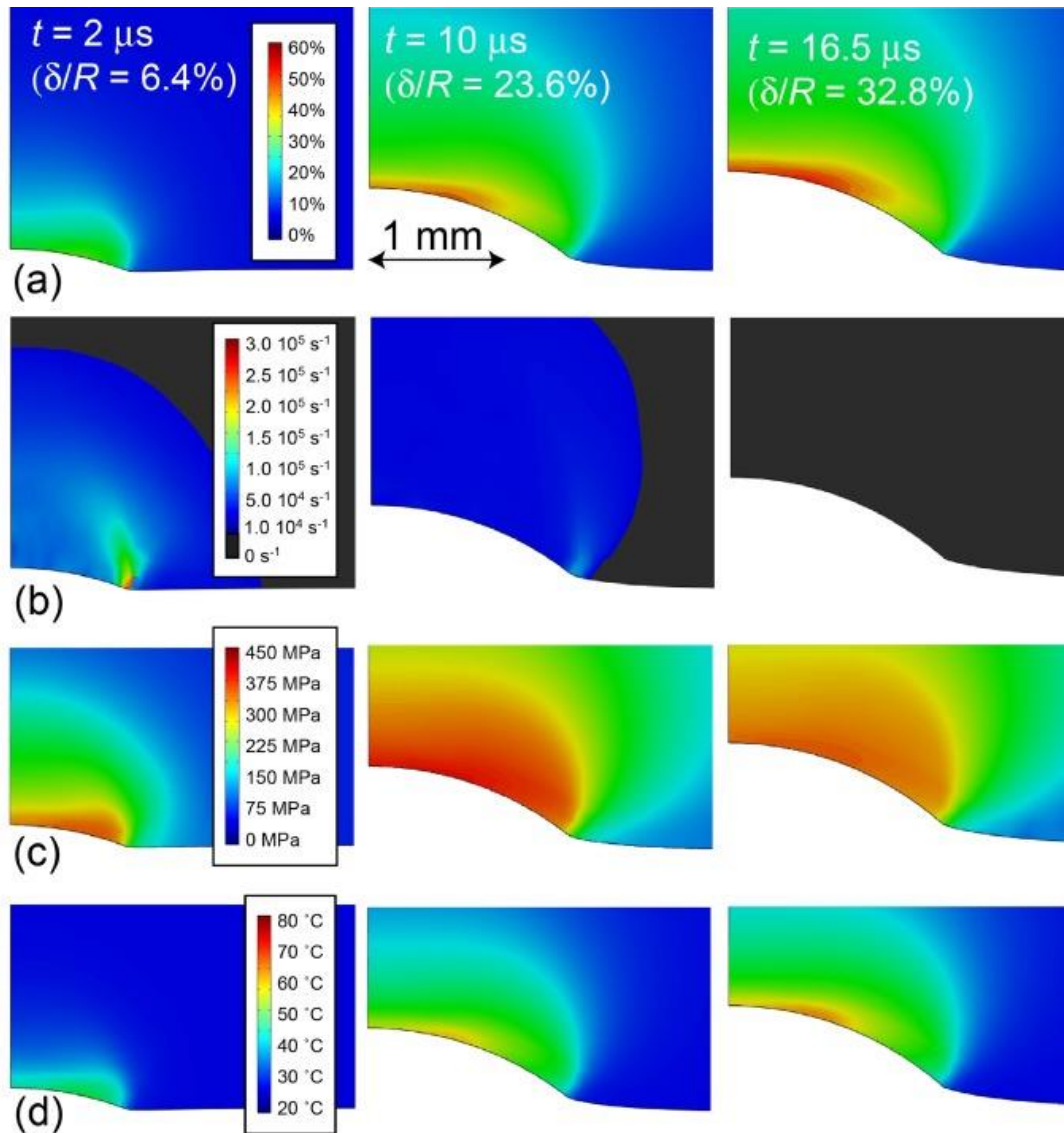


Figure 8.5 Predicted FEM outcomes for the annealed material, with an incident projectile velocity of 70 m s^{-1} (assuming a strain rate sensitivity parameter, C , of 0.03), showing (a) total (von Mises) plastic strain, (b) strain rate, (c) deviatoric (von Mises) stress and (d) temperature, at 3 different times after initial impact.

The influence of projectile velocity is illustrated by Figure 8.6, in which the corresponding fields to those in Figure 8.5 are presented for 200 m s^{-1} . As expected (since the incident kinetic energy is now greater by almost an order of magnitude), penetration is much deeper (almost to the “equator” of the ball) and the strains, strain rates, stresses and temperatures also reach higher values. However, some are increased more than others. It can be seen in Figure 8.6(a) that the cumulative strains are raised considerably, reaching peaks of over 200% in places and exceeding 100% in relatively large volumes of material. Strain rates are also somewhat higher than for the lower velocity, peaking at nearly 10^6 s^{-1} , although again this is only for short periods in small volumes. The peak stress levels, on the other hand, are rather similar to those for the lower velocity impact and they drop off more quickly as the ball penetrates. This is due to the effect illustrated in Figure 8.6(d), which shows that the temperature rises more quickly, and reaches relatively high values ($>150 \text{ }^\circ\text{C}$) in a fairly large volume, bringing down the stress levels.

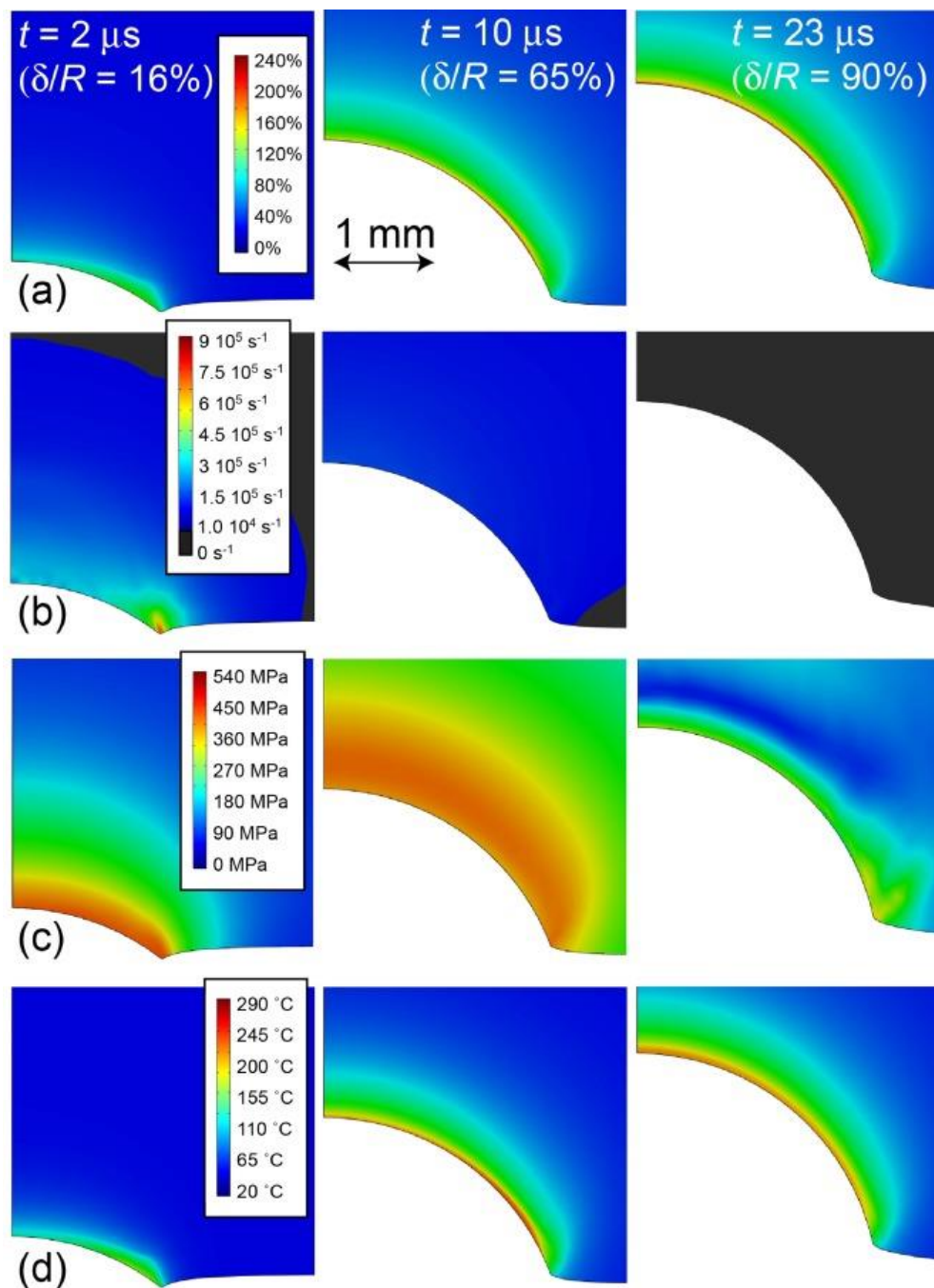


Figure 8.6 Predicted FEM outcomes for the annealed material, with an incident projectile velocity of 200 m s^{-1} (assuming a strain rate sensitivity parameter, C , of 0.03), showing (a) total (von Mises) plastic strain, (b) strain rate, (c) deviatoric (von Mises) stress and (d) temperature, at 3 different times after initial impact.

The material response for these two impact velocities will thus be sensitive to different parts of the family of stress-strain curves, with the main difference being that in the high velocity case there will be a greater sensitivity to the high strain regime (well beyond the limits of conventional uniaxial testing). For the as-received (work hardened)

material, the behaviour will be different again, with strains being lower, but stresses being higher. Furthermore, the change in (quasi-static) flow stress as straining occurs will be less (and there is less uncertainty about the nature of the work-hardening). Of course, the two materials may have different strain rate sensitivities (values of C). There are no well-established ground rules for even approximate prediction of the value of C in different cases, although there might be an argument for expecting softer materials (such as the annealed material) to have higher values (since, when the quasi-static mobility of dislocations is high, larger changes in flow stress might be expected to result from imposing strain rates beyond levels that can be achieved by normal dislocation glide).

It should be noted that the peak strain rates are less important than the distribution of values that are effective locally while plastic deformation is occurring. This distribution is illustrated in Figure 8.7(a) and (b), which provide data for both materials, with two different impact velocities. As expected, the average strain rate (weighted by the amount of plastic work done) is higher for the higher impact velocities, although the differences are not very great. (The average strain rates, weighted by plastic work, are $5.4 \cdot 10^4$ and $1.3 \cdot 10^5 \text{ s}^{-1}$ for (a) and $2.4 \cdot 10^4$ and $7.1 \cdot 10^4 \text{ s}^{-1}$ for (b)). A higher strain rate makes the material harder, tending to limit the amount of strain that occurs and hence reduce somewhat the amount of deformation occurring at such rates. On the other hand, with the initially softer material (Figure 8.7(b)), while more deformation occurs, the strain rates tend to be lower than for the harder material. These plots demonstrate that the predominant strain rate range in these experiments is of the order of 10^4 – 10^5 s^{-1} , with values up to $\sim 10^6 \text{ s}^{-1}$ being generated in the harder material.

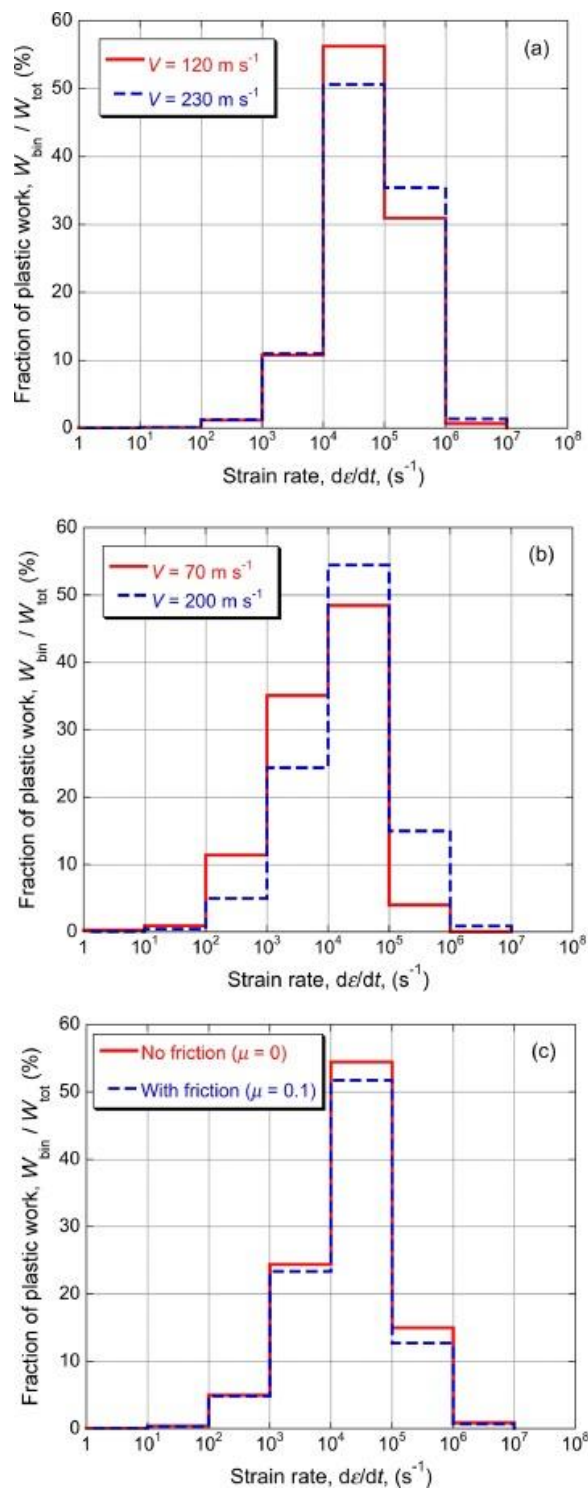


Figure 8.7 Histograms of strain rate ranges within which plastic work was done ($C = 0.03$). Plots (a) and (b) relate to as-received and annealed materials, with two impact velocities and no friction, while plot (c), which is for the annealed material, with $V_i = 200 \text{ m s}^{-1}$, shows the effect of friction.

Finally, the significance of the frictional work is illustrated by Figure 8.7(c), which compares (for the annealed material, with an impact velocity of 200 m s^{-1}) the strain rate distribution of the plastic work, obtained with the best fit value for μ of 0.1, with that in the absence of friction ($\mu = 0$). The plastic work done is lower when friction is included (due to some of the incident energy being absorbed by frictional sliding). It can be seen that this is a small, but not insignificant, fraction of the total work. It is also apparent that the frictional work is more significant in the higher strain rate regime, which is consistent with this taking place under conditions where the normal stress at the interface (i.e. the contact pressure) is higher.

8.3.2 Evaluation of C for the as-received material

Illustrative comparisons for the as-received material are shown in Figure 8.8 between model outcomes and experimental data, with 3 different incident velocities, in terms of projectile displacement histories and residual indent shapes. These predictions are for a particular value of C (0.016). It can be seen that, in both cases, the agreement is fairly good (S_{red} values around 10^{-2} – 10^{-4} in all cases). Such comparisons were made for a range of C values, with the misfit parameter, S_{red} , being evaluated in each case. The outcome of this set of comparisons is summarised in Figure 8.9, which shows plots of S_{red} as a function of C , for each type of comparison, and for each of the 3 impact velocities. While the outcome is not entirely consistent, optimum values of C are mostly around 0.016. It should be recognised that this procedure constitutes a comprehensive examination, not only of the value of C , but also of the reliability of the JC formulation. The outcome does suggest that it is at least approximately valid, with, for this (work-hardened) material, the appropriate value of C apparently being $\sim 0.016 \pm 0.005$.

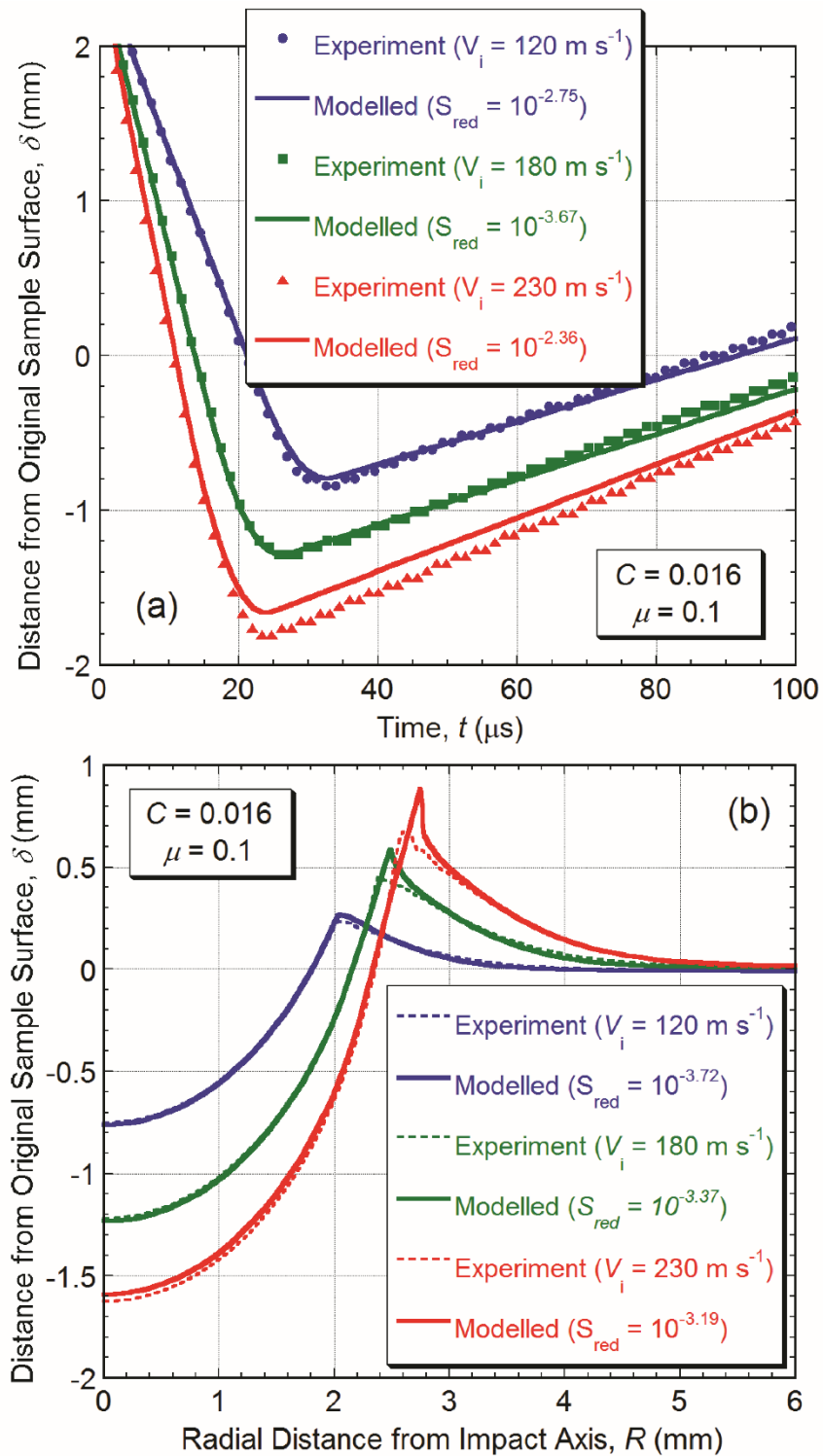


Figure 8.8 Comparisons, for 3 different impact velocities, between model predictions (with $C = 0.016$ and $\mu = 0.1$) and experimental data, for the as-received material, showing (a) displacement histories (from high-speed photography) and (b) residual indent shapes (from profilometry). The level of agreement in each case is characterised by the values shown for the misfit parameter, S_{red} .

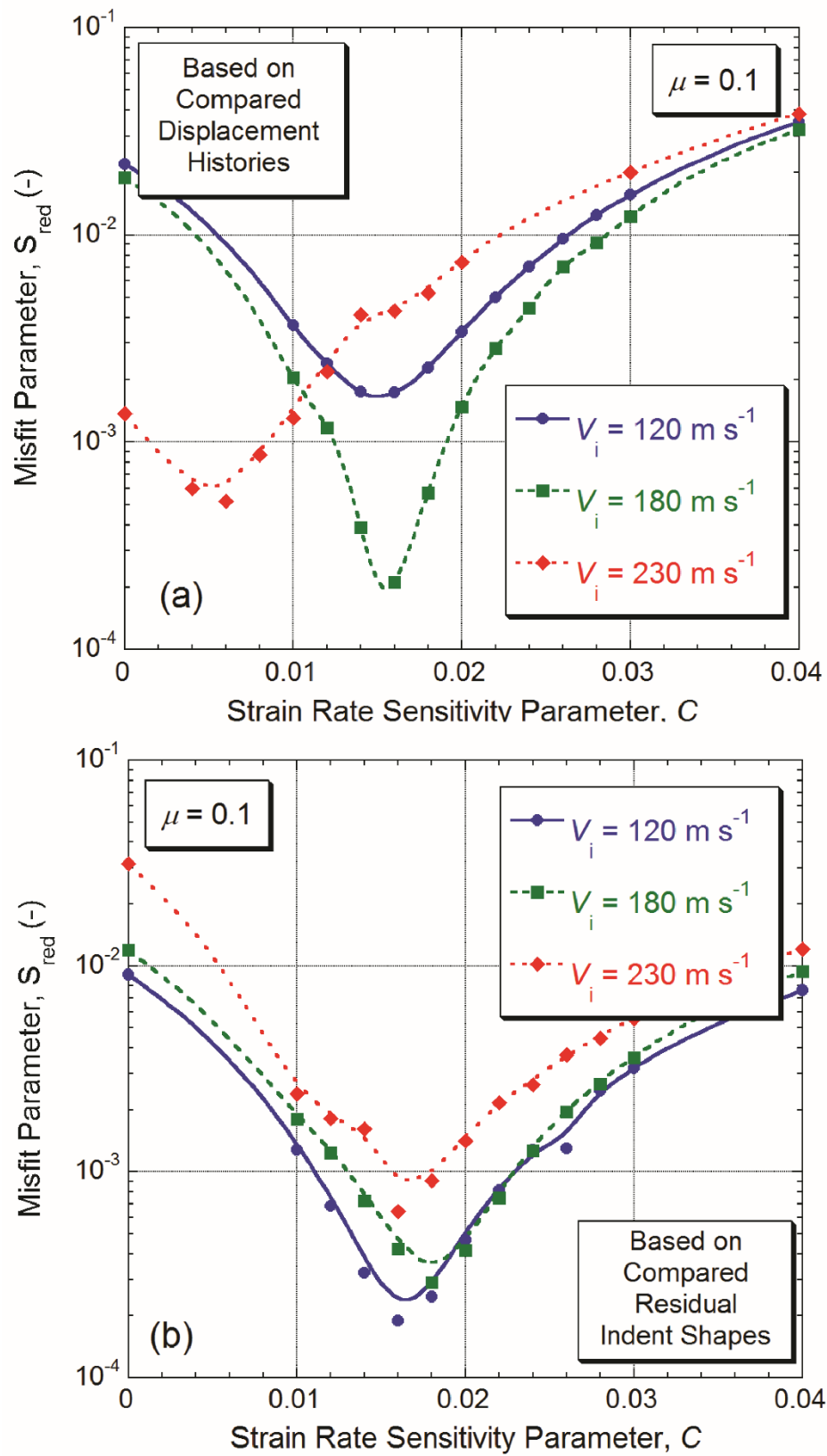


Figure 8.9 Plots, for 3 different impact velocities, of $S_{red}(C)$, for the as-received material, based on (a) projectile displacement histories and (b) residual indent shapes.

8.3.3 *Evaluation of C for the annealed material*

Corresponding plots to Figures. 8.8 and 8.9, for the annealed material, are shown in Figures. 8.10 and 8.11. The comparisons in Figure 8.10 are for $C = 0.030$. It can be seen that agreement is again quite good, with this value of C , for both high-speed photography and profilometry data. It is also clear from the $S_{red}(C)$ plots in Figure 8.11 that a higher value of C than for the as-received material gives the best agreement for the annealed samples. Again, the agreement is not perfect. In particular, the plots for the $V_i = 70 \text{ m s}^{-1}$ case appear to be a little inconsistent, apparently indicating a best-fit C value above 0.04 for the displacement data and below 0.02 for the indent shape data. This could be at least partly attributable to the fact that the strain rates were relatively low in this case, which is likely to introduce errors into the inferred value of C . Taken overall, the results for the annealed material indicate that the most appropriate value of C is about 0.030 ± 0.010 .

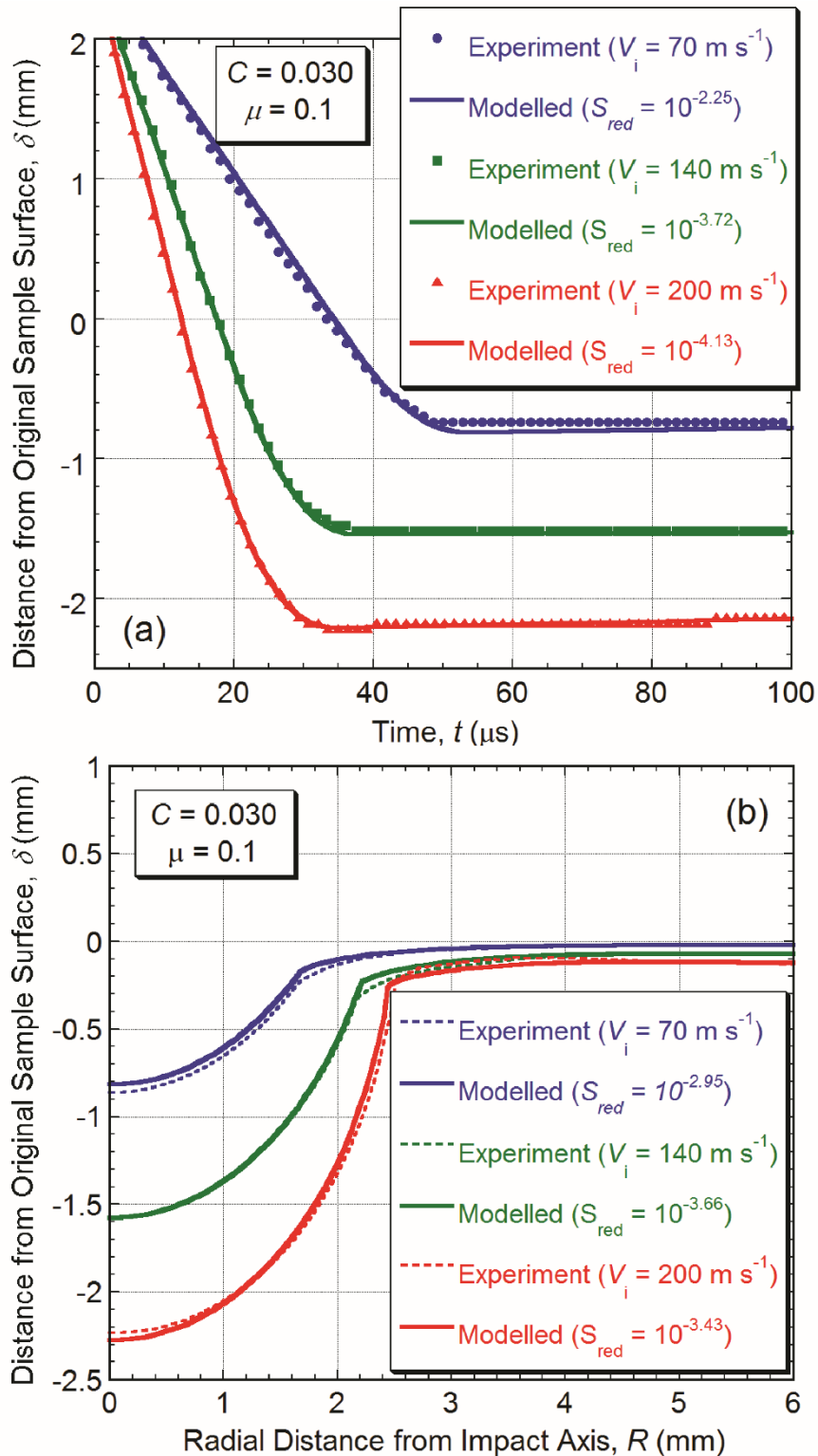


Figure 8.10 Comparisons, for 3 different impact velocities, between model predictions (with $C = 0.030$ and $\mu = 0.1$) and experimental data, for the annealed material, showing (a) displacement histories (from high-speed photography) and (b) residual indent shapes (from profilometry). The level of agreement in each case is characterised by the values shown for the misfit parameter, S_{red} .

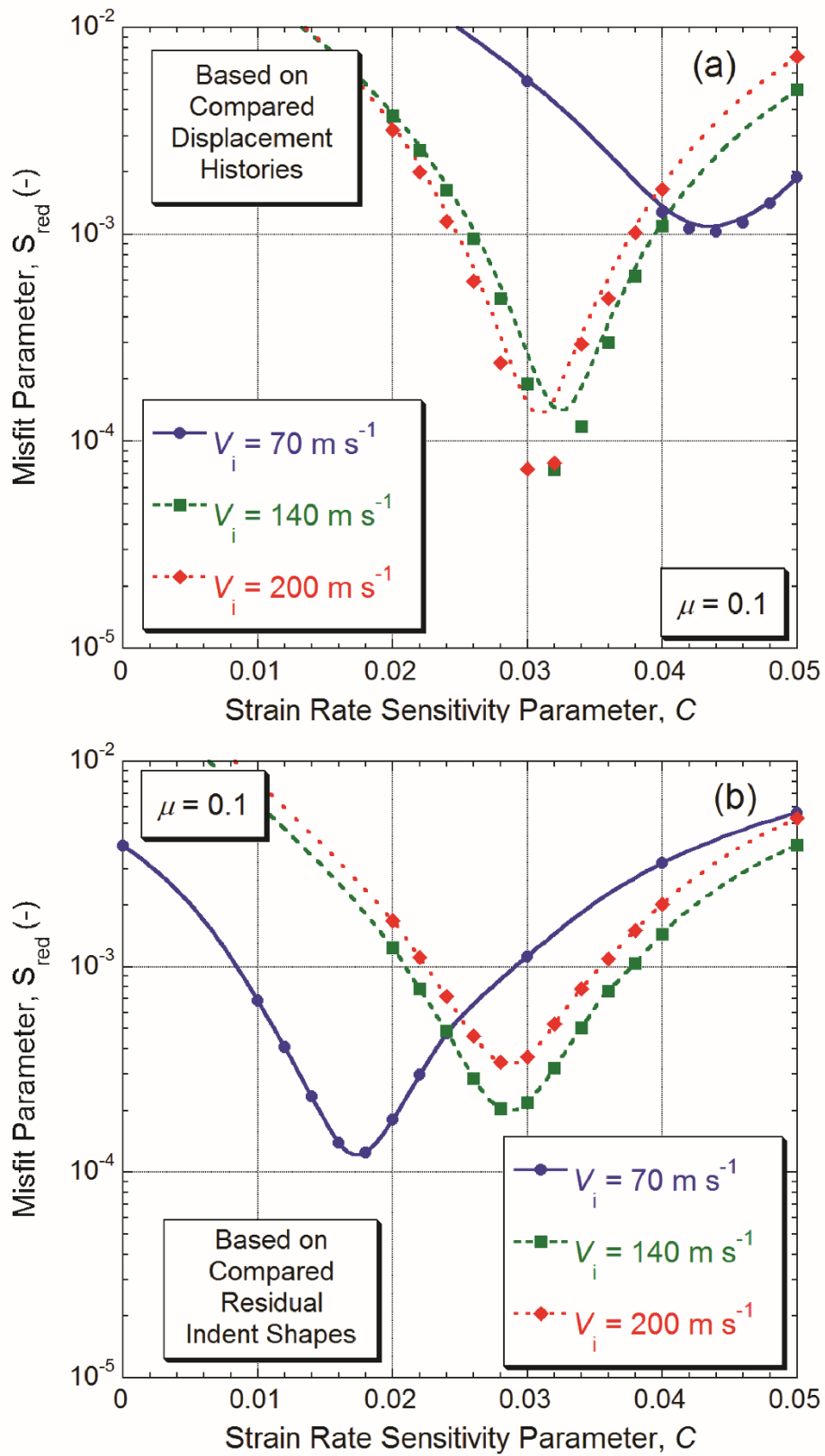


Figure 8.11 Plots, for 3 different impact velocities, of $S_{red}(C)$, for the annealed material, based on (a) projectile displacement histories and (b) residual indent shapes.

8.3.4 *Reliability of the inferred values of C*

While it is difficult to compare these values with anything in a systematic way, they are of a similar magnitude to those reported in a number of previous publications [91, 100-104] (for a range of metals). Furthermore, that the softer material should be more susceptible to strain rate hardening (higher value of C) than the harder material (when, apart from the degree of prior work hardening, they are essentially the same material) certainly appears to be plausible - there is clearly more scope for relatively greater hardening with softer materials and it thus seems likely that the effect of an increased strain rate would be more noticeable (although this is not a rigorous argument). In fact, the data presented here are more comprehensive than those of earlier studies, both in terms of the spatial and temporal variations in local strain rate being fully incorporated into the modelling and because two independent sets of experimental measurements have been obtained in each case. The fact that, in general, both types of measurement point to similar values of C in each case does allow increased confidence in their reliability.

In detail, there are certainly some discrepancies, notably in terms of the results for the softer material, for which the outcome with the lower impact velocity (strain rates) appears a little inconsistent with those dominated by higher strain rates. It's clear that the JC formulation is simplistic, with complete decoupling of the base shape of the stress-strain curve, the softening effect of raising the temperature and the hardening effect of raising the strain rate. From a mechanistic (microstructural) point of view, it is the mobility of dislocations that is the key factor (with deformation twinning being rather unlikely in these two materials), and, while this will be enhanced by high temperature and reduced by imposing a high strain rate, it's quite likely that there would be some kind of inter-dependence between the two effects. Furthermore, studies [81] aimed at exploring dislocation dynamics over a range of (high) strain rates have indicated that there is often a transition in the rate-determining process as the strain rate is increased (for example, from the rate of motion of existing dislocations to the rate of nucleation of new ones at a shock front). It is therefore not unreasonable to expect that the apparent strain rate sensitivity would be different in two experiments in

which the strain was imposed at substantially different average strain rates with different degrees of heating. However, there may be a danger of over-analysing these results, which do, in general, confirm that the JC formulation appears to provide a broadly reliable description of the strain rate sensitivity, and also that the proposed methodology allows this sensitivity to be quantified in approximate terms. Of course, the methodology could also be used to check on the reliability of alternative formulations.

8.4 Summary

A novel procedure has been developed and presented for experimental evaluation of the strain rate sensitivity parameter, C , in the JC equation (which would also be applicable to other formulations). This procedure has been carried out on two different materials, in the form of as-received (work-hardened) and annealed copper. In both cases, three different impact velocities were used (~ 50 – 250 m s⁻¹). Good levels of agreement were obtained (using best-fit values of C), over the range of velocity employed. The strain rates operative during the plastic deformation were predominantly of the order of 10^4 – 10^6 s⁻¹.

The values obtained for C were 0.016 ± 0.005 for the harder (as-received) material and 0.030 ± 0.010 for the softer (annealed) material. Using these values, the level of agreement observed between predicted and observed experimental outcomes is good, with misfit parameter values mostly around 10^{-3} , allowing a reasonable level of confidence to be placed in both the broad reliability of the JC formulation and the accuracy of the inferred values of C .

Chapter 9

Evaluation of the Fracture Energy of Magnesium via Ballistic Impact Experiments

9.1 Introduction

The metal chosen for this work is cast (pure) magnesium. The main reason for this choice is simply that magnesium has a relatively low fracture energy (for a metal), such that well-defined crack propagation can be stimulated by (ballistic) indentation. This characteristic, in combination with reasonably high ductility (capacity for plastic straining) makes it suitable for this study. It should, however, be recognized that magnesium does exhibit some complexities, including a tendency for complex twin structures to be generated and for anisotropic behavior to be exhibited. Several studies [241-245] have been undertaken in which the fracture characteristics of magnesium alloys have been explored under high strain rate conditions. These characteristics need to be borne in mind when attempting to extract generalized conclusions in this area.

9.2 Microstructure

The grain structure of the ingot (transverse section) and the locations of the test samples are shown in Figure 9.1. It can be seen that the grain size was coarse (of the order of a few mm, with significant variations). There was also a high incidence of (deformation) twins within the grains, as can be seen in the micrograph shown in Figure 9.2. Magnesium, which has an hexagonal crystal structure, is prone to deformation twinning and these arose just from the stresses created during solidification and cooling of the ingot. Coarse grain structures such as this present challenges in terms of using indentation to obtain (bulk) properties, since these can only be obtained by

mechanically interrogating a representative (multi-grain) volume. The indents were therefore created using relatively large cermet (WC-Co) spheres (of diameter 5 mm).

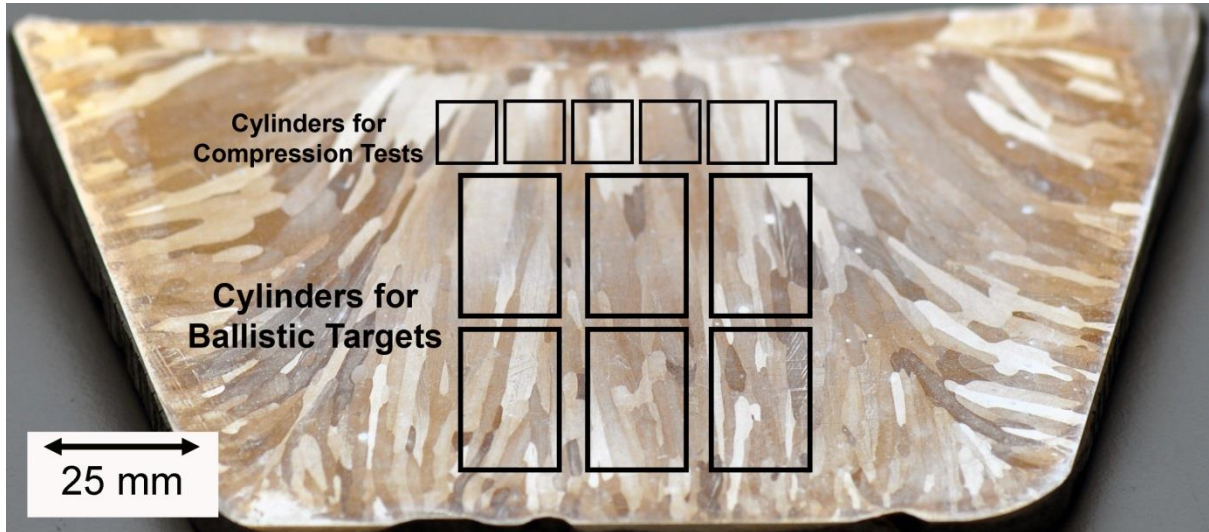


Figure 9.1 Photograph of a transverse section of the cast magnesium ingot, showing the approximate locations of the cylindrical samples taken from it for compression and ballistic testing.

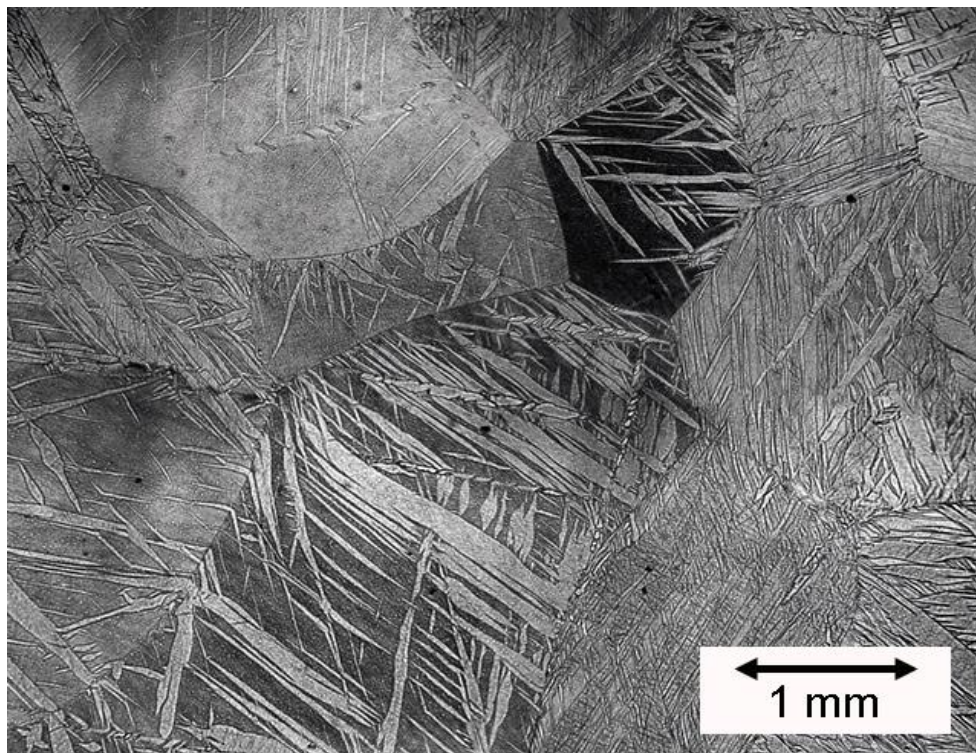


Figure 9.2 Optical micrograph of the cast magnesium ingot. Section from the impact surface.

9.3 Effects of Temperature and Strain Rate on Plasticity

9.3.1 Quasi-static Stress-strain Plots as a Function of Temperature

Stress-strain curves are shown in Figure 9.3 for three different temperatures, after elimination of the elastic component and conversion to true values (using Equation 2.3). It should first be noted that the reduction in true stress as the strain rises above about 12%, observed for the two lower temperatures. In this particular case, it was probably due to (observed) inter-granular cracking at the free surface, leading in some cases to actual loss of grains from the sample. This kind of behaviour is not uncommon with Mg alloys [244, 245]. The effect may also be explained by a transition in the deformation mechanism from slip to twinning, as is common in the compression response of magnesium [246]. In view of this, the real plasticity characteristics exhibited by this material (as a function of temperature) are probably captured reasonably well by Equation 6.5, using the set of parameter values shown in the plot. Of course, it should be recognized that there are significant limitations to this procedure, one of which is that this material is probably quite strongly textured (and hence plastically anisotropic). Mg is certainly known to exhibit relatively complex stress-strain characteristics, partly as a result of high levels of twinning [246]. It may also be noted that these plots reflect the response when loaded parallel to the axis of the columnar zone (Fig.1), whereas (ballistic) indentation generates multi-directional deformation.

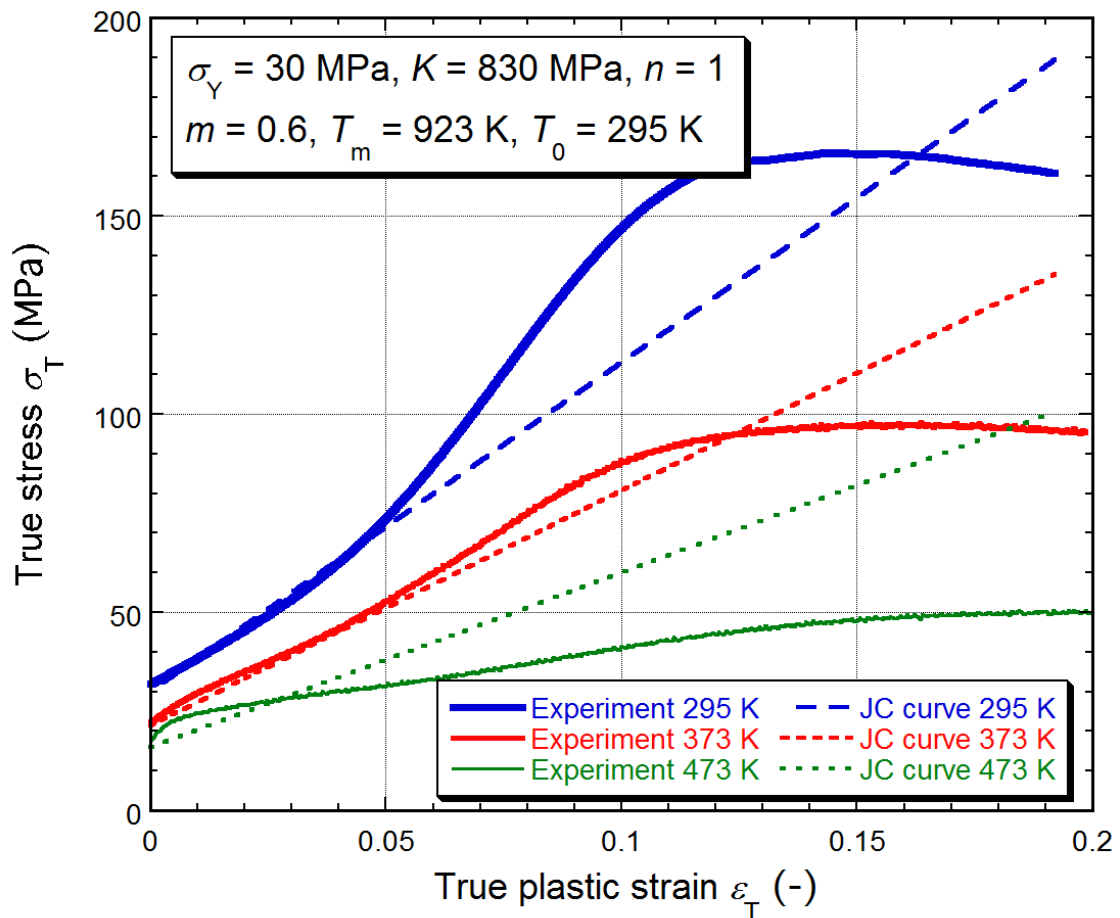


Figure 9.3 Experimental stress-strain plots from compression testing over a range of temperature, together with corresponding best fit JC (Equation 6.5) curves, obtained using the parameter set shown.

9.3.2 Effect of Strain Rate and Evaluation of C

A magnitude of C for this material was estimated by repeatedly running the FEM model, using Equation 6.5 to represent the plasticity. The value of C in this expression was progressively varied, while the values of the other parameters in it were held at those shown in Figure 9.3 and the reference (quasi-static) strain rate was taken as the one used in the compression tests (§5.1.6). Figure 9.4 shows, for an impact velocity of 50 m s^{-1} , (a) a comparison between measured and modelled residual indent shapes, for the best fit value of C , and (b) the dependence of the misfit parameter, S_{red} , on the value of C used in the model. This (low) velocity was chosen because it created no cracks, since these influence the response of the sample. It can be seen that the best fit value for C is about 0.026, although it should be noted that the fit is not perfect (S_{red} is not very close to 10^{-1}).

4) and the peak is not a sharp one. Nevertheless, a value in the range 0.02 – 0.03 seems appropriate and this should be sufficiently accurate to at least approximately capture the plastic deformation under these impact conditions. This is confirmed by Figure 9.5, which shows the corresponding comparisons for the displacement-time data obtained via high speed photography. While there is no reported value of C in the literature for anything resembling this material, it is certainly in the expected range [91, 100-104, 134], particularly since relatively soft metals like this, with potential for work hardening, tend to exhibit relatively high values.

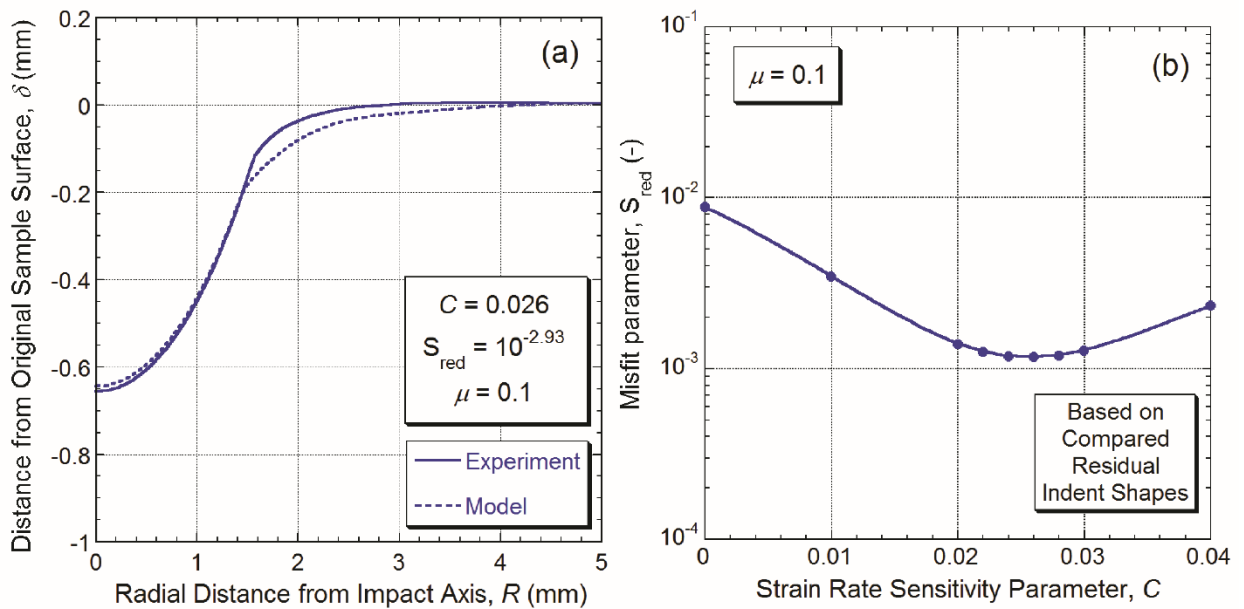


Figure 9.4 Residual indent shape data for an impact velocity of 50 m s^{-1} , showing (a) a comparison between experiment and FEM prediction, for the best fit value of C , and (b) the dependence of the mis fit parameter on the value of C used in the model.

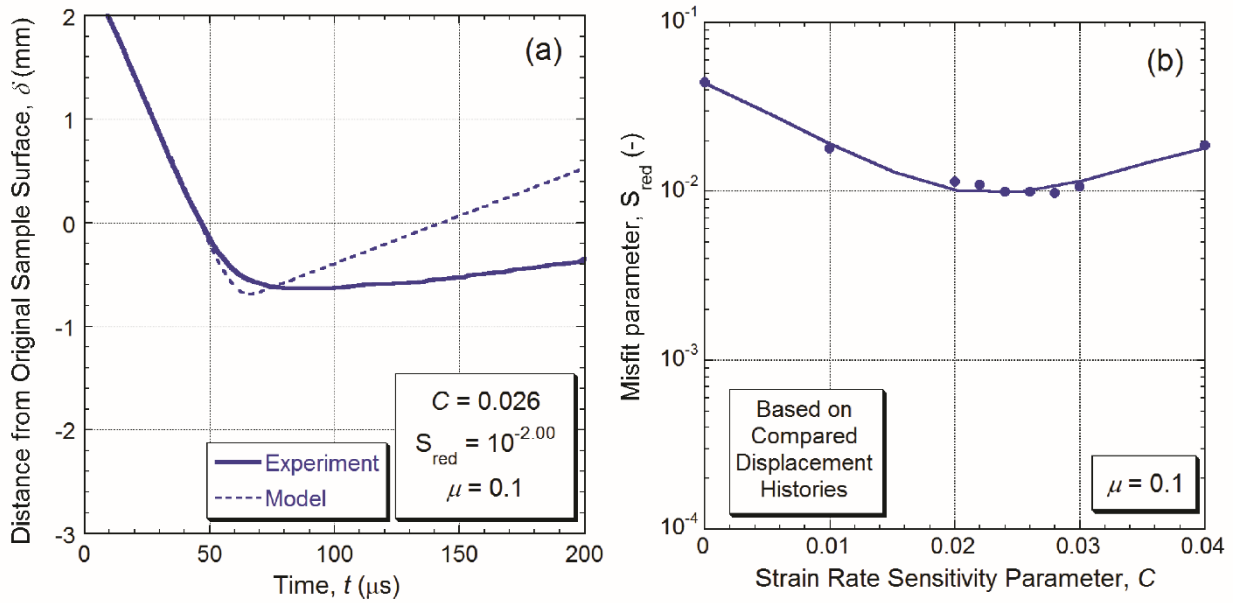


Figure 9.5 Displacement-time data during projectile impact and rebound, for an impact velocity of 50 m s^{-1} , showing (a) a comparison between experiment and FEM prediction, for the best fit value of C , and (b) the dependence of the misfit parameter on the value of C used in the model.

9.4 Evaluation of the Fracture Energy

9.4.1 Tomographic Capture of Crack Patterns

Well-defined cracking – mostly inter-granular – was observed with the higher impact velocities ($> \sim 100 \text{ m s}^{-1}$) used in this work. In order to analyse crack initiation and growth, knowledge of their location and orientation is required. It was found that they provided good contrast in tomographic images. A representative example can be seen Figure 9.6, which also shows a polished section from the same sample. The latter confirms that the cracking is predominantly inter-granular, and also shows that some of these cracks opened up significantly, suggesting that they formed with a strong mode I (“crack opening mode”) component. This is also consistent with the strong contrast seen in tomographic images. Of course, the crack pattern is somewhat irregular, and this was true of most such images. It does not, for example, exhibit clear radial symmetry. This is unsurprising in view of the tendency towards inter-granular cracking and the coarse, rather irregular grain structure. Nevertheless, tomographic images like this did give indications of the nature and orientation of the cracking, and an idea of typical crack

lengths (from the free surface). Cracks mainly propagated in a direction normal to the original free surface, with the crack plane showing a tendency to lie in the “hoop” plane (normal to the radial direction). They could thus be described as “Hertzian”, although with a shape that is closer to a cylinder than a cone. They mostly appear to originate around the periphery of the “impact crater”.

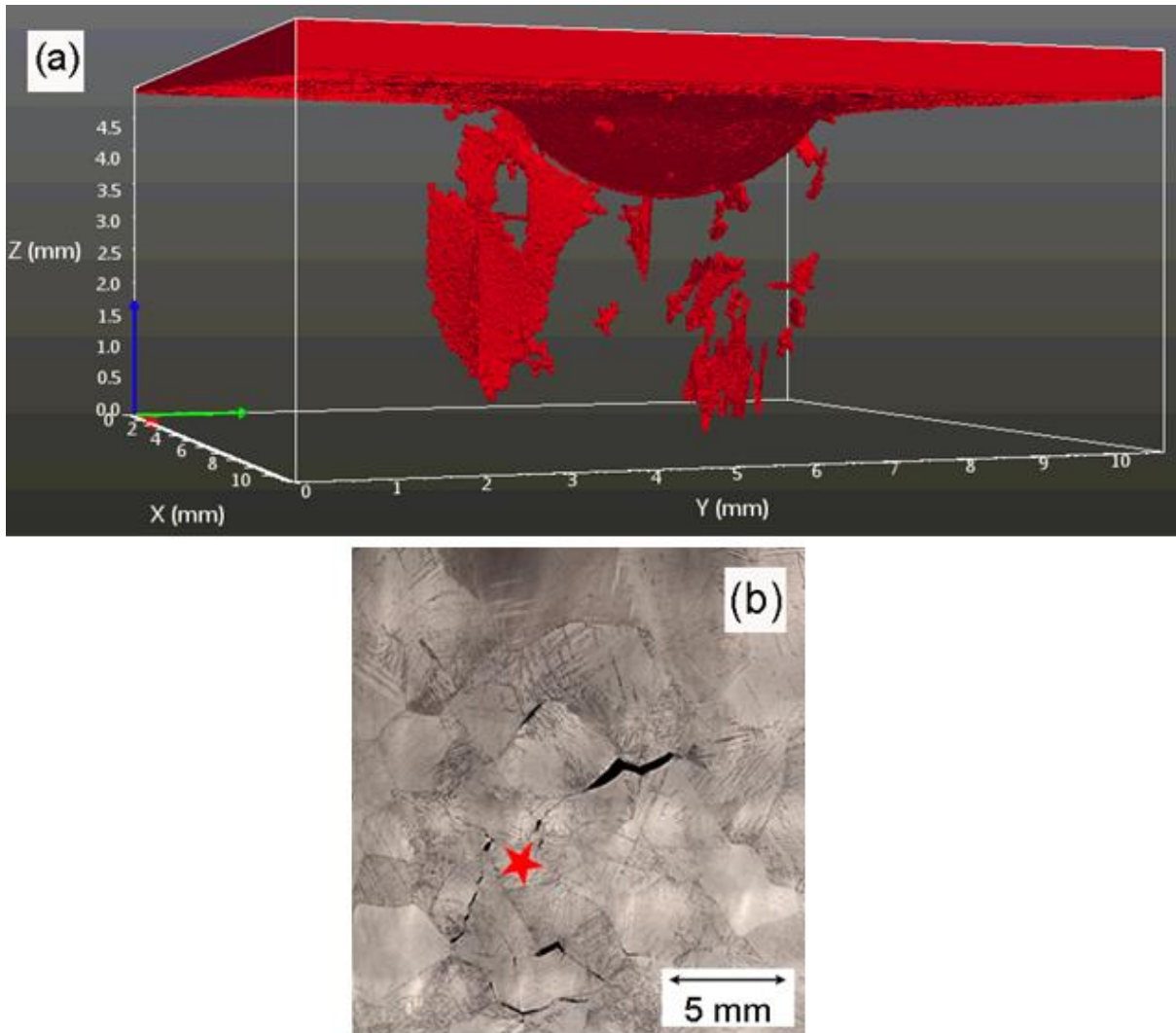


Figure 9.6 Crack patterns after impact with a velocity of 120 m s^{-1} , illustrated by (a) a tomographic visualization and (b) a metallographic section normal to the axis of the projectile motion (marked with a star), at a depth of 2.8 mm below the original free surface.

9.4.2 Stress, Strain, Strain Rate and Temperature Fields

The FEM model can be used to provide insights into the conditions under which crack initiation and propagation occurred. An example is provided by Figure 9.7, which shows the fields concerned at the stages when peak values were obtained, for an incident velocity of 120 m s^{-1} . These give a general feel for the conditions that were created during impact (strains of up to $\sim 60\%$, strain rates up to $\sim 10^5 \text{ s}^{-1}$, temperatures up to $\sim 140^\circ\text{C}$ and deviatoric stresses up to $\sim 500 \text{ MPa}$). However, this type of information does not really provide any pointers towards the onset of cracking. For example, using a “critical strain” criterion would suggest that cracking should start deep within the indent, rather than around the rim of the impact crater where they are actually observed. What is needed is more detailed consideration of the stress field (and strain energy release rates that would be associated with cracking in a particular configuration).

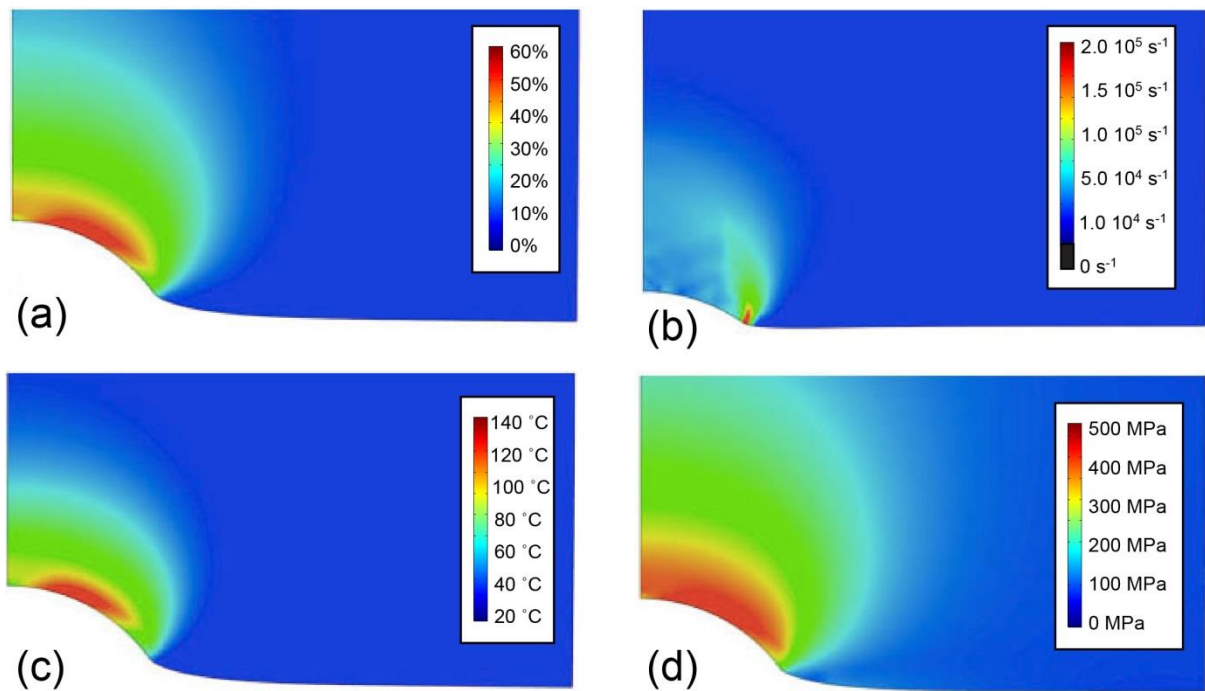


Figure 9.7 Fields of (a) plastic strain, (b) strain rate, (c) temperature and (d) von Mises stress, for an incident velocity of 120 m s^{-1} , each field being shown at the stage when the peak value was attained. (An indication of the stages concerned can be obtained from the penetration depths.)

9.4.3 Simulation of Crack Growth

Since the observed cracks appear to have grown under predominantly mode I loading, attention should be focused on the tensile stresses generated during impact. Figure 9.8 shows contours of the largest tensile principal stresses created during the process (with an impact velocity of 120 m s^{-1}). It can be seen that these did occur in the vicinity of the rim of the impact crater. This suggests that (mode I) cracks are expected to initiate first in that location, under the influence of the tensile stress (of $\sim 100 \text{ MPa}$) indicated by the arrow. This is encouraging in the sense that the observed cracking can be reconciled with the predicted stress field (but not with the application of any type of critical strain criterion). However, the value of 100 MPa is probably not of any significance and indeed attempts to identify “fracture strengths” of materials, expressed as a stress level, are in general unsuccessful, particularly for metals.

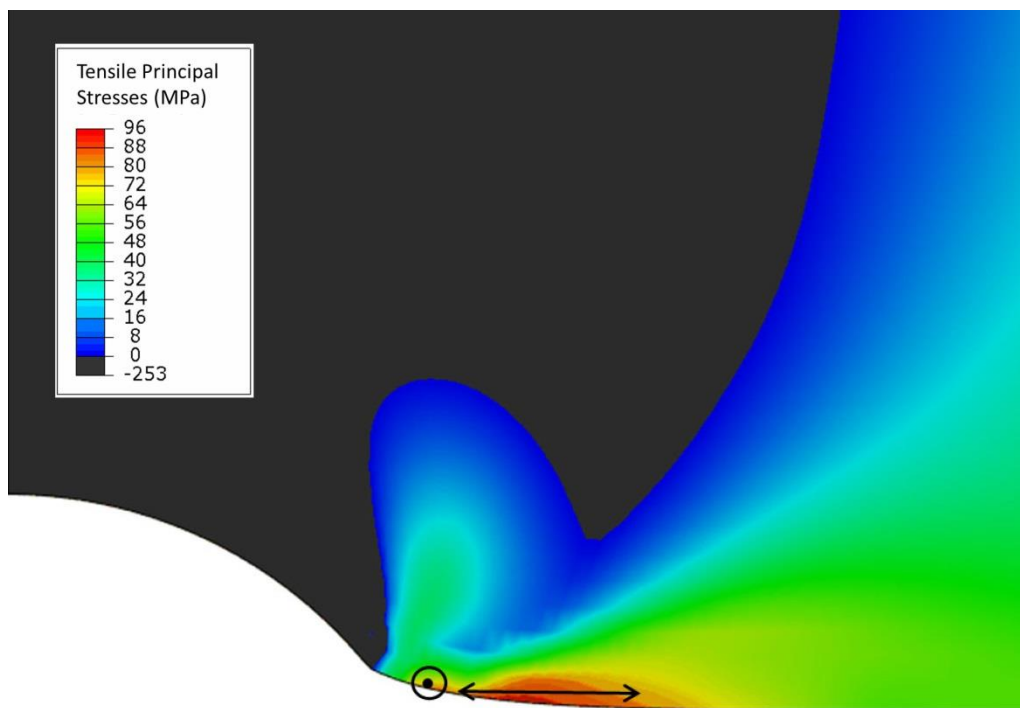


Figure 9.8 Field showing the location of the largest tensile principal stress (with directions indicated in two locations), for an impact velocity of 120 m s^{-1} . This occurred $9 \mu\text{s}$ after initial contact (1.05 mm penetration).

The real objective is to estimate the fracture energy, recognizing the conditions under which crack propagation occurred (in this case, approximately plane strain conditions applied and the mode mix was predominantly mode I). The fracture energy was obtained by the simulation of crack advance, assumed to occur without further projectile motion, as outlined in §6.1.3. The crack plane was predetermined - in this case a cylinder with radius equal to the distance from the axis to the location of peak tensile stress. This plane was initially pinned, with the stress field concerned. The crack front was then allowed to advance (i.e. the plane was unpinned) by a series of increments, driven by the stress relaxation (and associated release of strain energy) that this allowed - see Figure 9.9.

After each advance, the stored elastic strain energy was audited and the strain energy release rate taken as the reduction in energy divided by the increase in crack area. The outcome is shown in Figure 9.10, for two impact velocities and for three different crack lengths. An indication of the fracture energy (critical strain energy release rate) can be obtained from observed crack lengths. Of course, these are not well-defined, but in general they were observed to be of the order of 3-4 mm for both of these impact velocities - see Figure 9.6(a) for an indication of this - and, as shown in Figure 9.10, this leads to an estimate of the fracture energy having a magnitude of the order of 2 kJ m^{-2} . With this particular material, it wasn't possible to carry out a conventional fracture toughness measurement and, in any event, part of the argument here is that the effective toughness is likely to be different (lower) under impact conditions, when (crack tip) plasticity is inhibited. Nevertheless, it may be noted that this fracture energy value, which is relatively low (for a metal), actually appears to be quite plausible, recognizing that magnesium is less tough than many metals.

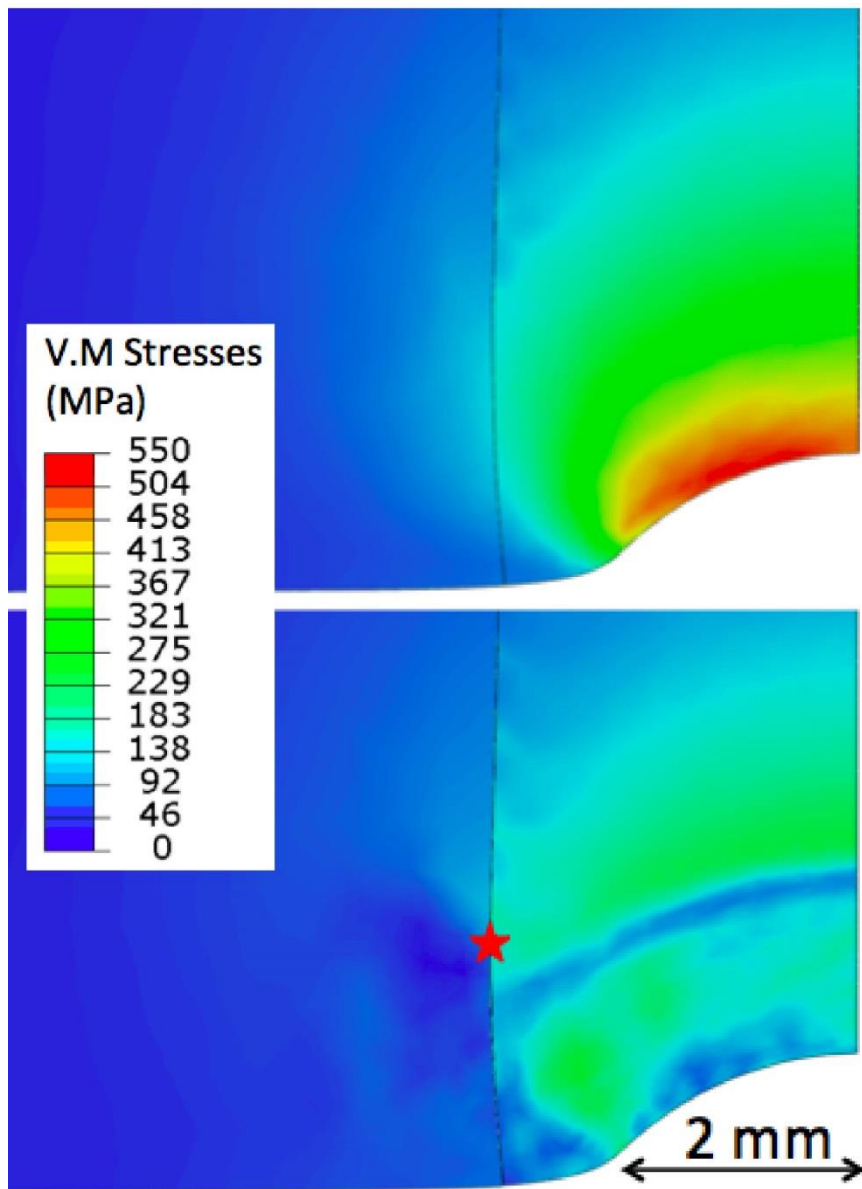


Figure 9.9 Von Mises stress fields before and after crack advance (from the free surface to the marked location (Star)).

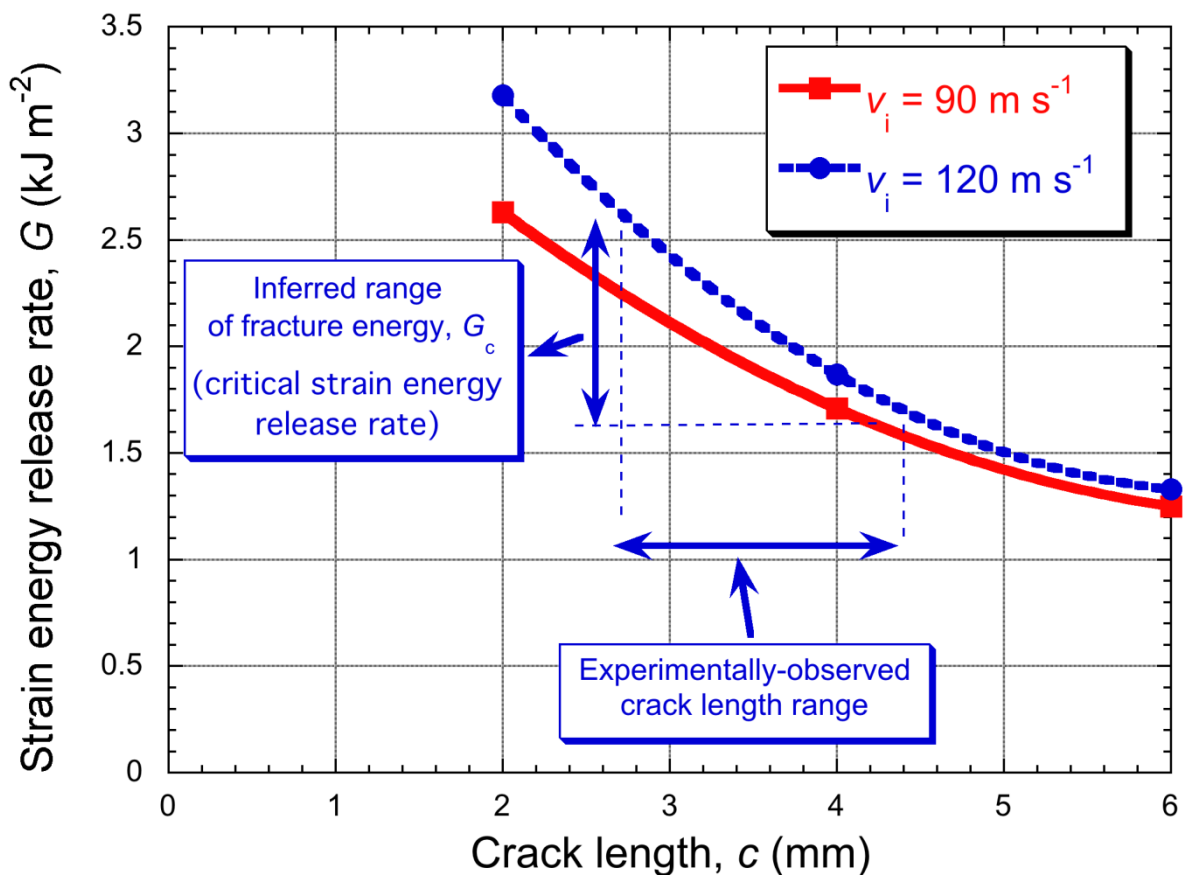


Figure 9.10 Strain energy release rates during crack advance, due to the stress fields arising during impact, and inferred fracture energy range.

It must be recognized that the work presented here incorporates a number of fairly severe simplifications and approximations, both in terms of the details of the modelling and concerning experimental data and observations. This is partly a reflection of the difficulty of creating well-defined crack patterns under high strain rate loading. However, it also relates to the severe challenges faced when attempting to model dynamic crack propagation under impact conditions, using a rigorous fracture mechanics approach. It is certainly a much more complex undertaking than that of using the “conventional” approach of simply defining a critical strain, at which fracture is expected to occur. Nevertheless, since the latter undoubtedly has serious limitations, it may be considered worthwhile to attempt to take the fracture mechanics approach a little further than the very rudimentary study presented here. It is certainly likely that substantial improvements can quite readily be made in the modelling methodology.

The particular fracture initiation condition implemented (whereby the projectile is stopped, effectively halting the simulation process prior to the opening of the crack) means that the conditions are not ideally representative of dynamic fracture. Whilst dynamic conditions are maintained in the development of the indentation process and therefore in the resulting stress field, in halting the simulation, the kinetic energy of the system is removed. At the point of fracture, there are therefore aspects that are better described by quasi-static fracture conditions. Despite this, the measured value is of the expected order of magnitude for a fracture energy of magnesium.

9.5 Summary

A novel procedure is proposed for evaluation of the fracture energy of the material, based on observed crack patterns generated in a ballistic impact event. Ballistic impact experiments have been carried out, using hard spheres as the projectile and thick samples machined from a cast magnesium ingot as the target. Crack geometry was captured using X-ray tomography. FEM simulation was then carried out, with strain rate sensitive plasticity characteristics captured by the JC formulation. The fracture event was studied by “unpinning” an interface representing the crack plane (a cylinder with radius corresponding to the position around the rim where cracking was initiated). In assessing the stored elastic strain energy in the sample, before and after allowing the crack to propagate by the observed distance (a few mm in these cases), a critical strain energy release rate was estimated. This procedure led to an estimated value for the critical strain energy release rate (fracture energy) of about 2 kJ m^{-2} .

Chapter 10

Conclusions

10.1 Creep Properties using Recess Instrumented Indentation

The following conclusions can be drawn from work detailed in chapter 7:

(a) A procedure is described for iterative FEM simulation of the creep deformation that takes place during penetration of a spherical indenter into a sample (under constant applied load). The target outcome is a penetration-time dataset and convergence is obtained via optimisation of the set of 3 parameter values in the MN creep law (covering both primary and secondary regimes).

(b) An important part of the procedure is the prior production on the sample surface of a recess that matches the (spherical) shape of the indenter. This ensures that the stresses in the sample can be kept below the yield stress throughout the indentation test, so that conventional plasticity (and the associated complications) can be avoided.

(c) Experimental work has involved a single material (pure nickel) at a single temperature (750°C). Both conventional uniaxial (tensile) creep tests, using three values for the applied (nominal) stress, and creep indentation testing, under a constant applied load, have been carried out. It is recognized that this constitutes a fairly limited dataset and the results presented are intended mainly to demonstrate the methodology and to obtain some preliminary indications regarding its reliability. Good agreement is observed between the strain-time plots obtained by conventional testing and by using the (MN) creep parameter values inferred via the indentation testing. The stress exponent obtained in this way has a value of about 2.5.

(d) A final “tertiary” regime was observed with the higher stress level tensile tests, which was not captured well in the indentation-derived MN curves. It seems likely that this arose because the true stress was approaching the yield stress, such that conditions were outside the regime that could be represented at lower stress levels by a MN creep law with a single set of parameter values. Indeed, it may be that some conventional plastic deformation was starting to take place in the “tertiary” regime.

(e) The benefits of the proposed method relative to uniaxial testing are numerous. The experimental setup is comparably simple and specimen requirements are less demanding. The numerical aspect means very few assumptions and simplifications are made. Indentation probes a multiaxial response. For most modelling scenarios where isotropic properties are assumed and a multiaxial stress-state is observed, indentation inferred plasticity characteristics would therefore usually provide a better representation of the material. The key drawbacks are the time required to converge on best-fit parameters and that different creep regimes may be active and contributing to the creep response, a distinct possibility given the nature of stress fields below an indenter.

(f) Indentation creep plastometry requires a software package in order to infer strain-time curves from experimental indentation data. Such packages are now starting to become available for indentation plastometry and are likely to be developed soon for indentation creep plastometry.

10.2 Extraction of a Strain Rate Sensitivity Parameter from Ballistic Indentation

The following conclusions can be drawn from work detailed in chapter 8:

(a) A novel procedure has been developed for experimental evaluation of the strain rate sensitivity parameter, C , in the JC equation (which would also be applicable to other formulations). It involves impact of the sample by a hard spherical projectile, followed by monitoring of its penetration and rebound by high-speed photography and/or profilometry of the residual indent shape.

Iterative FEM simulation is then carried out, using trial values for C , with quantification of the level of agreement between predicted and measured outcomes. Input requirements for the model include data characterising the quasi-static plasticity behaviour of the material (over a range of temperature) and also the effect of interfacial friction (which apparently has a small, but detectable, influence).

(b) This procedure has been carried out on two different materials, in the form of as-received (work-hardened) and annealed copper. In both cases, three different impact velocities were used ($\sim 50\text{--}250\text{ m s}^{-1}$), with both high-speed photography and residual indent profilometry being employed. Good levels of agreement were obtained (using best-fit values of C), over the range of velocity employed, for both types of experimental data. The strain rates operative during the plastic deformation were predominantly of the order of $10^4\text{--}10^6\text{ s}^{-1}$.

(c) The values obtained for C were 0.016 ± 0.005 for the harder (as-received) material and 0.030 ± 0.010 for the softer (annealed) material. Using these values, the level of agreement observed between predicted and observed experimental outcomes is good, with misfit parameter values mostly around 10^{-3} , allowing a reasonable level of confidence to be placed in both the broad reliability of the JC formulation and the accuracy of the inferred values of C . There is also good agreement seen with values from the literature for a range of materials, including OFHC copper [91, 100-104].

(d) The benefits of the proposed method relative to SHPB (the most common conventional testing method for measuring high strain rate plasticity) are numerous. The numerical aspect means very few assumptions and simplifications are made. Indentation probes a multiaxial response. For most modelling scenarios where isotropic properties are assumed and a multiaxial stress-state is observed, indentation inferred plasticity characteristics will therefore usually provide a better representation of the material. A plasticity response may also be required, which are accessible with indentation. The key drawbacks are the time required to converge with modelling runs and the ability to characterise over a range of strain rates (due to the probing of a distribution of strain rates during each indentation experiment).

(e) The procedure employed, while involving iterative FEM modelling runs, is one that is amenable to automated convergence. User-friendly software packages for its implementation, requiring no FEM expertise or resources, are likely to become available in the near future.

10.3 Measurement of Fracture Energy from Indentation Data

The following conclusions can be drawn from work detailed in chapter 9:

(a) Ballistic impact experiments have been carried out, using hard spheres as the projectile and thick samples machined from a cast magnesium ingot as the target. This material was chosen in view of its relatively low toughness (compared with many metals). With impact velocities of at least about 100 m s^{-1} , networks of cracks were created. Their geometry was captured using X-ray tomography. These were broadly of a Hertzian type, although approximately cylindrical, rather than conical, and were mostly initiated close to the rim of the impact crater.

(b) FEM simulation was carried out, with the dependence on strain rate of the plasticity being captured via the JC formulation, using an experimentally-determined value of the strain rate sensitivity parameter. The focus was on attempting to understand and predict observed features of the crack initiation and propagation. It was noted that, during impact, relatively high tensile stresses were created around the rim of the impact crater, oriented in the radial direction. It is likely that these stimulated initiation of many of the observed cracks.

(c) A novel procedure is proposed for evaluation of the fracture energy of the material, based on such observed crack patterns. This involves using the FEM model to predict the stress field, and hence the stored elastic strain energy in the sample, before and after allowing the crack to propagate by the observed distance (a few mm in these cases). This was done by “unpinning” this length of an interface representing the crack plane (a cylinder with radius corresponding to the position around the rim where cracking was initiated). This procedure led to an estimated value for the critical strain energy release rate (fracture energy) of about 2 kJ m^{-2} . There is no alternative way of measuring this property under

corresponding conditions (since it is likely to be affected by the very high crack propagation rate), but it is approximately in the range that might have been expected.

(d) The work presented here incorporates a number of fairly severe simplifications and approximations, both in terms of the details of the modelling and concerning experimental data and observations. This is partly a reflection of the difficulty of creating well-defined crack patterns under high strain rate loading. However, it also relates to the severe challenges faced when attempting to model dynamic crack propagation under impact conditions, using a rigorous fracture mechanics approach. It is certainly likely that substantial improvements can quite readily be made in the modelling methodology.

10.4 Future Work

There is considerable scope for future work on the characterisation of mechanical properties from indentation data. In this study, indentation creep tests were carried out at constant load and temperature. Further extensions to this would be to test over a range of temperature to measure an activation energy and variable load experimentation, where the load is changed at some (or multiple) points throughout the test. This would allow for a more complete characterisation of the creep behaviour. A study verifying the method for a variety of metallic materials would also be beneficial.

An obvious real world application for this method would be the testing of welds, where properties are known to vary over small distances. In this way, material could be tested that would previously have required the machining and testing of a miniscule tensile sample, which is tough to do.

Further to this is the extension to the characterisation of coatings, in a similar way Campbell et al. did for plasticity [3, 226]. The creep behaviour of coatings used in aerospace applications is of particular interest. Currently testing of such systems involves the production of tiny tensile specimens. Indentation has the potential to provide a far more cost effective method for testing.

On the topic of ballistic indentation for the extraction of strain rate sensitive plasticity parameters, there is considerable scope for more definitive experimental data and the verification of measured parameters. Conventional methods, which have been shown to introduce errors, would not be satisfactory. It would be necessary to apply a similar inverse FE approach to these. Extension to alternative constitutive laws may also be of interest. The JC law is limited to a single strain rate sensitivity parameter that scales the flow stress with the natural log of the strain rate. This law is therefore not suitable for materials at very high strain rates, where it is common for the response to deviate from a straight line (in terms of flow stress vs the natural log of the strain rate). Certain constitutive laws do account for this behaviour. It would be of interest to see how well this method could characterise such materials over a significant range of strain rates, given a range of strain rates are probed in each indentation experiment. The distribution of strain rates probed (Figure 8.7) suggest this would be doable.

The capability of simulation to model crack propagation is always improving, but still fails to accurately predict dynamic fracture events. The software package, LS-DYNA, have developed the ability to input representative grain structures and crystal plasticity parameters. For the purposes of this study, where the fracture of a large grained magnesium material was studied, such developments are sure to be useful. In fact, not many metallic materials will fracture in the way magnesium was observed to following ballistic indentation, which does severely limit the applicability of the method for the testing of metallic materials.

Integral to the use of all of the methods presented in this study for industrial applications is accreditation. This would require widespread acceptance and thorough verification. In order to facilitate this, software packages that carry out the necessary inverse FEM analysis, with only the relevant experimental input required of the user, would be beneficial.

References

1. Oliver, W.C. and G.M. Pharr, *An Improved Technique for Determining Hardness and Elastic-Modulus Using Load and Displacement Sensing Indentation Experiments*. Journal of Materials Research, 1992. **7**(6): p. 1564-1583.
2. Oliver, W.C. and G.M. Pharr, *Measurement of hardness and elastic modulus by instrumented indentation: Advances in understanding and refinements to methodology*. Journal of Materials Research, 2004. **19**(1): p. 3-20.
3. Campbell, J.E., et al., *Comparison between stress-strain plots obtained from indentation plastometry, based on residual indent profiles, and from uniaxial testing*. Acta Materialia, 2019. **168**: p. 87-99.
4. Rodriguez, P., *Sixty years of dislocations*. Bulletin of Materials Science, 1996. **19**(6): p. 857-872.
5. Zhang, L., et al., *Strain rate dependence of twinning avalanches at high speed impact*. Applied Physics Letters, 2014. **104**(16): p. 162906.
6. Hart, E., *Theory of the tensile test*. Acta metallurgica, 1967. **15**(2): p. 351-355.
7. Zhao, Y., et al., *Influence of specimen dimensions and strain measurement methods on tensile stress-strain curves*. Materials Science and Engineering: A, 2009. **525**(1-2): p. 68-77.
8. Matic, P., G.C. Kirby III, and M.I. Jolles, *The relation of tensile specimen size and geometry effects to unique constitutive parameters for ductile materials*. Proceedings of the Royal Society of London. A. Mathematical and Physical Sciences, 1988. **417**(1853): p. 309-333.
9. Choung, J. and S. Cho, *Study on true stress correction from tensile tests*. Journal of Mechanical Science and Technology, 2008. **22**(6): p. 1039-1051.
10. Barlat, F., *Constitutive modeling for metals*, in *Advanced methods in material forming*. 2007, Springer. p. 1-18.
11. Hollomon, J.H., *Tensile deformation*. Aime Trans, 1945. **12**(4): p. 1-22.
12. Voce, E., *The relationship between stress and strain for homogeneous deformation*. Journal of the Institute of Metals, 1948. **74**: p. 537-562.
13. Capsoni, A. and L. Corradi, *Variational formulations for the plane strain elastic-plastic problem for materials governed by the von Mises criterion*. International journal of plasticity, 1996. **12**(4): p. 547-560.

14. Gariboldi, E. and S. Spigarelli, *Creep and High-Temperature Deformation of Metals and Alloys*, 2019, Multidisciplinary Digital Publishing Institute.
15. Frost, H.J. and M.F. Ashby, *Deformation mechanism maps: the plasticity and creep of metals and ceramics*. 1982: Pergamon press.
16. Frost, H.M., *Review article mechanical determinants of bone modeling*. *Metabolic Bone Disease and Related Research*, 1982. **4**(4): p. 217-229.
17. Withers, P.J. and M. Preuss, *Fatigue and Damage in Structural Materials Studied by X-Ray Tomography*, in *Annual Review of Materials Research, Vol 42*, D.R. Clarke, Editor. 2012, Annual Reviews: Palo Alto. p. 81-103.
18. Frost, H.J. and M.F. Ashby, *Deformation Mechanism Maps - The Plasticity and Creep of Metals and Ceramics*. 1982, Oxford: Pergamon.
19. Owen, D.M. and T.G. Langdon, *Low stress creep behavior: An examination of Nabarro—Herring and Harper—Dorn creep*. *Materials Science and Engineering: A*, 1996. **216**(1-2): p. 20-29.
20. Herring, C., *DIFFUSIONAL VISCOSITY OF A POLYCRYSTALLINE SOLID*. *Journal of Applied Physics*, 1950. **21**(5): p. 437-445.
21. Nabarro, F.R.N., *Report on Conference on Strength of Solids*, 1948, Physical Society, London.
22. Coble, R.L., *A MODEL FOR BOUNDARY DIFFUSION CONTROLLED CREEP IN POLYCRYSTALLINE MATERIALS*. *Journal of Applied Physics*, 1963. **34**(6): p. 1679-&.
23. Weertman, J., *THEORY OF STEADY-STATE CREEP BASED ON DISLOCATION CLIMB*. *Journal of Applied Physics*, 1955. **26**(10): p. 1213-1217.
24. Nabarro, F.R.N., *STEADY-STATE DIFFUSIONAL CREEP*. *Philosophical Magazine*, 1967. **16**(140): p. 231-&.
25. Cadek, J., *CREEP IN PRECIPITATION AND DISPERSION STRENGTHENED ALLOYS - A REVIEW .2. DISLOCATION CLIMB PAST INTERACTING PARTICLES - MODELS OF CREEP*. *Kovove Materialy-Metallic Materials*, 1992. **30**(1): p. 5-43.
26. Mott, N.F., *THE MECHANICAL PROPERTIES OF METALS*. *Proceedings of the Physical Society of London Section B*, 1951. **64**(381): p. 729-&.
27. Lomer, W.M., *A DISLOCATION REACTION IN THE FACE-CENTRED CUBIC LATTICE*. *Philosophical Magazine*, 1951. **42**(334): p. 1327-1331.
28. Zhang, M.H., et al., *Recrystallisation-assisted creep of an austenitic Fe-Ni alloy under low stresses after hot deformation*. *Acta Materialia*, 2018. **153**: p. 23-34.
29. Greenwood, J.N. and H.K. Worner, *Types of creep curve obtained with lead and its dilute alloys*. *Journal of the Institute of Metals*, 1939. **64**: p. 135-167.

30. Feltham, P. and J.D. Meakin, *CREEP IN FACE-CENTRED CUBIC METALS WITH SPECIAL REFERENCE TO COPPER*. Acta Metallurgica, 1959. **7**(9): p. 614-627.
31. Sakai, T. and J.J. Jonas, *Overview no. 35 dynamic recrystallization: mechanical and microstructural considerations*. Acta Metallurgica, 1984. **32**(2): p. 189-209.
32. Souza, R., et al., *Dynamic recovery and dynamic recrystallization competition on a Nb-and N-bearing austenitic stainless steel biomaterial: Influence of strain rate and temperature*. Materials Science and Engineering: A, 2013. **582**: p. 96-107.
33. Sakui, S., T. Sakai, and H. Sawada, *HIGH-TEMPERATURE DEFORMATION-BEHAVIOR AND SUBSTRUCTURES IN ALPHA-IRON*. Journal of the Japan Institute of Metals, 1976. **40**(12): p. 1284-1291.
34. Sakui, S., T. Sakai, and K. Takeishi, *HOT DEFORMATION OF AUSTENITE IN A PLAIN CARBON-STEEL*. Transactions of the Iron and Steel Institute of Japan, 1977. **17**(12): p. 718-725.
35. Ardakani, M., M. McLean, and B. Shollock, *Twin formation during creep in single crystals of nickel-based superalloys*. Acta materialia, 1999. **47**(9): p. 2593-2602.
36. Sass, V., U. Glatzel, and M. Feller-Kniepmeier, *Anisotropic creep properties of the nickel-base superalloy CMSX-4*. Acta materialia, 1996. **44**(5): p. 1967-1977.
37. Carlson, R. and E. Bodine. *An experimental study of compressive-creep behavior at elevated temperatures*. in *Proceedings of ASTM*. 1957.
38. Tilly, G., *Relationships for tensile creep under transient stresses*. Journal of Strain Analysis, 1972. **7**(1): p. 61-68.
39. Taub, A. and F. Luborsky, *Creep, stress relaxation and structural change of amorphous alloys*. Acta Metallurgica, 1981. **29**(12): p. 1939-1948.
40. Norton, F.H., *The creep of steel at high temperatures*. 1929: McGraw-Hill Book Company, Incorporated.
41. Matsunaga, T. and E. Sato, *Creep Mechanism in Several Grades of Aluminum at Low Temperatures*. Materials Transactions, 2013. **54**(12): p. 2202-2208.
42. Wilshire, B. and A.J. Battenbough, *Creep and creep fracture of polycrystalline copper*. Materials Science and Engineering a-Structural Materials Properties Microstructure and Processing, 2007. **443**(1-2): p. 156-166.
43. Debschütz, K.D., et al., *Critical evaluation of the compression creep test*. Journal of the American Ceramic Society, 1993. **76**(10): p. 2468-2474.
44. Peroni, L., M. Scapin, and M. Peroni, *Identification of strain-rate and thermal sensitive material model with an inverse method*, in *Icem 14*:

-
- 14th International Conference on Experimental Mechanics, Vol 6*, F. Bremand, Editor. 2010, E D P Sciences: Cedex A.
45. Baker, M., *A new method to determine material parameters from machining simulations using inverse identification*, in *15th Cirp Conference on Modelling of Machining Operations*, V. Schulze, Editor. 2015, Elsevier Science Bv: Amsterdam. p. 399-404.
46. Umbrello, D., R. M'Saoubi, and J.C. Outeiro, *The influence of Johnson-Cook material constants on finite element simulation of machining of AISI 316L steel*. *International Journal of Machine Tools & Manufacture*, 2007. **47**(3-4): p. 462-470.
47. Zhang, Y.C., J.C. Outeiro, and T. Mabrouki, *On the selection of Johnson-Cook constitutive model parameters for Ti-6Al-4V using three types of numerical models of orthogonal cutting*, in *15th Cirp Conference on Modelling of Machining Operations*, V. Schulze, Editor. 2015, Elsevier Science Bv: Amsterdam. p. 112-117.
48. Corran, R.S.J., P.J. Shadbolt, and C. Ruiz, *Impact Loading of Plates - An Experimental Investigation*. *International Journal of Impact Engineering*, 1983. **1**(1): p. 3-22.
49. Anderson, C.E. and S.R. Bodner, *Ballistic Impact: The Status of Analytical and Numerical Modelling*. *International Journal of Impact Engineering*, 1988. **7**(1): p. 9-35.
50. Corbett, G.G., S.R. Reid, and W. Johnson, *Impact Loading of Plates and Shells by Free Flying Projectiles*. *International Journal of Impact Engineering*, 1996. **18**(2): p. 141-230.
51. Klepaczko, J.R., *PHYSICAL-STATE VARIABLES - THE KEY TO CONSTITUTIVE MODELING IN DYNAMIC PLASTICITY*. *Nuclear Engineering and Design*, 1991. **127**(1): p. 103-115.
52. Albertini, C., E. Cadoni, and G. Solomos, *Advances in the Hopkinson bar testing of irradiated/non-irradiated nuclear materials and large specimens*. *Philosophical Transactions of the Royal Society of London A: Mathematical, Physical and Engineering Sciences*, 2014. **372**(2015): p. 20130197.
53. Bai, Y. and B. Dodd, *Adiabatic Shear Localization*. First ed. 1992, Oxford: Pergamon Press. 378.
54. Timothy, S.P., *THE STRUCTURE OF ADIABATIC SHEAR BANDS IN METALS - A CRITICAL-REVIEW*. *Acta Metallurgica*, 1987. **35**(2): p. 301-306.
55. Wright, T.W., *The Physics and Mathematics of Adiabatic Shear Bands*. 2002: Cambridge University Press.
56. Nguyen, N.T., et al., *Mechanical Behavior of AZ31B Mg Alloy Sheets under Monotonic and Cyclic Loadings at Room and Moderately Elevated Temperatures*. *Materials*, 2014. **7**(2): p. 1271-1295.

57. Taylor, G.I., *The Mechanism of PLastic Deformation of Crystals, I-Theoretical*. Proc. Roy. Soc., 1934. **A145**: p. 362-404.
58. Lee, B.J., S. Ahzi, and R.J. Asaro, *ON THE PLASTICITY OF LOW-SYMMETRY CRYSTALS LACKING 5 INDEPENDENT SLIP SYSTEMS*. Mechanics of Materials, 1995. **20**(1): p. 1-8.
59. Brown, L., *Dislocation plasticity in persistent slip bands*. Materials Science and Engineering: A, 2000. **285**(1-2): p. 35-42.
60. Kombaiah, B. and K.L. Murty, *Dislocation cross-slip controlled creep in Zircaloy-4 at high stresses*. Materials Science and Engineering: A, 2015. **623**: p. 114-123.
61. Püschl, W., *Models for dislocation cross-slip in close-packed crystal structures: a critical review*. Progress in materials science, 2002. **47**(4): p. 415-461.
62. Rao, S., et al., *Calculations of intersection cross-slip activation energies in fcc metals using nudged elastic band method*. Acta materialia, 2011. **59**(19): p. 7135-7144.
63. Gray, G.T., *High-Strain-Rate Deformation: Mechanical Behavior and Deformation Substructures Induced*, in *Annual Review of Materials Research, Vol 42*, D.R. Clarke, Editor. 2012, Annual Reviews: Palo Alto. p. 285-303.
64. Christian, J.W. and S. Mahajan, *Deformation twinning*. Progress in materials science, 1995. **39**(1-2): p. 1-157.
65. Yoshinaga, H., T. Obara, and S. Morozumi, *Twinning deformation in magnesium compressed along the C-axis*. Materials Science and Engineering, 1973. **12**(5-6): p. 255-264.
66. Wu, X., et al., *$\gamma \rightarrow \epsilon$ martensite transformation and twinning deformation in fcc cobalt during surface mechanical attrition treatment*. Scripta materialia, 2005. **52**(7): p. 547-551.
67. Voyiadjis, G.Z. and A.H. Almasri, *A physically based constitutive model for fee metals with applications to dynamic hardness*. Mechanics of Materials, 2008. **40**(6): p. 549-563.
68. Lee, W.S., C.F. Lin, and T.J. Liu, *Impact and Fracture Response of Sintered 316L Stainless Steel Subjected to High Strain Rate Loading*. Materials Characterization, 2007. **58**: p. 363-370.
69. Pan, C.L., S. Wu, and W.W. Yu, *Strain Rate and Aging Effect on the Mechanical Properties of Sheet Steels*. Thin Walled Structures, 2001. **39**: p. 429-444.
70. Höppel, H., et al., *Strain-rate sensitivity of ultrafine-grained materials*. Zeitschrift für Metallkunde, 2005. **96**(6): p. 566-571.
71. Hines, J. and K. Vecchio, *Recrystallization kinetics within adiabatic shear bands*. Acta materialia, 1997. **45**(2): p. 635-649.

72. Andrade, U., et al., *Dynamic recrystallization in high-strain, high-strain-rate plastic deformation of copper*. *Acta metallurgica et materialia*, 1994. **42**(9): p. 3183-3195.
73. Panov, V., *Modelling of behaviour of metals at high strain rates*. 2006.
74. Salvado, F.C., et al., *A review on the strain rate dependency of the dynamic viscoplastic response of FCC metals*. *Progress in Materials Science*, 2017. **88**: p. 186-231.
75. Samantaray, D., S. Mandal, and A. Bhaduri, *A comparative study on Johnson Cook, modified Zerilli–Armstrong and Arrhenius-type constitutive models to predict elevated temperature flow behaviour in modified 9Cr–1Mo steel*. *Computational Materials Science*, 2009. **47**(2): p. 568-576.
76. Zhang, D.N., et al., *A modified Johnson-Cook model of dynamic tensile behaviors for 7075-T6 aluminum alloy*. *Journal of Alloys and Compounds*, 2015. **619**: p. 186-194.
77. Samantaray, D., et al., *Constitutive flow behavior of IFAC-1 austenitic stainless steel depicting strain saturation over a wide range of strain rates and temperatures*. *Materials & Design*, 2014. **56**: p. 565-571.
78. Zerilli, F.J. and R.W. Armstrong, *Dislocation - mechanics - based constitutive relations for material dynamics calculations*. *Journal of applied physics*, 1987. **61**(5): p. 1816-1825.
79. Vandergiesse, E. and A. Needleman, *DISCRETE DISLOCATION PLASTICITY - A SIMPLE PLANAR MODEL*. *Modelling and Simulation in Materials Science and Engineering*, 1995. **3**(5): p. 689-735.
80. McDowell, D.L., *Modeling and experiments in plasticity*. *International Journal of Solids and Structures*, 2000. **37**(1-2): p. 293-309.
81. Molinari, A. and G. Ravichandran, *Constitutive modeling of high-strain-rate deformation in metals based on the evolution of an effective microstructural length*. *Mechanics of materials*, 2005. **37**(7): p. 737-752.
82. Johnson, G.R. and W.H. Cook, *Fracture Characteristics of Three Metals Subjected to Various Strains, Strain Rates, Temperatures and Pressures*. *Engineering Fracture Mechanics*, 1985. **21**(1): p. 31 - 48.
83. Gambirasio, L. and E. Rizzi, *On the calibration strategies of the Johnson-Cook strength model: Discussion and applications to experimental data*. *Materials Science and Engineering a-Structural Materials Properties Microstructure and Processing*, 2014. **610**: p. 370-413.
84. Stainier, L., A.M. Cuitiño, and M. Ortiz, *A micromechanical model of hardening, rate sensitivity and thermal softening in bcc single crystals*. *Journal of the Mechanics and Physics of Solids*, 2002. **50**(7): p. 1511-1545.

85. Scapin, M., L. Peroni, and M. Peroni, *Parameters identification in strain-rate and thermal sensitive visco-plastic material model for an alumina dispersion strengthened copper*. International Journal of Impact Engineering, 2012. **40-41**: p. 58-67.
86. Banerjee, B., *The Mechanical Threshold Stress model for various tempers of AISI 4340 steel*. International Journal of Solids and Structures, 2007. **44**(3-4): p. 834-859.
87. Hopkinson, B., *"The effects of momentary stresses in metals."*. Proceedings of the Royal Society of London, 1905. **74**(505): p. 498-506.
88. Taylor, G., *The testing of materials at high rates of loading*. J. Inst. Civil Eng, 1946. **26**(8): p. 487-501.
89. Kolsky, H., *An investigation of the mechanical properties of materials at very high rates of loading*. Proceedings of the Physical Society. Section B, 1949. **62**: p. 676.
90. Davies, E.D.H. and S.C. Hunter, *THE DYNAMIC COMPRESSION TESTING OF SOLIDS BY THE METHOD OF THE SPLIT HOPKINSON PRESSURE BAR*. Journal of the Mechanics and Physics of Solids, 1963. **11**(3): p. 155-179.
91. Jordan, J.L., et al., *Strain rate-dependant mechanical properties of OFHC copper*. Journal of Materials Science, 2013. **48**(20): p. 7134-7141.
92. Al Salahi, A.A. and R. Othman, *Constitutive equations of yield stress sensitivity to strain rate of metals: A comparative study*. Journal of Engineering, 2016. **2016**.
93. Bertholf, L.D. and C.H. Karnes, *2-DIMENSIONAL ANALYSIS OF SPLIT HOPKINSON PRESSURE BAR SYSTEM*. Journal of the Mechanics and Physics of Solids, 1975. **23**(1): p. 1-19.
94. Chen, W.N.W. and B. Song, *Split Hopkinson (Kolsky) Bar: Design, Testing and Applications*, in *Split Hopkinson*. 2011, Springer: New York. p. 1-+.
95. Maudlin, P.J., et al., *On the modeling of the Taylor cylinder impact test for orthotropic textured materials: experiments and simulations*. International Journal of Plasticity, 1999. **15**(2): p. 139-166.
96. Maudlin, P.J., et al., *High-rate material modelling and validation using the Taylor cylinder impact test*. Philosophical Transactions of the Royal Society a-Mathematical Physical and Engineering Sciences, 1999. **357**(1756): p. 1707-1729.
97. Lopatnikov, S.L., et al., *Dynamics of metal foam deformation during Taylor cylinder-Hopkinson bar impact experiment*. Composite Structures, 2003. **61**(1-2): p. 61-71.
98. Gama, B.A., S.L. Lopatnikov, and J.W. Gillespie Jr, *Hopkinson bar experimental technique: A critical review*. Applied Mechanics Reviews, 2004. **57**: p. 223.

-
99. Prabowo, D.A., M.A. Kariem, and L. Gunawan, *The Effect of Specimen Dimension on the Results of the Split-Hopkinson Tension Bar Testing*, in *Plasticity and Impact Mechanics*, N.K. Gupta and M.A. Iqbal, Editors. 2017, Elsevier Science Bv: Amsterdam. p. 608-614.
 100. Noh, H.G., et al., *Verification of dynamic flow stress obtained using split Hopkinson pressure test bar with high-speed forming process*. International Journal of Advanced Manufacturing Technology, 2017. **91**(1-4): p. 629-640.
 101. Mylonas, G.I. and G.N. Labeas, *Mechanical Characterisation of Aluminium Alloy 7449-T7651 at High Strain Rates and Elevated Temperatures Using Split Hopkinson Bar Testing*. Experimental Techniques, 2014. **38**(2): p. 26-34.
 102. Sedighi, M., M. Khandaei, and H. Shokrollahi, *An approach in parametric identification of high strain rate constitutive model using Hopkinson pressure bar test results*. Materials Science and Engineering a-Structural Materials Properties Microstructure and Processing, 2010. **527**(15): p. 3521-3528.
 103. Sasso, M., G. Newaz, and D. Amodio, *Material characterization at high strain rate by Hopkinson bar tests and finite element optimization*. Materials Science and Engineering a-Structural Materials Properties Microstructure and Processing, 2008. **487**(1-2): p. 289-300.
 104. Mishra, A., et al., *High-strain-rate response of ultra-fine-grained copper*. Acta Materialia, 2008. **56**(12): p. 2770-2783.
 105. Zhao, H., G. Gary, and J. Klepaczko, *On the use of a viscoelastic split Hopkinson pressure bar*. International Journal of Impact Engineering, 1997. **19**(4): p. 319-330.
 106. Gray, G.T., *Classic Split-Hopkinson Pressure Bar Testing*. Materials Park, OH: ASM International, 2000., 2000: p. 462-476.
 107. Field, J., et al., *Review of experimental techniques for high rate deformation and shock studies*. International journal of impact engineering, 2004. **30**(7): p. 725-775.
 108. Demiral, M., et al. *Finite-element simulations of split Hopkinson test of Ti-based alloy*. in *Advanced Materials Research*. 2011. Trans Tech Publ.
 109. Briscoe, B.J. and R.W. Nosker, *THE INFLUENCE OF INTERFACIAL FRICTION ON THE DEFORMATION OF HIGH-DENSITY POLYETHYLENE IN A SPLIT HOPKINSON PRESSURE BAR*. Wear, 1984. **95**(3): p. 241-262.
 110. Klepaczko, J., *EFFECTS OF STRAIN-RATE HISTORY ON STRAIN HARDENING CURVE OF ALUMINIUM*. Archiwum Mechaniki Stosowanej, 1967. **19**(2): p. 211-+.
 111. Mamishev, A.V., et al., *Parameter estimation using an interdigital dielectrometry sensor with finite-element software*. Ieee 1997 Annual

- Report - Conference on Electrical Insulation and Dielectric Phenomena, Vols I and II. 1997, New York: I E E E. 234-237.
112. Lin, L., et al., *Characterization of material properties using an inverse method*, in *Modern Practice in Stress and Vibration Analysis VI, Proceedings*, P.S. Keogh, Editor. 2006, Trans Tech Publications Ltd: Durnten-Zurich. p. 107-+.
113. Telejko, T. and Z. Malinowski, *Application of an inverse solution to the thermal conductivity identification using the finite element method*. *Journal of Materials Processing Technology*, 2004. **146**(2): p. 145-155.
114. Llopis-Albert, C., F. Rubio, and F. Valero, *Characterization and assessment of composite materials via inverse finite element modeling*. *Multidisciplinary Journal for Education Social and Technological Sciences*, 2019. **6**(2): p. 1-10.
115. Oliveira, I., et al., *Inverse Characterization of Material Constitutive Parameters for Dynamic Applications*, in *Icsi 2015 the 1st International Conference on Structural Integrity Funchal*, P. Moreira and P.J. Tavares, Editors. 2015, Elsevier Science Bv: Amsterdam. p. 784-791.
116. Zhao, M.H., et al., *Determination of uniaxial residual stress and mechanical properties by instrumented indentation*. *Acta Materialia*, 2006. **54**(10): p. 2823-2832.
117. Capehart, T.W. and Y.T. Cheng, *Determining constitutive models from conical indentation: Sensitivity analysis*. *Journal of Materials Research*, 2003. **18**(4): p. 827-832.
118. Dean, J., J.M. Wheeler, and T.W. Clyne, *Use of Quasi-Static Nanoindentation Data to Obtain Stress-Strain Characteristics for Metallic Materials*. *Acta Materialia*, 2010. **58**: p. 3613-3623.
119. Alkorta, J., J.M. Martinez-Esnaola, and J.G. Sevillano, *Absence of one-to-one correspondence between elastoplastic properties and sharp-indentation load-penetration data*. *Journal of Materials Research*, 2005. **20**(2): p. 432-437.
120. Tho, K.K., et al., *Uniqueness of reverse analysis from conical indentation tests*. *Journal of Materials Research*, 2004. **19**(8): p. 2498-2502.
121. Cheng, Y.T. and C.M. Cheng, *Can Stress-Strain Relationships be Obtained from Indentation Curves using Conical and Pyramidal Indenters*. *J. Mat. Res.*, 1999. **14**(9): p. 3493-3496.
122. Bucaille, J.L., et al., *Determination of plastic properties of metals by instrumented indentation using different sharp indenters*. *Acta Materialia*, 2003. **51**(6): p. 1663-1678.
123. Cao, Y.P. and J. Lu, *A new method to extract the plastic properties of metal materials from an instrumented spherical indentation loading curve*. *Acta Materialia*, 2004. **52**: p. 4023-4032.

124. Chen, X., et al., *On the uniqueness of measuring elastoplastic properties from indentation: The indistinguishable mystical materials*. Journal of the Mechanics and Physics of Solids, 2007. **55**(8): p. 1618-1660.
125. Gavrus, A., et al., *Investigation of high speed behaviour of ductile materials by computer simulation and Hopkinson experimental test*. Advances in Mechanical Behaviour, Plasticity and Damage, Vols 1 and 2, Proceedings, ed. D. Miannay, et al. 2000, Amsterdam: Elsevier Science Bv. 535-540.
126. Guo, X., et al., *Inverse Identification at Very High Strain Rate of the Johnson-Cook Constitutive Model on the Ti-6Al-4V Alloy With a Specially Designed Direct-impact Kolsky Bar Device*. Strain, 2014. **50**(6): p. 527-538.
127. Meyer, H.W. and D.S. Kleponis, *Modeling the high strain rate behavior of titanium undergoing ballistic impact and penetration*. International Journal of Impact Engineering, 2001. **26**(1): p. 509-521.
128. Dey, S., et al., *The Effect of Target Strength on the Perforation of Steel Plates Using Three Different Projectile Nose Shapes*. Int J Impact Eng, 2004. **30**: p. 1005 - 1038.
129. Børvik, T., et al., *Experimental and numerical study on the perforation of AA6005-T6 panels*. International Journal of Impact Engineering, 2005. **32**(1): p. 35-64.
130. Frutschy, K. and R. Clifton, *High-temperature pressure-shear plate impact experiments on OFHC copper*. Journal of the Mechanics and Physics of Solids, 1998. **46**(10): p. 1723-1744.
131. Andrews, E., et al., *Analysis of the impact of a sharp indenter*. Int J Solids and Structures, 2002. **39**: p. 281-295.
132. Lu, J., S. Suresh, and G. Ravichandran, *Dynamic indentation for determining the strain rate sensitivity of metals*. J Mech Phys Solids, 2003. **51**: p. 1923-1938.
133. Skordaris, G., K.D. Bouzakis, and P. Charalampous, *A dynamic FEM simulation of the nano-impact test on mono- or multi-layered PVD coatings considering their graded strength properties determined by experimental-analytical procedures*. Surface & Coatings Technology, 2015. **265**: p. 53-61.
134. Burley, M., et al., *Johnson-Cook parameter evaluation from ballistic impact data via iterative FEM modelling*. International Journal of Impact Engineering, 2018. **112**: p. 180-192.
135. Inglis, C., *Stress in a Plate due to the Presence of Cracks and Sharp Corners*. Trans. Inst. Naval Architects, 1913. **55**: p. 219-230.
136. Griffith, A.A., *The Phenomena of Rupture and Flow in Solids*. Philosophical Transactions of the Royal Society of London, 1920. **A221**: p. 163-198.

137. Sugimura, Y., et al., *Fracture normal to a bimaterial interface: effects of plasticity on crack-tip shielding and amplification*. Acta Metallurgica et Materialia, 1995. **43**(3): p. 1157-1169.
138. Cleri, F., et al., *Atomic-scale mechanism of crack-tip plasticity: dislocation nucleation and crack-tip shielding*. Physical Review Letters, 1997. **79**(7): p. 1309.
139. Anderson, T.L., *Fracture mechanics-fundamentals and applications*. NASA STI/Recon Technical Report A, 1991. **92**.
140. Irwin, G.R., *Fracture Dynamics*, in *Fracturing of Metals*. 1948, ASM. p. 147-166.
141. Zhu, X.-K. and J.A. Joyce, *Review of fracture toughness (G, K, J, CTOD, CTOA) testing and standardization*. Engineering Fracture Mechanics, 2012. **85**: p. 1-46.
142. Chao, Y.-J. and X.-K. Zhu, *A Simple Theory for Describing the Transition Between Tensile and Shear Mechanisms in Mode I, II, III, and Mixed-Mode Fracture*, in *Mixed-mode crack behavior*. 1999, ASTM International.
143. Wells, A. *Critical tip opening displacement as fracture criterion*. in *Proc. Crack Propagation Symp.* 1961.
144. Wells, A.A., *Crack opening displacements from elastic-plastic analyses of externally notched tension bars*. Engineering Fracture Mechanics, 1969. **1**(3): p. 399-410.
145. Rice, J.R., *A path independent integral and the approximate analysis of strain concentration by notches and cracks*. 1968.
146. Begley, J. and J. Landes, *The J integral as a fracture criterion*, in *Fracture Toughness: Part II*. 1972, ASTM International.
147. Shih, C., *Relationships between the J-integral and the crack opening displacement for stationary and extending cracks*. Journal of the Mechanics and Physics of Solids, 1981. **29**(4): p. 305-326.
148. Rice, J.R., *Limitations to the small scale yielding approximation for crack tip plasticity*. Journal of the Mechanics and Physics of Solids, 1974. **22**(1): p. 17-26.
149. Brown, W.F., *Review of developments in plane strain fracture toughness testing*. 2011: ASTM International.
150. Rosakis, A.J. and L. Freund, *Optical measurement of the plastic strain concentration at a crack tip in a ductile steel plate*. Journal of Engineering Materials and Technology, 1982. **104**(2): p. 115-120.
151. Atkinson, C. and J. Eshelby, *The flow of energy into the tip of a moving crack*. International Journal of Fracture Mechanics, 1968. **4**(1): p. 3-8.
152. Moran, B. and C. Shih, *A general treatment of crack tip contour integrals*. International journal of fracture, 1987. **35**(4): p. 295-310.

153. Chang-Chun, W., H. Peixiang, and L. Ziran, *Extension of J integral to dynamic fracture of functional graded material and numerical analysis*. Computers & structures, 2002. **80**(5-6): p. 411-416.
154. Lynch, S., *Hydrogen embrittlement (HE) phenomena and mechanisms*, in *Stress corrosion cracking*. 2011, Elsevier. p. 90-130.
155. Newman, R.C., *Stress-corrosion cracking mechanisms*, in *Corrosion Mechanisms in Theory and Practice*. 2011, CRC Press. p. 511-556.
156. Gurovich, B., et al., *Assessment of relative contributions from different mechanisms to radiation embrittlement of reactor pressure vessel steels*. Journal of Nuclear Materials, 1997. **246**(2-3): p. 91-120.
157. Barnoush, A. and H. Vehoff, *Recent developments in the study of hydrogen embrittlement: Hydrogen effect on dislocation nucleation*. Acta Materialia, 2010. **58**(16): p. 5274-5285.
158. Barnoush, A., M. Asgari, and R. Johnsen, *Resolving the hydrogen effect on dislocation nucleation and mobility by electrochemical nanoindentation*. Scripta Materialia, 2012. **66**(6): p. 414-417.
159. Barnoush, A. and H. Vehoff, *Hydrogen embrittlement of aluminum in aqueous environments examined by in situ electrochemical nanoindentation*. Scripta Materialia, 2008. **58**(9): p. 747-750.
160. Deya, S., I. Chatteraja, and S. Sivaprasada, *Effect of hydrogen on mechanical degradation and fatigue in 7075 Aluminium alloy with in-situ hydrogenation*. Procedia Engineering, 2015. **114**: p. 461-469.
161. Anderton, C., et al., *Influence of partial hydride formation/decomposition on the mechanical properties of palladium*. Scripta materialia, 1996. **35**(8).
162. Clough, S.P. and D. Stein, *Study of sulfur embrittled oxygen-free copper*. Scr. Metall.:(United States), 1975. **9**(11).
163. Rule, W.K. and S.E. Jones, *A revised form for the Johnson-Cook strength model*. International Journal of Impact Engineering, 1998. **21**(8): p. 609-624.
164. Lin, Y.C., X.M. Chen, and G. Liu, *A modified Johnson-Cook model for tensile behaviors of typical high-strength alloy steel*. Materials Science and Engineering a-Structural Materials Properties Microstructure and Processing, 2010. **527**(26): p. 6980-6986.
165. He, A., et al., *A comparative study on Johnson-Cook, modified Johnson-Cook and Arrhenius-type constitutive models to predict the high temperature flow stress in 20CrMo alloy steel*. Materials & Design, 2013. **52**: p. 677-685.
166. Wierzbicki, T., *Petalling of Plates under Explosive and Impact Loading*. Int. J. Impact Eng., 1999. **22**: p. 935-954.

-
167. Landkof, B. and W. Goldsmith, *Petalling of Thin Metallic Plates During Penetration by Cylindro-Conical Projectiles*. Int. J. Solids and Structures, 1983. **21**(3): p. 245-266.
 168. Atkins, A.G., M.A. Khan, and J.H. Liu, *Necking and Radial Cracking Around Perforations in Thin Sheets at Normal Incidence*. Int J Impact Eng, 1998. **21**(7): p. 521-539.
 169. Borvik, T., et al., *Numerical Simulation of Plugging Failure in Ballistic Penetration*. Int. J. Solids and Structures, 1999. **38**: p. 6241-6264.
 170. Lee, Y.W. and T. Wierzbicki, *Fracture Prediction of Thin Plates under Localised Impulsive Loading. Part 1: Dishing*. Int J Impact Eng, 2005. **31**: p. 1253-1276.
 171. Gupta, N.K., M.A. Iqbal, and G.S. Sekhon, *Experimental and Numerical Studies on the Behaviour of Thin Aluminium Plates Subjected to Impact by Blunt- and Hemispherical-Nosed Projectiles*. International Journal of Impact Engineering, 2006. **32**: p. 1921 - 1944.
 172. Borvik, T., et al., *Experimental and Numerical Study on the Perforation of AA6005-T6 Panels*. International Journal of Impact Engineering, 2005. **32**: p. 35-64.
 173. Borvik, T., et al., *Ballistic Penetration of Steel Plates*. International Journal of Impact Engineering, 1999. **22**: p. 855 - 886.
 174. Borvik, T., et al., *Perforation Of 12mm Thick Steel Plates By 20mm Diameter Projectiles With Flat, Hemispherical And Conical Noses Part 2: Numerical Simulations*. Int J Impact Eng, 2002. **27**: p. 37-64.
 175. Teng, X. and T. Wierzbicki, *Evaluation of Six Fracture Models in High Velocity Perforation*. Engineering Fracture Mechanics, 2006. **73**: p. 1653-1678.
 176. Zabararas, N. and S. Mukherjee, *SOLIDIFICATION PROBLEMS BY THE BOUNDARY-ELEMENT METHOD*. International Journal of Solids and Structures, 1994. **31**(12-13): p. 1829-1846.
 177. Tomishima, T. and T. Yada, *STUDY ON AN IDENTIFICATION METHOD OF RESIDUAL-STRESSES IN A PLATE BY INVERSE ANALYSIS*. Jsme International Journal Series I-Solid Mechanics Strength of Materials, 1989. **32**(1): p. 31-37.
 178. Chai, C.K., et al., *LOCAL ANISOTROPIC MECHANICAL BEHAVIOR OF HUMAN CAROTID ATHEROSCLEROTIC PLAQUES - CHARACTERIZATION USING INDENTATION TEST AND INVERSE FINITE ELEMENT ANALYSIS*. Proceedings of the Asme Summer Bioengineering Conference - 2013, Pt A. 2014, New York: Amer Soc Mechanical Engineers.
 179. Zabararas, N., S. Mukherjee, and O. Richmond, *AN ANALYSIS OF INVERSE HEAT-TRANSFER PROBLEMS WITH PHASE-CHANGES USING AN INTEGRAL METHOD*. Journal of Heat Transfer-Transactions of the Asme, 1988. **110**(3): p. 554-561.

180. Gavrus, A., *A RHEOLOGICAL ANALYSIS OF SOLID POLYMERS USING AN INVERSE METHOD APPLIED TO A FINITE ELEMENT MODEL OF THE TORSION AND TENSILE TESTS*. Proceedings of the Romanian Academy Series a-Mathematics Physics Technical Sciences Information Science, 2010. **11**(4): p. 363-370.
181. Schnur, D.S. and N. Zabaras, *AN INVERSE METHOD FOR DETERMINING ELASTIC-MATERIAL PROPERTIES AND A MATERIAL INTERFACE*. International Journal for Numerical Methods in Engineering, 1992. **33**(10): p. 2039-2057.
182. Katz, M.A. and B. Rubinsky, *AN INVERSE FINITE-ELEMENT TECHNIQUE TO DETERMINE THE CHANGE OF PHASE INTERFACE LOCATION IN ONE-DIMENSIONAL MELTING PROBLEMS*. Numerical Heat Transfer, 1984. **7**(3): p. 269-283.
183. Martinez, F., et al., *Dynamic deformation and adiabatic shear microstructures associated with ballistic plug formation and fracture in Ti-6Al-4V targets*. Materials Science and Engineering a-Structural Materials Properties Microstructure and Processing, 2007. **454**: p. 581-589.
184. Lee, K.Y., D.S. Won, and H.J. Choi, *BOUNDARY ELEMENT ANALYSIS OF STRESS INTENSITY FACTORS FOR Z-SHAPED CRACKS*. Engineering Fracture Mechanics, 1987. **27**(1): p. 75-82.
185. Tu, S., et al., *Stress-strain curves of metallic materials and post-necking strain hardening characterization: A review*. Fatigue & Fracture of Engineering Materials & Structures, 2020. **43**(1): p. 3-19.
186. Kauer, M., et al., *Inverse finite element characterization of soft tissues*. Medical Image Analysis, 2002. **6**(3): p. 275-287.
187. Dean, J., et al., *Energy Absorption during Projectile Perforation of Thin Steel Plates and the Kinetic Energy of Ejected Fragments*. Int. J. Impact Engineering, 2009. **36**(10-11): p. 1250-1258.
188. Tanaka, M. and Y. Masuda, *BOUNDARY ELEMENT METHOD APPLIED TO SOME INVERSE PROBLEMS*. Engineering Analysis with Boundary Elements, 1986. **3**(3): p. 138-143.
189. Hernandez, V.B., et al., *Nanoindentation and microstructure analysis of resistance spot welded dual phase steel*. Materials Letters, 2010. **64**(2): p. 207-210.
190. Dean, J., et al., *A Critical Assessment of the "Stable Indenter Velocity" Method for Obtaining the Creep Stress Exponent from Indentation Data*. Acta Materialia, 2014. **80**: p. 56-66.
191. Campbell, J.E., et al., *Experimental and Computational Issues for Automated Extraction of Plasticity Parameters from Spherical Indentation*. Mechanics of Materials, 2018. **124**: p. 118-131.

192. Mohs, F., *Grundriss der Mineralogie*. 1822, Dresden.
193. Richmond, O., H. Morrison, and M. Devenpeck, *Sphere indentation with application to the Brinell hardness test*. International journal of mechanical sciences, 1974. **16**(1): p. 75-82.
194. Hill, R., B. Storåkers, and A. Zdunek, *A theoretical study of the Brinell hardness test*. Proceedings of the Royal Society of London. A. Mathematical and Physical Sciences, 1989. **423**(1865): p. 301-330.
195. Fischer-Cripps, A.C., *Critical review of analysis and interpretation of nanoindentation test data*. Surface and coatings technology, 2006. **200**(14-15): p. 4153-4165.
196. Dean, J. and T.W. Clyne, *Extraction of Plasticity Parameters from a Single Test using a Spherical Indenter and FEM Modelling*. Mechanics of Materials, 2017. **105**: p. 112-122.
197. Campbell, J., J. Dean, and T.W. Clyne, *Limit case analysis of the "stable indenter velocity" method for obtaining creep stress exponents from constant load indentation creep tests*. Mechanics of Time-Dependent Materials, 2017. **21**(1): p. 31-43.
198. PM, S. and M. Ashby, *Indentation creep*. Materials science and technology, 1992. **8**(7): p. 594-601.
199. Goodall, R. and T.W. Clyne, *A Critical Appraisal of the Extraction of Creep Parameters from Nanoindentation Data obtained at Room Temperature*. Acta Materialia, 2006. **54**(20): p. 5489-5499.
200. Bower, A.F., et al., *Indentation of a Power Law Creeping Solid*. Proc. Roy. Soc. Lond. A, 1993. **441**: p. 97-124.
201. Mayo, M.J. and W.D. Nix, *A Micro-Indentation Study of Superplasticity in Pb, Sn, and Sn-38wt% Pb*. Acta Metall., 1988. **36**(8): p. 2183-2192.
202. Raman, V. and R. Berriche, *An Investigation of the Creep Processes in Tin and Aluminium using a Depth-Sensing Indentation Technique*. J. Mater. Res., 1992. **7**(3): p. 627-638.
203. Fujiwara, M. and M. Otsuka, *Indentation Creep of Beta-Sn and Sn-Pb Eutectic Alloy*. Materials Science and Engineering A, 2001. **A319-321**: p. 929-933.
204. Frost, H.J., C.V. Thompson, and D.T. Walton, *SIMULATION OF THIN-FILM GRAIN STRUCTURES .2. ABNORMAL GRAIN-GROWTH*. Acta Metallurgica Et Materialia, 1992. **40**(4): p. 779-793.
205. Asif, S.A.S. and J.B. Pethica, *Nano-Scale Indentation Creep testing at Non-Ambient Temperature*. J. Adhesion, 1998. **67**: p. 153-165.
206. Shen, L., et al., *Nanoindentation Creep of Tin and Aluminium: A Comparative Study between Constant Load and Constant Strain Rate Methods*. Materials Science and Engineering A, 2012. **532**: p. 505-510.
207. Chen, W., Y. Cheng, and M. Li, *Indentation of power law creep solids by self-similar indenters*. Mat. Sci. & Eng. A, 2010. **527**: p. 5613-5618.

-
208. Choi, I.-C., et al., *Estimating the Creep Stress Exponent of Nanocrystalline Nickel: Sharp vs. Spherical Indentation*. ScienceDirect, 2011. **65**: p. 300-303.
209. Asif, S.A.S. and J.B. Pethica, *Nanoindentation Creep of Single-Crystal Tungsten and Gallium Arsenide*. Phil. Mag., 1997. **76**(6): p. 1105-1118.
210. Su, C., et al., *Measurement of Power-law Creep Parameters by Instrumented Indentation Methods*. Journal of the Mechanics and Physics of Solids, 2013. **61**: p. 517-536.
211. Chen, J. and S.J. Bull, *The Investigation of Creep of Electroplated Sn and Ni-Sn Coating on Copper at Room Temperature by Nanoindentation*. Surf. & Coat. Techn., 2009. **203**(12): p. 1609-1617.
212. Karthikeyan, K., et al., *MULTI-HIT ARMOUR CHARACTERISATION OF METAL-COMPOSITE BI-LAYERS*. Journal of Mechanics of Materials and Structures, 2012. **7**(7): p. 721-734.
213. Banerjee, A., et al., *Numerical simulation of ballistic impact of armour steel plate by typical armour piercing projectile*. Procedia engineering, 2017. **173**: p. 347-354.
214. Lu, J., S. Suresh, and G. Ravichandran, *Dynamic indentation for determining the strain rate sensitivity of metals*. Journal of the Mechanics and Physics of Solids, 2003. **51**(11-12): p. 1923-1938.
215. Atkins, A.G. and D. Tabor, *Plastic Indentation in Metals with Cones*. J Mech Phys Solids, 1965. **13**: p. 149-164.
216. Greszczuk, L.B., ASTM STP 452 1969 42-58., *Theoretical studies of the mechanisms of the fibre-matrix interface in composites*. Interfaces in composites, in *Interfaces in Composites*, ASTM STP. 1969. p. 42-58.
217. Anstis, G.R., et al., *A Critical Evaluation of Indentation Techniques for Measuring Fracture Toughness: 1 - Direct Crack Measurements*. J. Amer. Ceram. Soc., 1981. **64**(9): p. 533-538.
218. Laugier, M., *New formula for indentation toughness in ceramics*. Journal of materials science letters, 1987. **6**(3): p. 355-356.
219. Cuadrado, N., et al., *Geometry of nanoindentation cube-corner cracks observed by FIB tomography: Implication for fracture resistance estimation*. Journal of the European Ceramic Society, 2015. **35**(10): p. 2949-2955.
220. den Toonder, J., et al., *Fracture toughness and adhesion energy of sol-gel coatings on glass*. J. Mater. Res., 2002. **17**(1): p. 224-233.
221. Quinn, G.D. and R.C. Bradt, *On the Vickers indentation fracture toughness test*. J. Amer. Ceram. Soc., 2007. **90**(3): p. 673-680.
222. Chen, J., *On the determination of coating toughness during nanoindentation*. Surface & Coatings Technology, 2012. **206**(13): p. 3064-3068.

-
223. Wasmer, K., et al., *Nanoindentation cracking in gallium arsenide: Part I. In situ SEM nanoindentation*. J. Mater. Res., 2013. **28**(20): p. 2785-2798.
224. Reed, J.L., et al., *A Methodology for Obtaining Plasticity Characteristics of Metallic Coatings via Instrumented Indentation*. Int. J. Solids and Structures, 2015. **80**: p. 128-136.
225. Bouzakis, K. and N. Michailidis, *Coating Elastic-plastic Properties determined by means of Nanoindentations and FEM-supported Evaluation Algorithms*. Thin Solid Films, 2004. **469**: p. 227-232.
226. Campbell, J.E., et al., *Mechanical properties of sprayed overlayers on superalloy substrates, obtained via indentation testing*. Acta Materialia, 2018. **154**: p. 237-245.
227. Liao, Y.G., et al., *Measuring elastic-plastic properties of thin films on elastic-plastic substrates by sharp indentation*. Mechanics of Materials, 2009. **41**(3): p. 308-318.
228. Maier, V., et al., *Thermally Activated Deformation Behavior of ufg-Au: Environmental Issues During Long-Term and High-Temperature Nanoindentation Testing*. JOM, 2015. **67**(12): p. 2934-2944.
229. Wheeler, J., et al., *High temperature nanoindentation: The state of the art and future challenges*. Current Opinion in Solid State and Materials Science, 2015. **19**(6): p. 354-366.
230. Phani, P.S. and W. Oliver, *A direct comparison of high temperature nanoindentation creep and uniaxial creep measurements for commercial purity aluminum*. Acta Materialia, 2016. **111**: p. 31-38.
231. Mesarovic, S.D. and N.A. Fleck, *Spherical indentations of elastic-plastic solids*. Proc. R. Soc. Lond. A, 1999. **455**: p. 2707-2728.
232. Sarris, E. and G. Constantinides, *Finite element modeling of nanoindentation on C-S-H: Effect of pile-up and contact friction*. Cement and Concrete Composites, 2013. **36**: p. 78-84.
233. Liu, Y., et al., *Orientation Effects in Nanoindentation of Single Crystal Copper*. International Journal of Plasticity, 2008. **24**: p. 1990-2015.
234. Zhang, L., et al., *Hydrogen effects on localized plasticity in SUS310S stainless steel investigated by nanoindentation and atomic force microscopy*. Japanese Journal of Applied Physics, 2009. **48**(8S2): p. 08JB08.
235. Ruiz, O. and W. Goldsmith, *Controlled tumbling of projectiles—I. Theoretical model*. International journal of impact engineering, 1988. **7**(1): p. 101-115.
236. Dean, J., et al., *A procedure for extracting primary and secondary creep parameters from nanoindentation data*. Mechanics of Materials, 2013. **65**: p. 124-134.
237. Nelder, J.A. and R. Mead, *A Simplex Method for Function Minimization*. The Computer Journal, 1965. **7**(4): p. 308-313.

-
238. Gao, F.C. and L.X. Han, *Implementing the Nelder-Mead simplex algorithm with adaptive parameters*. Computational Optimization and Applications, 2012. **51**(1): p. 259-277.
 239. Oliphant, T.E., *Python for scientific computing*. Computing in Science & Engineering, 2007. **9**(3): p. 10-20.
 240. van der Walt, S., S.C. Colbert, and G. Varoquaux, *The NumPy Array: A Structure for Efficient Numerical Computation*. Computing in Science & Engineering, 2011. **13**(2): p. 22-30.
 241. Garkushin, G.V., G.I. Kanel, and S.V. Razorenov, *High strain rate deformation and fracture of the magnesium alloy Ma2-1 under shock wave loading*. Physics of the Solid State, 2012. **54**(5): p. 1079-1085.
 242. Daud, M.A.M., et al., *Dynamic Fracture Toughness of Magnesium Alloy under Impact Loading Conditions*, in *Malaysian Technical Universities Conference on Engineering & Technology 2012*, S.A. Aljunid, et al., Editors. 2013, Elsevier Science Bv: Amsterdam. p. 639-644.
 243. Zhou, L. and Y.F. Guo, *Dislocation-Governed Plastic Deformation and Fracture Toughness of Nanotwinned Magnesium*. Materials, 2015. **8**(8): p. 5250-5264.
 244. Malik, A., et al., *Fracture behavior of twin induced ultra-fine grained ZK61 magnesium alloy under high strain rate compression*. Journal of Materials Research and Technology-Jmr&T, 2019. **8**(4): p. 3475-3486.
 245. Jia, W.T., et al., *Deformation and fracture behaviors of AZ31B Mg alloy at elevated temperature under uniaxial compression*. Journal of Alloys and Compounds, 2019. **783**: p. 863-876.
 246. Sakedai, E. and T. Yokoyama, *Investigation of tensile-compressive yield asymmetry and the role of deformation twin in extruded pure magnesium*. International Journal of Materials Research, 2010. **101**(6): p. 736-740.